



UNIVERSITÀ
DEGLI STUDI
DI PADOVA

UNIVERSITÀ DEGLI STUDI DI PADOVA

DIPARTIMENTO DI INGEGNERIA INDUSTRIALE

CORSO DI LAUREA MAGISTRALE IN CHEMICAL AND PROCESS ENGINEERING

**Tesi di Laurea Magistrale in
Chemical and Process Engineering**

**Techno-economic assessment of CO₂ capture in a
decentralized H₂ production plant**

Relatore: Paolo Mocellin

Laureando: FEDERICO VALERIO

ANNO ACCADEMICO 2024-2025

Abstract

Hydrogen is increasingly recognized as a key energy vector in the transition toward a low-carbon economy. When produced from carbon-based sources, coupling hydrogen generation with carbon capture and storage (CCS) technologies is essential to mitigate greenhouse gas emissions. This thesis presents a techno-economic comparison between two CO₂ separation technologies — Pressure Swing Adsorption (PSA) and membrane separation — applied to the capture of carbon dioxide from a pre-combustion hydrogen-rich stream. The hydrogen is generated via an electrically assisted steam methane reforming (e-SMR) process fed with biogas, developed by the company SYPOX. The target gas stream originates from the tail gas of a first PSA unit dedicated to hydrogen recovery and consists of 3.88 kmol/h with a CO₂ molar fraction of approximately 0.7.

For the PSA system, a detailed model based on partial differential equations (PDEs) was implemented in MATLAB, simulating a vacuum swing adsorption (VSA) process with zeolite 13X as the adsorbent. The membrane-based system was analyzed under steady-state conditions using a polymeric membrane composed of PEBAX blended with propylene glycol (PG), also operated under vacuum. Both technologies were evaluated in terms of technical performance — including CO₂ removal efficiency, hydrogen recovery, and energy consumption — and economic aspects, such as capital (CAPEX) and operating (OPEX) expenditures.

The comparative analysis highlights the trade-offs between process efficiency and cost, providing valuable insights into the selection of suitable CO₂ capture technologies for low-emission hydrogen production systems based on renewable feedstocks.

Table of Contents

<i>Introduction</i>	1
<i>Chapter 1 Background on H₂ production based on decentralized steam methane reforming</i>	5
1.1 Centralized vs decentralized production routes	5
1.2 Overview on hydrogen production.....	8
1.2.1 Hydrogen global demand	8
1.2.2 Hydrogen production from fossil feedstock	11
1.2.3 Green hydrogen production.....	14
1.3 Electrified steam methane reforming (e-SMR)	16
1.4 Biogas as a hydrogen production feedstock	22
1.4.1 Biomass	23
1.4.2 Biogas reforming	23
1.4.3 Biogas global consumption	24
1.5 Carbon capture and storage	26
1.5.1 Routes for CO ₂ capture	27
1.5.2 Absorption techniques.....	31
1.5.3 CO ₂ transport and storage.....	33
1.6 SYPOX e-SMR biogas-to-hydrogen process.....	35
1.6.1 Process description	35
1.6.2 CO ₂ capture unit location	36
1.6.3 Hydrogen Production Cost and Carbon footprint.....	38
<i>Chapter 2 Pressure swing adsorption (PSA)</i>	41
2.1 General features of PSA.....	41
2.2 Fundamentals of adsorption	46
2.2.1 Adsorption mechanism.....	46
2.2.2 Adsorption equilibrium.....	50
2.2.3 Diffusion in porous media	54
2.3 PSA cycles: basic principles.....	56
2.3.1 The Skarstrom cycle	58
2.3.2 Pressure equalization	60
2.3.3 Multiple-bed systems.....	63
2.3.4 Vacuum swing cycle	64

2.4	Dynamics and operation of a PSA column.....	67
2.4.1	Pressure drops in packed beds.....	67
2.4.2	The adsorption front.....	68
2.4.3	Mathematical model of a PSA column.....	69
Chapter 3 Membrane gas separation.....		73
3.1	General features of membrane separation.....	73
3.2	Solution-diffusion model.....	74
3.2.1	Assumptions of the model.....	75
3.2.2	Flux equation.....	76
3.2.3	Sorption and diffusion coefficients.....	78
3.3	Membrane types for H ₂ /CO ₂ separation.....	80
3.3.1	Membrane modules.....	80
3.3.2	Polymeric CO ₂ selective membranes.....	82
3.3.3	Facilitated transport membranes.....	83
3.4	Process design.....	84
3.4.1	Design factors.....	85
3.4.2	Multistep and recycle system design.....	87
Chapter 4 PSA unit design.....		89
4.1	CO ₂ capture PSA unit location within the SYPOX process.....	89
4.2	Design of the PSA cycle.....	92
4.2.1	Adsorption step time.....	92
4.2.2	Steps of the cycle.....	93
4.2.3	Cycle scheduling.....	95
4.3	Column sizing.....	97
4.3.1	Adsorbent material selection.....	98
4.3.2	Column design steps.....	100
4.4	Dynamic simulation of the adsorption step.....	104
4.4.1	Mass transfer.....	105
4.4.2	Length of unused bed.....	108
4.4.3	Non-isothermal adsorption step.....	109
Chapter 5 Membrane separation unit design.....		115
5.1	CO ₂ capture membrane unit location in the SYPOX process.....	115
5.2	Membrane model.....	117
5.3	Membrane material selection.....	120

5.4	Membrane unit configuration.....	122
Chapter 6 Economic analysis.....		127
6.1	CAPEX and OPEX definition.....	127
6.2	PSA.....	128
6.2.1	Columns	128
6.2.2	Vacuum pumps.....	129
6.2.3	Switching valves.....	130
6.2.4	Adsorbent.....	130
6.2.5	Total annualised costs	131
6.3	Membrane-based separation.	133
6.3.1	Membranes material and frame	133
6.3.2	Vacuum pumps.....	134
6.3.3	Compressor	135
6.3.4	Total annualised costs	135
6.4	Technologies comparison	138
Conclusions.....		143
Appendices		145
Appendix A: Assumptions for the development of the techno-economic analysis.		145
Appendix B: Comparison of PSA and membrane CO ₂ with absorption using hot potassium carbonate.		149
Bibliographic references		151

Introduction

Global warming refers to the increase in global surface air and sea temperatures, averaged over 30 years to account for natural variability. The estimated rise in temperature from pre-industrial levels (1850–1900) to the decade 2006–2015 is 0.87°C. Scientific assessments warn that surpassing 1.5°C of warming could lead to irreversible climate impacts, including more frequent heatwaves, rising sea levels, biodiversity loss, and ecosystem degradation. The risks escalate significantly between 1.5°C and 2°C, threatening vulnerable communities and ecosystems. Limiting warming to below 1.5°C is essential to reduce extreme weather events, ensure food and water security, and minimize economic disruptions. However, achieving this goal depends on technological advancements, economic feasibility, and socio-political acceptance (IPCC, 2018). Since 1950, human-induced greenhouse gas emissions have been the primary driver of global warming. These emissions arise from burning fossil fuels, deforestation, agriculture, waste management, livestock farming, and industrial production. Among greenhouse gases, carbon dioxide (CO₂) is the largest contributor to recent climate change. While CO₂ is naturally exchanged within the carbon cycle—through plant respiration, volcanic activity, and ocean-atmosphere interactions—human activities have significantly disrupted this balance. The combustion of fossil fuels releases vast amounts of CO₂, while land-use changes, such as deforestation, diminish the planet’s ability to absorb it, intensifying atmospheric CO₂ concentrations and accelerating global warming (U.S. Environmental Protection Agency, n.d.).

In 1958, Charles Keeling refined techniques to detect small fluctuations in CO₂ concentration, establishing a continuous monitoring station at Mauna Loa, Hawaii. His measurements provided the first long-term dataset of rising atmospheric CO₂, confirming its steady increase due to human activities, particularly fossil fuel combustion and deforestation (Keeling CD, 1960). Global CO₂ emissions have grown significantly over the past decades. In 1950, annual emissions were approximately 6 billion tonnes. By 1990, they had nearly quadrupled, surpassing 20 billion tonnes. As of 2023, global CO₂ emissions have exceeded 35 billion tonnes, indicating a persistent upward trend (Ritchie & Roser, 2020). To mitigate climate change, international agreements such as the Paris Agreement aim to limit global warming to well below 2°C, preferably 1.5°C, compared to pre-industrial levels. Achieving these targets requires rapid and substantial reductions in greenhouse gas emissions across all sectors. The Glasgow Climate Pact, adopted during COP26 in 2021, reaffirms this goal, emphasizing the need for a 45% reduction in CO₂ emissions by 2030 (relative to 2010 levels) and achieving net zero around mid-century. In 2018 the largest contributor to CO₂ emissions is the energy sector (74.9 %),

other important contributors are the agriculture sector (12.4 %), industrial processes (9.2 %) and waste management (3.5 %). Effective climate mitigation strategies must ensure equity and just transitions, particularly for marginalized and vulnerable populations, to prevent unintended consequences (IPCC, 2018). A widely accepted approach to reducing CO₂ emissions is to phase out fossil fuels and transition to sustainable alternatives for transportation, heating/cooling, and electricity production. Advancements in electric and hybrid vehicles, along with the rapid development of solar and wind energy, offer promising solutions to curb further emissions growth. However, it would be unfeasible to think to reach the set goals without integrate to this green solution also technologies able to capture and separate the CO₂.

The IPCC highlighted that, *if we are to achieve the ambitions of the Paris Agreement and limit future temperature increases to 1.5°C, we must do more than just increasing efforts to reduce emissions – we also need to deploy technologies to remove CO₂ from the atmosphere. Carbon Capture and Sequestration (CCS) is one of these technologies and can therefore play an important role in tackling global warming.* CCS technologies were specifically developed to reduce the release of carbon dioxide into the atmosphere and, could be key to helping to tackle global warming. It's a three-step process, involving: capturing the CO₂ produced by power generation or industrial activity, transporting it; and then permanently storing it deep underground. Possible storage sites for CO₂ emissions include saline aquifers or depleted oil and gas reservoirs, which typically need to be 1 km or more under the ground. As an example, a storage site for the proposed Zero Carbon Humber project in the UK is a saline aquifer named “Endurance”, located in the southern North Sea, around 90 km offshore. Endurance is approximately 1.6 km below the seabed and has the potential to store very large amounts of CO₂. Similarly, in the U.S. there are multiple large-scale CO₂ sites such as the Citronelle Project in Alabama. This saline reservoir injection site is about 2.9 km deep. As well as CCS, there is a related concept, CCUS, which stands for Carbon Capture Usage and Storage. The idea is that, instead of storing CO₂, it could be re-used in industrial processes by converting it into, for example, plastics, concrete or biofuel. (National Grid, 2025)

In 2022, over 95 Mt of hydrogen were produced, highlighting its importance as a key raw material for energy-intensive industries. Hydrogen demand is expected to grow steadily, given its critical role in decarbonizing industrial processes, space heating (including industrial, commercial, and residential sectors), fuel cell applications, and transportation. Globally, 90% of hydrogen production is used in ammonia and methanol synthesis, Gas-to-Liquid processes, and oil refining, with ammonia alone accounting for 50% of total production. Currently, most hydrogen is produced from fossil fuels such as natural gas, refinery byproducts, and coal, which results in significant CO₂ emissions and contributes to rising greenhouse gas (GHG) levels. The most common methods for hydrogen production are SMR, autothermal reforming (ATR), partial oxidation (POX), and coal gasification, with SMR being the dominant technology. CCS

technologies found important functionality in Steam Methane Reforming (SMR) industrial application, allowing for the creation of low-carbon hydrogen, which can decarbonize the current process in the short and medium term. CCS is essential for reducing CO₂ emissions and can contribute up to 23 % of the reduction of process industry emissions. In traditional fuel-fired Steam Methane Reforming (SMR), only 50% to 65% of the CO₂ emissions result from the chemical reaction that converts methane (CH₄) into hydrogen and carbon dioxide. The remaining 35% to 50% is generated by burning fossil fuels in the furnace to supply the high temperatures required for the reforming reaction. One promising way to avoid emissions from this combustion step is by electrifying the process. Using electrical energy an increasingly important strategy for lowering industrial carbon emissions. Electrification can significantly reduce reliance on furnaces for driving energy-intensive, endothermic chemical reactions. In particular, the electrified version of SMR (e-SMR), which uses resistive heating, is being actively explored as a highly effective method for enhancing high-temperature thermochemical processes, such as hydrogen production. The 2021-born SYPOX has created a biogas to hydrogen decentralized plant with 100 kNm³ h⁻¹ of H₂ productivity based on electrically heated steam reforming reactor.

The objective of the thesis is to analyse two CCS technologies for small scale applications by doing a rough design with purity and productivity constraints. The first technology that will be examined is the pressure swing adsorption (PSA), based on the concept of physical adsorption and desorption that occurs between a solid surface and a gas component while changing operating pressure in a packed bed column. Adsorbent choice, type of the cycle, steps time and column sizing have all an important impact on the final design.

The second technology consists in membrane gas separation which offers an energy-efficient method for capturing CO₂ by selectively allowing carbon dioxide to pass through while retaining other gases.

Chapter 1

Background on H₂ production based on decentralized steam methane reforming

In this chapter, an overview of decentralized plants is done highlighting the main differences with the centralized model. Hydrogen production in decentralized plants is then considered, focusing on how the product stream of those facilities is managed. The main characteristic and usage of the hydrogen produced in decentralized route will be examined which is the environmental impact of those types of plants.

1.1 Centralized vs decentralized production routes

In recent years, industrial production has increasingly shifted toward decentralized sites and locally distributed facilities. This operational model offers greater responsiveness to local demand, aligns with sustainability goals, and enables the use of technologies suited for smaller-scale, modular production. In this context, it is essential to compare the functioning, strengths, and weaknesses of centralized and decentralized plants.

A centralized plant is a large-scale facility—typically comprising one or a few sites—strategically located to serve a wide geographic area. The main features of these facilities are:

- They are often situated near raw material sources to reduce supply chain costs and benefit from integration into established logistics networks. This setup enables significant economies of scale, allowing for bulk procurement, efficient machinery usage, and optimized labour, ultimately reducing per-unit costs.
- Centralized operations facilitate streamlined management and decision-making through unified oversight, enabling consistent quality control and efficient implementation of improvements.
- Resources—such as equipment and skilled personnel—are concentrated in one location, avoiding duplication, minimizing operational overhead, and improving internal communication. This consolidation enhances productivity, simplifies training,

and supports effective risk management. Additionally, scaling production at a single site is often more cost-effective than replicating facilities across multiple locations.

- Centralized logistics reduce supply chain complexity, improving reliability and overall competitiveness.

Despite these advantages, centralized models have notable limitations:

- Establishing centralized facilities require substantial capital investment and extended construction timelines, posing barriers for some industries.
- Centralized production is heavily dependent on extensive logistics networks to distribute goods, often resulting in longer lead times and increased transportation costs—particularly for distant markets. This can affect delivery speed and customer satisfaction.
- Concentrating production in one site introduces strategic risks: operational failures, natural disasters, or geopolitical instability can disrupt the entire supply chain, leading to significant losses.
- Centralized plants may also be less responsive to local market needs or sudden demand shifts and tend to have higher environmental impacts due to elevated energy consumption and emissions from long-distance transport. These vulnerabilities make centralized systems less suitable where resilience, sustainability, and flexibility are priorities.

In contrast, decentralized production involves smaller-scale, modular units located closer to the point of consumption. The main traits of decentralized plants are:

- These facilities can quickly respond to local market needs and adapt to changing conditions as they can be constructed near the source of the input materials or process feedstock.
- Their proximity to end users reduces transportation costs and emissions, shortens delivery times, and enhances customer satisfaction.
- Decentralized systems require lower initial capital investment and can be expanded incrementally, based on demand.
- They offer increased operational resilience, as disruptions in one facility do not compromise the entire production network.

However, decentralized operations also have limitations:

- The lack of economies of scale often results in higher per-unit production costs.

- Resource duplication—in terms of infrastructure, machinery, and workforce—raises operational expenditures. Additionally, coordinating multiple sites while maintaining uniform quality and customer satisfaction poses logistical and managerial challenges.
- Without robust standardization and communication systems, inconsistencies may arise.
- Operating across different regions also introduces regulatory complexity, as each location may require separate compliance with local laws and permitting processes, adding administrative burdens.

These trade-offs highlight the importance of careful planning and system integration when choosing a production model. Table 1.1 summarizes the main features of centralized and decentralized systems.

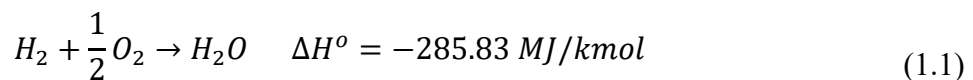
Table 1.1: *General features of centralized and decentralized plants.*

	CENTRALIZED	DECENTRALIZED
PRODUCTION SCALE	Large-scale, high-volume production.	Smaller-scale, localized production
MANAGEMENT COMPLEXITY	Easy to manage and control from a single location.	Complex coordination and management across multiple sites.
FLEXIBILITY	Less flexible, slower to adapt to local market changes.	Highly flexible, quick to respond to local demands.
COST STRUCTURE	Lower per-unit costs due to economies of scale.	Higher operational costs due to multiple facilities.
RISK MANAGEMENT	Higher risk of total disruption from a single point of failure.	Reduced risk through diversification across locations.
LOGISTICS AND DISTRIBUTION	Longer lead times for distribution to distant markets.	Reduced transportation costs and quicker delivery times.

Although they may not benefit from the same economies of scale as centralized facilities, decentralized models are increasingly considered a viable and sustainable alternative, particularly in contexts where adaptability, energy autonomy, and environmental sustainability are prioritized. In general, choosing between centralized and decentralized production models depends on a variety of factors, including economic considerations, infrastructure availability, market demand characteristics, regulatory environments, and sustainability goals.

1.2 Overview on hydrogen production

Hydrogen generation in decentralized is an approach that is gaining increasing attention due to its potential to reduce transportation costs, enhance energy efficiency, and support local energy autonomy. Often located closer to the point of use, decentralized hydrogen production, aligns well with renewable energy sources such as solar and wind, enabling flexible and scalable solutions for various sectors. It offers a low-carbon alternative for hard-to-abate sectors like heavy industry and long-distance transport, while also serving as an efficient means of storing and balancing renewable energy. Currently hydrogen trade remains minimal and mainly constrained to small-scale, localised transport between neighbouring countries, and trade in hydrogen-based products such as ammonia or methanol. In the Net Zero Emissions by 2050 Scenario (NZE Scenario), interregional trade in hydrogen and hydrogen-based fuels reaches more than 70 Mt in hydrogen-equivalent terms (Mt H₂-eq) by 2050, representing almost 20% of global low-emissions hydrogen demand in that year. As such, hydrogen plays a strategic role in decarbonizing the global energy system. As a matter of fact, hydrogen could represent the best alternative as energy source with respect to fossil fuels which demand continues to increase, raising concerns about their depletion. Other energy sources as the renewables solar, wind and geothermal could also be competitive but suffer from intermittency. Hydrogen remains the sources that more than others is capable to be continuous, safe and clean. A key advantage of hydrogen, in fact, is that its oxidation does not result in the formation of carbon dioxide, while producing energy. Indeed, according to hydrogen oxidation reaction:



Moreover, appropriate storage technologies make it possible to utilize hydrogen for domestic applications. Despite its advantages, the widespread adoption of hydrogen production remains limited due to several challenges, primarily its absence in a free form in nature, necessitating its extraction from other raw materials. Fig 1.1 represents the main advantages, disadvantages and features of hydrogen.

1.2.1 Hydrogen global demand

According to the IEA, global hydrogen demand is expected to rise from the actual 90 million tonnes per year to 800 million tonnes per year by 2050, accounting for only 20% of final energy demand. The development of production technologies and the necessary infrastructure to accommodate various feedstocks is progressing at a slow pace. Most hydrogen production worldwide—about 96%—relies on non-renewable sources such as fossil fuels, resulting in approximately 830 million tonnes of CO₂ emissions annually, comparable to the combined

emissions of the United Kingdom and Indonesia. (IEA, 2019) This heavy reliance on fossil fuels poses significant environmental challenges, particularly due to greenhouse gas emissions and their contribution to global warming.

Hydrogen is currently used predominantly in industrial applications such as oil refining, and the production of ammonia, methanol, and steel—sectors where it has been employed for decades. This widespread use underscores the significant potential for decarbonization through the adoption of cleaner hydrogen alternatives. Despite its critical role in these traditional industries, hydrogen adoption in emerging applications—such as heavy industry, long-distance transport, and energy storage—remains limited, accounting for less than 1% of global demand, even though this segment grew by 40% compared to 2022. Most of the demand is still concentrated in refining. In 2023, global hydrogen demand exceeded 97 million tonnes (Mt) and is approached 100 Mt in 2024.

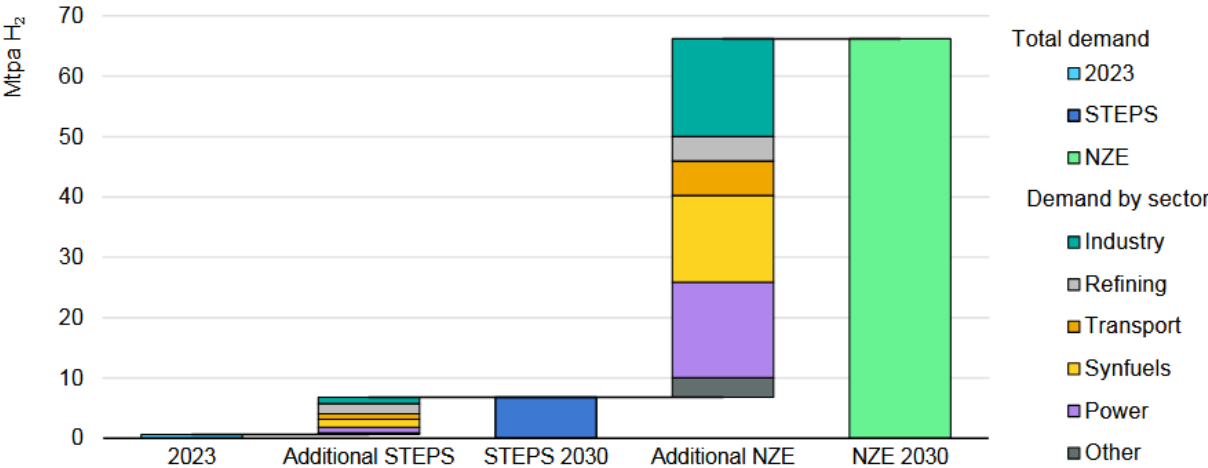


Figure 1.1: Low-emissions hydrogen demand by sector in 2023, and in the Stated Policies Scenario and the Net Zero Emissions by 2050 Scenario, 2030 (IEA, 2024).

However, this growth is largely driven by broader economic trends rather than targeted policy implementation. As an example, low-emissions hydrogen demand has been increased since it is a critical component in the global transition toward net-zero emissions. Low-emissions hydrogen is produced either through electrolysis powered by renewable electricity or from fossil fuels combined with carbon capture and storage (CCS).

Unlike conventional hydrogen production from unabated fossil fuels, which generates significant greenhouse gas emissions, low-emissions hydrogen offers a cleaner alternative that can substantially reduce the carbon footprint across multiple sectors. However, its current cost remains significantly higher than that of hydrogen from fossil fuels, limiting its adoption by existing users and delaying its uptake in new applications where it could replace direct fossil fuel use. Without targeted policy measures to reduce this cost gap or create strong market incentives, demand is likely to remain confined to early adopters—typically companies with

ambitious climate targets or those engaging in pilot projects to gain experience with the technology. Fig 1.1 shows an overview of low-emissions hydrogen demand by sector in 2023, and the needed scenario that would be needed of the Stated Policies Scenario and the Net Zero Emissions by 2050. It is underlined how the demand for low-emissions hydrogen, even if grown by nearly 10% in 2023, remains below 1 Mt.

Nonetheless, recent government actions—including mandates, incentive programs, and market development tools—could increase demand to over 6 Mt per year by 2030 reaching about 65 Mtpa. While this marks a significant improvement, it still accounts for only about one-tenth of the volume required to meet the Net Zero Emissions by 2050 (NZE) Scenario. Efforts to accelerate hydrogen adoption include public tenders and collaborative initiatives to aggregate demand for hydrogen and hydrogen-based fuels and feedstocks. In 2023, several large-scale low-emissions hydrogen projects—intended for refining, chemical production, and steelmaking—reached final investment decision (FID) status. These projects could collectively produce up to 1.5 Mt of low-emissions hydrogen annually by 2030, tripling current levels. Transport trends vary by subsector: momentum in road transport is shifting from passenger vehicles to heavy-duty trucks, while interest in hydrogen-derived fuels is increasing in shipping and aviation, especially where they are supported by policy. Nonetheless, limited market penetration has led to the cancellation of some high-profile supply projects. The environmental impact of hydrogen depends significantly on its production route—namely, the raw materials, energy source, and specific method used. Analysing those factors, a categorization of hydrogen has been considered, attributing a colour to each different type. Table 1.2 summarizes each category.

Table 1.2: *Types of hydrogen classified by colour*

<i>Colour</i>	<i>Feedstock</i>	<i>Primary energy source</i>	<i>Technology</i>
White	Nature	Natural	Fracking
Grey	Fossil fuels	Fossil fuels	Reforming
Blue	Natural gas	Fossil fuels	Reforming with CCS
Green	Water	Renewable energies	Electrolysis
Purple	Water	Nuclear energy	Electrolysis
Yellow	Water	Grid electricity	Electrolysis
Black/Brown	Coal	Fossil fuels	Gasification

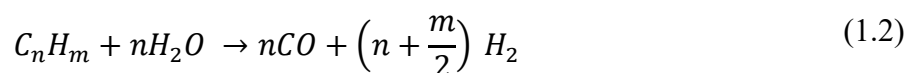
A key distinction in hydrogen production lies in the use of renewable versus non-renewable primary energy sources. Hydrogen can be produced from fossil fuels, biomass, water, or a combination of these. Currently, hydrogen production accounts for 2% of global primary energy demand. Natural gas is the dominant source, supplying approximately 75% of the 65 million tonnes (MtH₂) of dedicated global hydrogen production and consuming around 205 billion cubic meters of gas annually. Coal follows, contributing 23% and using 107 Mt of coal, while the remainder comes from heavy oils, naphtha, and electricity-based methods. These figures highlight hydrogen's current reliance on fossil fuels, which results in significant CO₂ emissions: around 10 tCO₂/tH₂ from natural gas, 12 tCO₂/tH₂ from oil products, and 19 tCO₂/tH₂ from coal. The Middle East is a key player – it produces 20% of all the hydrogen from unabated natural gas – with the United States and China together contributing around one-quarter. In addition, more than 15% of hydrogen globally is produced as a by-product in refineries and in the petrochemical industry, from processes such as naphtha reforming.

1.2.2 Hydrogen production from fossil feedstock

Hydrogen production methods are a subject of significant industrial interest. Despite the recent emphasis on green hydrogen, most of the global hydrogen is still derived from fossil sources through well-established thermochemical processes. Among these, reforming technologies, particularly those utilizing natural gas, represent the most mature and widely deployed solutions due to their high efficiency, scalability, and well-developed infrastructure. However, a common drawback across all fossil-based routes is the generation of carbon dioxide, either directly from the reforming reactions or indirectly through the combustion of fuels required to sustain these highly endothermic processes. Additionally, carbon monoxide is often formed as a by-product, which not only contributes to environmental concerns but also acts as a poison to catalysts used in downstream hydrogen purification. To mitigate this, the CO content is typically reduced via the water-gas shift (WGS) reaction, converting CO into CO₂ while generating additional hydrogen. The three principal reforming technologies used at industrial scale are Steam Methane Reforming (SMR), Partial Oxidation (POX), and Autothermal Reforming (ATR). Each of these technologies offers distinct thermodynamic and operational characteristics, with trade-offs in terms of hydrogen yield, energy consumption, and CO₂ emissions. In parallel, coal gasification remains a significant hydrogen source, particularly in countries with large coal reserves, although it is increasingly scrutinized for its high carbon intensity.

The following sections examine these major hydrogen production technologies in detail, starting with Steam Methane Reforming (SMR), followed by Partial Oxidation (POX), Autothermal Reforming (ATR), and finally Coal Gasification, with a focus on their underlying chemical reactions, operational conditions, efficiencies, and.

1. **Steam methane reforming (SMR)** is a thermochemical process in which hydrocarbon fuels react with steam at elevated temperatures, typically between 700 and 900°C, in the presence of a catalyst—often Nickel (Ni). Common feedstocks for this process include NG, light and heavy naphtha. Among these, NG is the preferred choice due to its high hydrogen output and reduced formation of carbon-rich byproducts compared to heavier hydrocarbons. As illustrated in Equation 1.2, steam reforming involves the reaction of a given hydrocarbon with water vapor to produce synthesis gas (syngas), a mixture primarily composed of hydrogen (H₂) and carbon monoxide (CO).

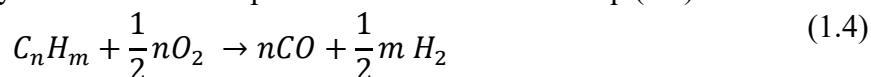


As already mentioned, the produced carbon monoxide must be converted and that can be done by the water gas shift reaction (WGS) a catalytic process that converts CO into carbon dioxide (CO₂) while simultaneously generating additional hydrogen:



SMR is strongly endothermic, requiring continuous heat input to maintain the necessary reaction conditions. For example, the steam methane reforming (SMR) has a heat of reaction of $\Delta H = 206 \text{ kJ mol}^{-1}$. Water gas shift on the other hand is mildly exothermic $\Delta H = -41 \text{ kJ mol}^{-1}$. (Ming et al. 2002)

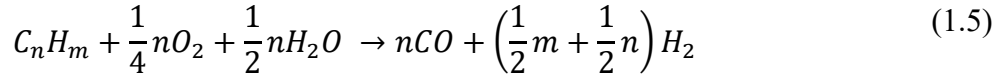
2. **Partial oxidation (POX)** is a process in which hydrocarbon fuels are reacted with a limited amount of oxygen, insufficient for complete combustion. POX occurs without a catalyst at 1200-1400°C and about 40-80 bar. Unlike full combustion, which fully oxidizes the fuel to carbon dioxide and water, partial oxidation generates a mixture of syngas: hydrogen (H₂) and carbon monoxide (CO). The general equation of POX reaction for any hydrocarbon with a specific carbon chain is as Eq. (1.4):



The main advantage of partial oxidation is its rapid reaction rate and reduced need for external heat, as the process is exothermic. However, it generally produces less hydrogen per unit of fuel compared to steam reforming and may require additional gas treatment steps to optimize hydrogen yield and purity. The partial oxidation which uses natural gas as a feedstock has a heat of reaction of $\Delta H = -35.7 \text{ kJ mol}^{-1}$.

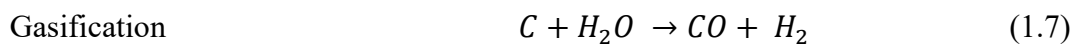
3. **Autothermal Reforming (ATR)** represents the third major method of hydrogen production and combines the principles of both partial oxidation (POX) and steam reforming (SR) within a single reactor. In this process, steam is introduced alongside a

hydrocarbon feedstock—typically methane—and a limited amount of oxygen. The partial oxidation reaction, which is exothermic, provides the thermal energy required to drive the endothermic steam reforming reaction, allowing both to occur simultaneously under controlled conditions. This integration enhances the overall efficiency of the process by eliminating the need for external heat sources, thus overcoming one of the main limitations of conventional steam reforming. Eq. (1.5) shows the general form of ATR.



A key distinction between ATR and POX is the presence of a fixed catalytic bed located before the combustion zone in ATR reactors. This catalyst promotes steam reforming reactions prior to or in conjunction with the partial oxidation, improving hydrogen yield and process control. By incorporating steam into a reaction environment where partial oxidation is already taking place, ATR not only benefits from thermal self-sufficiency but also improves the hydrogen yield compared to standalone POX, which typically produces a syngas with a lower hydrogen-to-carbon ratio. Furthermore, ATR offers operational flexibility, as the hydrogen-to-carbon monoxide ratio in the syngas can be tuned by adjusting the steam-to-carbon and oxygen-to-carbon ratios. Due to its high throughput and energy integration, ATR is particularly well-suited for large-scale applications such as ammonia or methanol synthesis and integrated gasification systems.

The second largest source of hydrogen is given by the coal gasification technology. Hydrogen production from unabated coal gasification accounted for 20% of the global total in 2023. It is a thermochemical method where coal, is converted into a mixture of gases primarily composed of hydrogen and carbon monoxide. It is considered an alternative to conventional combustion and is especially relevant in regions with abundant coal resources. China alone accounts for most of the coal-based hydrogen production, driven by its abundant coal reserves and lower reliance on natural gas imports. The process involves reacting coal at high temperatures, typically 800–1300 °C, and 30-70 bar with a controlled amount of oxygen and/or steam in an oxygen-deficient environment, preventing full combustion (Panda et al. 2023). The general reactions are:



While it enables the utilization of coal for cleaner fuel production, the process is carbon-intensive, resulting in significant CO₂ emissions if not coupled with carbon capture and storage

(CCS) technologies. It generates solid and liquid waste streams that require careful environmental management. Its application is indeed minimal in Europe and North America, where environmental regulations and carbon pricing mechanisms strongly disincentivize carbon-intensive processes. (IEA, 2024).

1.2.3 Green hydrogen production

The methods discussed so far rely on fossil fuels as feedstocks and are therefore primarily used to produce grey hydrogen—or blue hydrogen when carbon capture and storage (CCS) is implemented. However, recent decarbonization trends and regulatory pressures are driving the development of alternative methods aimed at reducing greenhouse gas emissions, with a particular focus on using renewable feedstocks. Among these, water stands out as a promising candidate due to its abundance, low environmental impact, and potential for integration with renewable energy sources. Water splitting produces hydrogen and oxygen through a series of chemical reactions. As such, water-based hydrogen production represents a crucial pathway in the transition toward sustainable energy systems, particularly when powered by solar, wind, or hydroelectric energy.

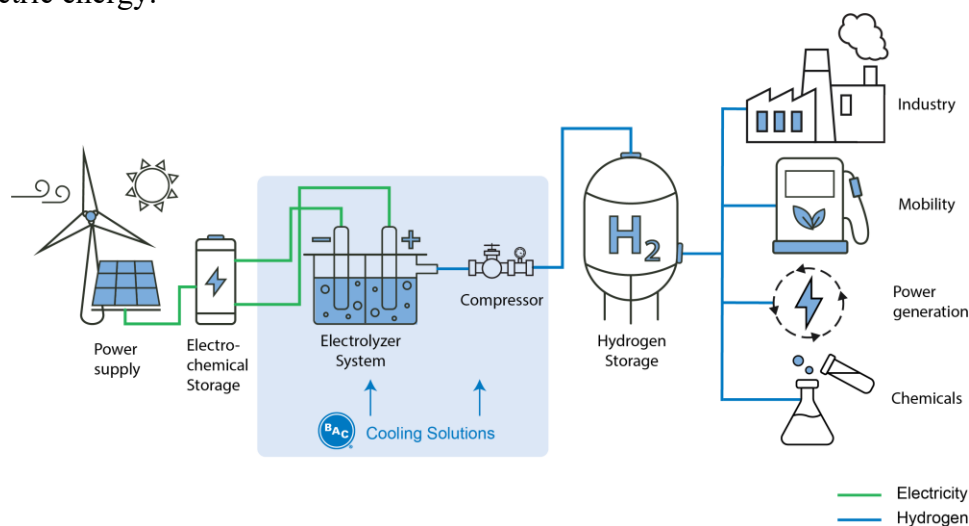
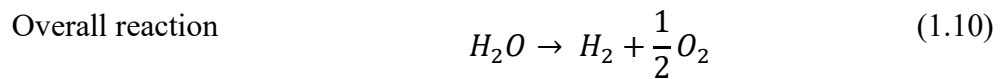
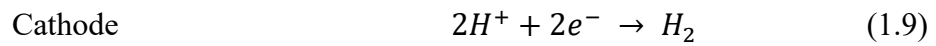
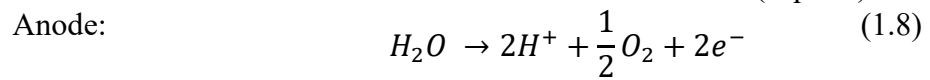


Figure 1.2: Green hydrogen production route via electrolysis (Baltimore Aircoil Company, 2025).

Water electrolysis is currently considered the most effective zero-emission technology for hydrogen production, particularly when powered by renewable electricity sources (El-Shafie, 2023). Among the various electrolysis technologies, polymer electrolyte membrane (PEM) water electrolysis—employing an ion-exchange membrane—stands out for its high efficiency and ability to produce high-purity hydrogen. This method offers several advantages, including the absence of pollutant emissions, high hydrogen purity, and compatibility with a wide array of renewable energy inputs. Furthermore, water electrolysis has been applied in industrial settings for many years, demonstrating its technical feasibility and reliability. The production cost of green hydrogen via electrolysis is heavily influenced by the cost of renewable electricity, which remains a key factor in determining economic viability. In addition to its technical

benefits, water electrolysis is particularly well-suited for integration with intermittent renewable sources, enabling flexible and decentralized hydrogen generation. Nevertheless, the process is not without challenges. One major limitation is its relatively high energy consumption in conventional industrial applications, which ranges between 4.5 – 5.5 kWh/Nm³ of H₂ produced. Moreover, the requirement for fresh water as the primary input to the electrolyser raises concerns, especially in arid regions. The availability of water may become a bottleneck in the large-scale deployment of electrolytic hydrogen production. Approximately 40% of the projected global low-emission hydrogen production by 2030 is expected to occur in water-stressed regions. The electrochemical decomposition process of water occurs according to anodic and cathodic evolution reactions which lead to the overall reaction (Eq. 1.8):



From the data carried out by the article of (Tahmasbi et al. 2025) is retrieved figure 1.3 using MATLAB. It presents a comparative analysis of the costs (in \$/kg H₂) and efficiencies (%) of the five cited hydrogen production methods: Steam Reforming (SR), Partial Oxidation (POX), Autothermal Reforming (ATR), Coal Gasification, and Electrolysis.

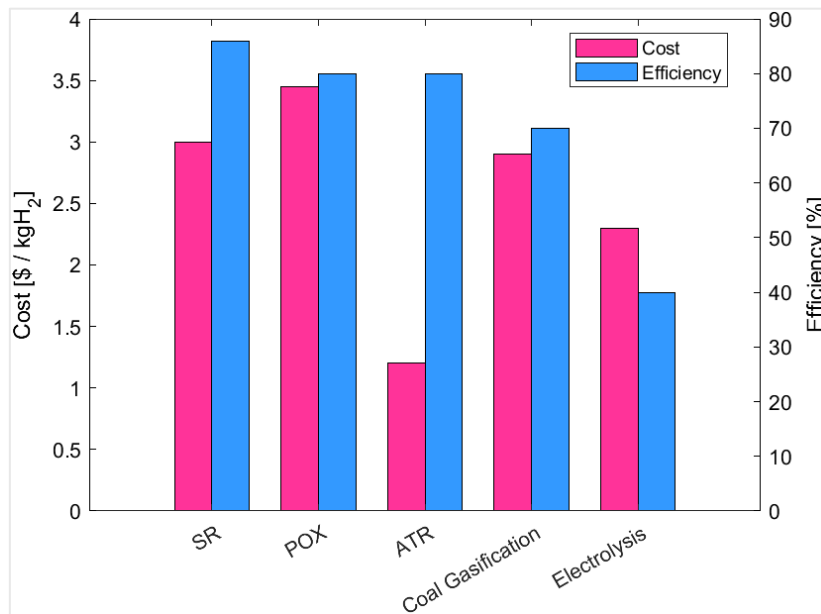


Figure 1.3: The costs of hydrogen production for the major five production methods (Tahmasbi et al. 2025).

From the graph, it is evident that steam reforming (SR) exhibits the highest efficiency, reaching approximately 85%, while maintaining a relatively moderate cost of around 2.5 \$/kg H₂. This performance underscores why SR is currently the dominant method in the hydrogen industry,

balancing both economic and energetic effectiveness. Partial oxidation (POX), although similar in cost (~3.5 \$/kg H₂), shows slightly lower efficiency than SR. Despite its fast reaction rate and simpler reactor design, its hydrogen yield is lower, which contributes to a higher cost per unit of hydrogen produced. Autothermal reforming (ATR) emerges as the least expensive option, with production costs close to 1.5 \$/kg H₂, making it economically attractive for large-scale applications. However, its efficiency is somewhat lower than SR and POX, estimated around 70–75%. This reflects the thermal trade-off inherent in ATR’s integration of exothermic and endothermic reactions. Coal gasification shows a cost comparable to SR (~2.5 \$/kg H₂), but with noticeably lower efficiency—around 60%. This, combined with its high CO₂ emissions, makes it less desirable from both an environmental and energy-efficiency perspective, particularly in regions with carbon pricing policies. Finally, electrolysis, the only non-fossil-based method shown, has a higher production cost (~2.5 \$/kg H₂) and an efficiency of about 40%. Despite these drawbacks, it remains the most promising option for green hydrogen production, particularly when powered by low-cost renewable electricity. The higher cost reflects the current expense of electrolyser systems and the energy-intensive nature of the process.

1.3 Electrified steam methane reforming (e-SMR)

Steam methane reforming is the most common of the reactions used to produce hydrogen since methane is the principal component of natural gas. When reformed, it yields a greater amount of hydrogen per unit of carbon emitted compared for example to naphtha. This improves the hydrogen yield and reduces the relative production of carbon-based byproducts such as CO₂ and soot. The process is highly efficient and cost-effective but is also carbon-intensive, as it relies on the combustion of fossil fuels to provide the necessary heat to satisfy the endothermicity of the reaction. As a result, SMR is responsible for substantial CO₂ emissions produced during the fuel combustion in a furnace, necessary to provide heat to the reaction and during the water gas shift reaction. These emissions make the SMR incompatible with long-term decarbonization goals unless coupled with carbon capture and storage (CCS). The reaction holds in the following way:



In industrial applications, steam methane reforming reactors are typically designed as tubular fixed-bed systems integrated within a fired furnace. The reformer consists of an array of a huge number of vertically or horizontally arranged tubes. They are fabricated from high-temperature resistant material such as alloy HK-40 with a high content of Ni-Cr. These tubes are packed with a nickel-based catalyst, commonly Ni/Al₂O₃, which facilitates the endothermic reforming reactions (Rostrup-Nielsen et al., 2002). The radiant section of the furnace provides the thermal

energy needed to sustain the reaction, operating at temperatures between 800 and 950 °C using burners placed above or beside the tubes. Above the radiant zone, the convection section serves to recover heat from the flue gases, which is used to preheat the feed components—primarily NG, steam, and boiler feedwater—thereby improving the overall thermal efficiency of the process (Towler & Sinnott, 2013). Heat required for steam methane reforming (SMR) is typically supplied by the combustion of a mixture of natural gas and tail gases from PSA. This combustion must occur at temperatures significantly higher than the reaction temperature to provide the necessary inward heat flux for the endothermic process. Conventional SMR results in the emission of approximately 9 to 10 metric tons of CO₂ per metric ton of hydrogen produced, with 30% to 40% of these emissions directly attributed to hydrocarbon combustion (Wismann et al., 2019). A major limitation in steam methane reforming (SMR) is the inefficient heat transfer caused by the strongly endothermic nature of the reaction and the low thermal conductivity of both the catalyst and reactor walls. These factors lead to steep temperature gradients within the reactor and catalyst bed, which not only limit catalytic efficiency but also increase the risk of carbon deposition and thermal stress, ultimately reducing reactor lifespan. In industrial applications, intrinsic catalytic activity is generally not the limiting factor; rather, the challenge lies in maintaining uniform heat distribution to ensure optimal catalyst utilization and stable reactor performance. To mitigate steep temperature gradients, efforts have been made to optimize the reactor design by selecting tube diameters within a range of 100 to 150 mm. However, even with this optimization, less than 10% of the available catalytic activity is typically utilized (Wismann et al., 2019).

The major improvement analysed, aimed at reducing CO₂ emissions and addressing the limitations of low thermal conductivity in endothermic processes has explored various strategies. These include the development of novel materials with enhanced thermal conductivity, the design of alternative reactor configurations, approaches to lower reaction temperatures by shifting the thermodynamic equilibrium, reducing characteristic heat transfer length scales, and the direct heating of catalytic nanoparticles via induction. Alternatively, electrical heating of an integrated, catalytically coated heating element enables reactor temperatures that surpass those attainable in conventional reactors. This method also offers significantly improved dynamic performance, reducing start-up times to just a few minutes. In a typical electrically heated reformer configuration, the endothermic reforming reactions are facilitated either by indirect electric heating—where external resistive or inductive elements supply heat to the reactor tubes—or by direct Joule heating, in which current is passed through electrically conductive reactor components or structured catalysts. These systems preserve the fundamental architecture of packed-bed reactors whose tubes are filled with catalysts but eliminate the need for a fired furnace, thereby reducing direct CO₂ emissions and enhancing process controllability. As an example, in 2020 SYPOX deliver a patent of how it is structured

an e-SMR reactors with ceramic catalyst. Figure 1.4 shown that this reactor consists of a shell filled with insulation to minimize heat losses, enclosing a reactive mixture duct where the feed gases flow.

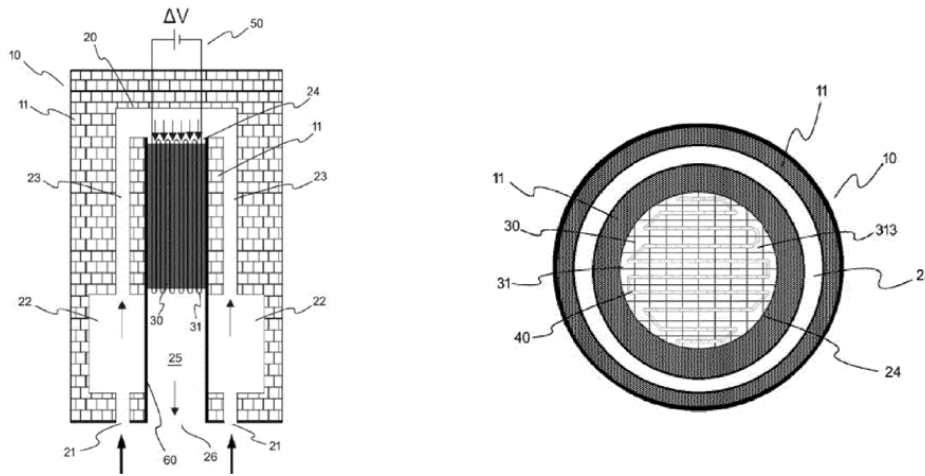


Figure 1.4: Electrified steam reforming reactor configuration. On the left is shown a longitudinal view. On the right a cross-sectional view.

Within this duct, a structured ceramic catalyst—often in a monolithic or foam-like configuration—is employed to catalyse steam reforming, but also other types of reactions such as steam reforming, dry reforming, steam cracking, ammonia and cracking. Crucially, this structured catalyst is equipped with embedded electrical heating means powered by at least two insulated electrical feeds that pass through the reactor shell. These feeds are connected to an external power supply, which delivers the electrical energy needed to heat the catalyst to the desired reaction temperature. This architecture enables direct Joule heating of the catalyst, allowing precise thermal control. The reactive gas mixture enters the duct, contacts the heated catalyst, and exits the reactor after undergoing the targeted reaction. A significant advantage of electrified reactors lies indeed in their more uniform and localized heat distribution, which greatly reduces the risk of hot spots—a common issue in flame-heated systems that can accelerate catalyst sintering and thermal degradation. As illustrated in Figure 1.5, conventional fired reformers require the external wall temperature to be substantially higher than the target reaction temperature to ensure adequate heat transfer across thick tube walls and catalyst beds. This leads to steep thermal gradients and uneven heating. In contrast, electrically heated reactors can deliver energy directly at or near the reaction zone, allowing operation closer to the desired process temperature and thus avoiding thermal overshoot (Wismann et al., 2019). This not only improves thermal efficiency but also extends catalyst lifetime and enhances safety.

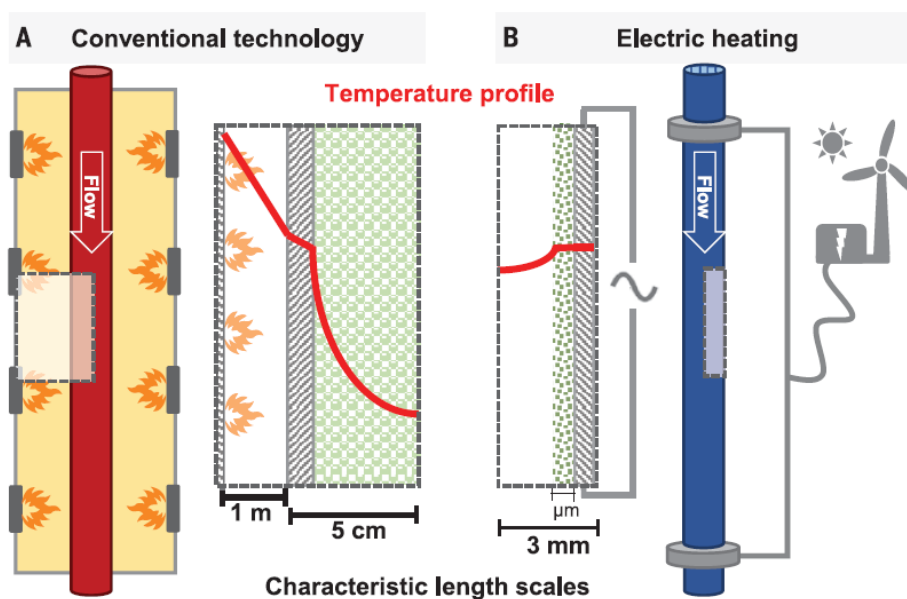


Figure 1.5: Heating principles. (A) Conventional fired reactor. (B) Electrical resistance-heated reactor. Characteristic radial length scales and temperature profiles are shown across the heat source, reactor wall (grey), and catalyst material (green). In (B), the heat source and reactor wall are one.

The electrification of steam methane reforming, through uniform heating and the potential for highly compact reactor designs, represents a disruptive solution to the challenges of CO₂ emissions and the limitations of current reactor design, operation, and process integration. Beyond reducing carbon emissions, integrating resistance-heated reactors into existing plants may enable alternative operating conditions, such as lower steam-to-carbon ratios or higher methane conversions—typically constrained by carbon formation and material temperature limits. Higher methane conversion, combined with innovative purification technologies, could also provide a localized CO₂ stream for other industrial applications. The efficiency of resistance-heated reformers and their reduced need for heat recovery make them suitable across a wide range of scales, supporting decentralized hydrogen production by leveraging existing infrastructure for natural gas and potentially biogas. Furthermore, their low thermal mass enables rapid adaptation to fluctuating renewable energy supplies, with possible start-up times of just a few seconds, making them ideal for intermittent operation. Operating costs for electrified reformers are primarily influenced by electricity prices, natural gas costs, and CO₂ taxes. Preliminary analyses suggest that in regions with abundant renewable electricity, resistance-heated reformers could be cost-competitive with conventional fired systems. This approach underscores the transformative potential of electrifying core industrial processes. With the continuous decline in renewable electricity costs, resistive heating emerges as both an environmentally and economically attractive option for supplying the heat demands of strongly endothermic reactions in the transition toward a more sustainable industrial future.

A recent study (Maporti et al., 2024) evidence the effect of the factors previously cited. Two configurations of e-SMR were developed. In the first one an electrified reactor is integrated with a convective SMR, using extra heat for electricity production via high super-heated steam avoiding any usage of fuel to provide the heat necessary for the reaction. The alternative configuration incorporates CO₂ capture from the syngas, which helps to reduce CO₂ emissions from the process. Both configurations are benchmarked with conventional fuel fired reforming respectively without (first configuration) and with (second configuration) a CCS integration. To understand the effect of electricity price and the price of natural gas feedstock on the levelized cost of hydrogen (LCOH, EUR Nm⁻³), sensitivity analyses were carried out and they are reported in figure 1.6 and 1.7.

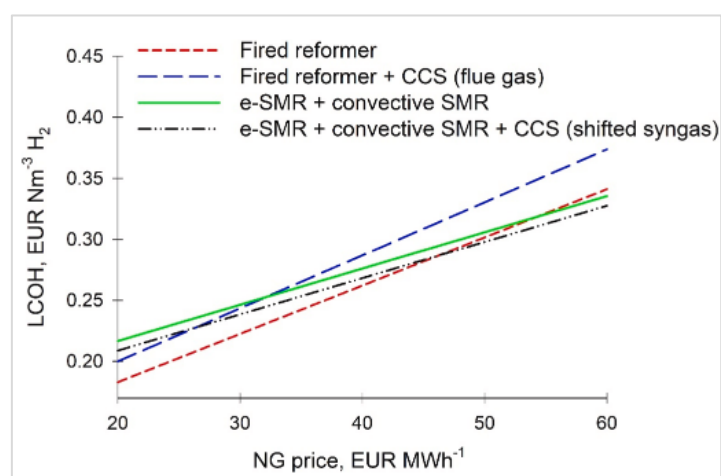


Figure 1.6 Impact of the NG price on the LCOH in the different process configurations (Maporti et al., 2024).

The graph shows that natural gas price significantly affects all the configurations studied. Focusing on the configuration without the CCS and it is evident that it is less competitive compared it with its respective benchmark of fuel-fired reformer at least when the price is under 50 EUR MWh⁻¹.

From figure 1.6 can be seen how the LCOH of the fired reformer decreases with increasing electricity prices. That is mainly due to the fact the processes export electricity to the grid. In particular, the LCOH of the fired reformer without CO₂ capture decreases steeply. On the other hand, the electrified configurations show an increase in LCOH with an increase in electricity prices.

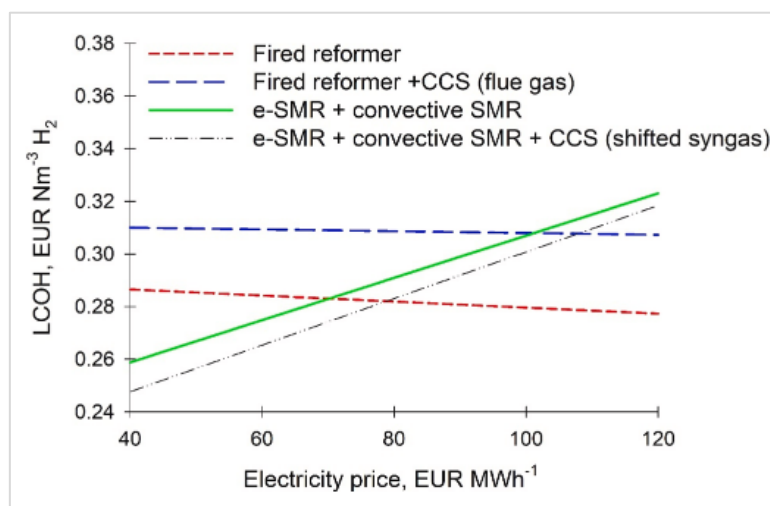


Figure 1.7: Impact of the electricity price on the LCOH in the different process configurations (Maporti et al., 2024).

This data identifies how the electrified reactors technology can be pushed over with a large dependency on the prices of energy. In that way countries that can itself produce electricity with renewable resources get a great advantage from this point of view (Khatib et al., 2022). By using low- or zero-carbon energy sources such as solar, wind, or hydro, e-SMR can produce low-emission hydrogen comparable to green hydrogen from electrolysis. As renewable electricity prices continue to fall—often below €30/MWh in some regions—e-SMR becomes increasingly cost-effective, especially when operated flexibly during periods of low electricity prices.

Since the economics of electrified steam methane reforming (e-SMR) are heavily influenced by electricity prices, particularly from renewable sources, understanding regional energy cost trends is essential for evaluating the viability of e-SMR. According to the (IEA, 2025) electricity market report, EU wholesale electricity prices in 2024 averaged around USD 85/MWh, marking a 20% year-on-year reduction, but remaining over 40% higher than pre-COVID levels. Notably, electricity in the Nordics remained the cheapest in Europe at USD 40/MWh, thanks to strong hydropower generation, while France saw an average of USD 62/MWh, aided by recovering nuclear and hydropower output. In contrast, Germany’s prices were significantly higher, with spreads of about EUR 20–30/MWh over France, partly due to transmission constraints. Despite the decline in EU prices since the 2022 energy crisis, the price gap with the U.S. remains substantial: EU prices were still 130% higher than U.S. averages in 2024, and futures predict a spread of 160% in 2025. In the U.S., prices dropped to an average of USD 37/MWh, driven by falling natural gas prices and increased production also due to large usage of renewables (23%) and nuclear (18%) for the electricity generation. Elsewhere, Japan averaged USD 77/MWh, Australia saw USD 70/MWh, and India averaged USD 55/MWh, with most regions benefiting from increased renewable output or regulatory measures.

These trends highlight that the competitiveness of e-SMR varies greatly by region, being most promising where low-cost, low-carbon electricity is available. The primary challenge of electrified steam reforming is to compete with traditional technologies in terms of productivity due to the huge barriers to scaling them up into large plants. The scalability of e-SMR is limited by its substantial electricity demand, which must be met with low-cost, renewable power to maintain a low carbon footprint. In many regions, the high cost of renewable electricity undermines the economic viability of e-SMR, making conventional SMR with carbon capture more competitive. High capital costs for specialized equipment and the absence of proven industrial-scale e-SMR plants further hinder investment and adoption (Hydrogen Council, 2023). Yet rather than being solely a limitation, the inherent challenges of scaling e-SMR can also be viewed as an opportunity to promote decentralized hydrogen production. Small-scale, modular e-SMR units offer distinct advantages: they are easier to deploy, require lower initial capital investment, and can be sited near renewable energy sources, such as solar or wind farms. Such modular systems can directly integrate with renewable electricity, allowing for flexible, low-carbon hydrogen production without the need for extensive electrical infrastructure. These decentralized e-SMR units are particularly well-suited for industrial sites, remote areas, and hydrogen refuelling stations, where localized production can minimize transportation costs and reduce carbon footprints. Additionally, their compact design and rapid response capability make them ideal for balancing intermittent renewable energy supply, further enhancing their economic and environmental benefits.

This shift from a centralized to a decentralized model aligns with broader trends in the energy sector, where distributed renewable energy sources are increasingly favoured over large, centralized power plants. By embracing modular e-SMR technology, the hydrogen industry can achieve greater flexibility, resilience, and sustainability, leveraging the advantages of electrified reforming without being constrained by the challenges of large-scale deployment.

1.4 Biogas as a hydrogen production feedstock

The adoption of renewable energy sources in the industry is steadily increasing, driven by their potential to promote sustainable development, minimize environmental pollution, and enhance domestic energy security. In the context of hydrogen production, renewable energy sources play a critical role in generating low-emission energy, a demand that has been steadily increasing in recent years. In that context, biogas is a valid alternative since it is considered a sustainable and renewable fuel (EPA, 2014), and it is suitable for a direct conversion to syngas. Biofuels are fuel originates from biomass which is the source of bioenergy.

1.4.1 Biomass

Biomass, derived from organic materials like wood, agricultural residues, and waste, is a renewable energy source with variable composition and seasonal availability. It is classified into lignocellulosic, carbohydrate-, lipid-, and protein-rich types, each affecting conversion efficiency (George et al., 2024). Traditional combustion is inefficient due to biomass's low calorific value (14–17 MJ/kg), prompting the development of advanced thermochemical and biochemical conversion methods (Anastas & Warner, 1998). Biofuels, derived from biomass, are categorized into four generations based on feedstock and sustainability—from food crops (1st gen) to GMOs and carbon capture-integrated processes (4th gen). Biofuels exist in solid, liquid, and gaseous forms. Liquid biofuels include bioethanol, biodiesel, green diesel, and other blends, while gaseous biofuels include biogas and syngas, produced via anaerobic digestion or gasification. Biogas (40–75% methane) can be upgraded to biomethane (≈ 36 MJ/m³ LHV), offering a higher energy content and cleaner combustion (IEA, 2020). While biochemical conversion is more widely adopted, all biofuel types require pre-treatment and purification to ensure efficient and sustainable energy production.

1.4.2 Biogas reforming

Biogas reforming is a critical process for converting renewable biogas into valuable syngas (a mixture of hydrogen and carbon monoxide), which can serve as a feedstock for producing a wide range of chemicals and fuels as hydrogen and methanol. The reforming process leverages the main components of biogas, primarily methane (CH₄) and carbon dioxide (CO₂), in various reaction pathways to produce syngas. The three primary types of reforming methods used for biogas conversion are dry reforming, bi-reforming, and tri-reforming (Zhao et al., 2020).

- Dry reforming of biogas is a process that involves the reaction of methane (CH₄) with carbon dioxide (CO₂) to produce syngas (a mixture of H₂ and CO) through the following reaction:



This process is highly endothermic, requiring a significant amount of energy input, typically at temperatures ranging from 700°C to 900°C. The primary advantage of dry reforming is its ability to directly use CO₂, a greenhouse gas, as a reactant, making it a method for both energy production and carbon capture. However, the process is also associated with challenges such as carbon deposition (coke formation) on the catalyst surface, which can lead to catalyst deactivation over time. Researchers have focused on

developing advanced catalysts, such as nickel-based catalysts supported by CeO₂, ZrO₂, and Al₂O₃, to enhance the stability and efficiency of dry reforming.

- Bi reforming, also known as steam biogas reforming, is a process that combines dry reforming and steam reforming in a single process, allowing the simultaneous use of CO₂ and H₂O as oxidants for methane conversion. The main reactions involved are:



By adjusting the ratios of CO₂ and H₂O, the H₂/CO ratio in the resulting syngas can be tuned to meet specific requirements for downstream applications, such as Fischer-Tropsch synthesis or methanol production. Bi reforming is less prone to carbon formation than dry reforming because the steam present helps oxidize carbon deposits on the catalyst surface. Typical operating conditions are slightly milder than dry reforming, with temperatures of 750°C to 850°C.

Tri-reforming is an advanced technique that combines dry reforming, steam reforming, and partial oxidation of methane in a single process. The key reactions involved are:



Tri-reforming is a highly flexible process, offering the benefits of each reforming method while overcoming their individual limitations. The presence of both steam and oxygen helps reduce carbon deposition on the catalyst, while partial oxidation provides additional heat, reducing the overall energy input required. This method also allows for precise control over the H₂/CO ratio, making it suitable for various syngas applications. The process is generally operated at temperatures between 800°C and 900°C.

1.4.3 Biogas global consumption

Bioenergy is the largest source of renewable energy globally, accounting for 45% of total renewable energy consumption. In 2020, it contributed 12.6% of the total final energy consumption worldwide, encompassing both traditional uses such as wood and charcoal in open fires, and modern applications, including biofuels, biogas, and biomass used in advanced systems (REN21, 2023). Despite its significant role in the renewable energy mix, biogas and biomethane currently account for less than 3% of total bioenergy demand and only 0.3% of

total primary energy. Globally, there are approximately 18 GW of installed power generation capacity running on biogas, primarily located in Germany, the United States, and the United Kingdom. From 2010 to 2018, this capacity grew at an average rate of 4% per year. However, deployment has slowed in recent years in some regions, including the United States and Europe, mainly due to changes in policy support. In contrast, growth has accelerated in emerging markets such as China and Turkey.

Biogas is predominantly used for electricity and heat generation, with nearly two-thirds of production dedicated to these purposes—split roughly evenly between electricity-only and cogeneration facilities. Around 30% is consumed in residential buildings for cooking and heating, while the remainder is upgraded to biomethane for injection into gas networks or use as transport fuel. The cost of generating electricity from biogas varies depending on feedstock type and plant sophistication, ranging from USD 50 to USD 190 per megawatt-hour (MWh). This range is generally higher than the cost of wind and utility-scale solar photovoltaic (PV) power, which have seen sharp cost reductions in recent years. Consequently, the shift from feed-in tariffs to technology-neutral renewable electricity auctions (such as power purchase agreements) in many countries may limit the growth of electricity-only biogas plants. However, unlike wind and solar PV, biogas plants can operate flexibly, providing grid-balancing and ancillary services—an advantage that, if properly valued, could enhance their future deployment. Despite these challenges, biogas and biomethane have the potential to play a greater role in the energy transition. They offer the benefits of natural gas—such as storage, flexibility, and high-temperature heat—without the associated carbon emissions. This characteristic becomes increasingly valuable as economies strive to decarbonize. Moreover, biogas provides a sustainable source of heat and power, particularly for communities seeking local, decentralized energy supplies, and serves as a reliable cooking fuel in developing countries. The environmental benefits of biogas extend beyond energy production. By capturing and using methane—a potent greenhouse gas (GHG) that would otherwise be released from decomposing organic waste—biogas significantly reduces GHG emissions. It also supports waste management, improves resource efficiency, and can enhance energy security by replacing gas transported over long distances. Additionally, biogas and biomethane contribute to nutrient recycling, rural job creation, and the promotion of circular economy principles, particularly when developed in partnership with the agricultural sector.

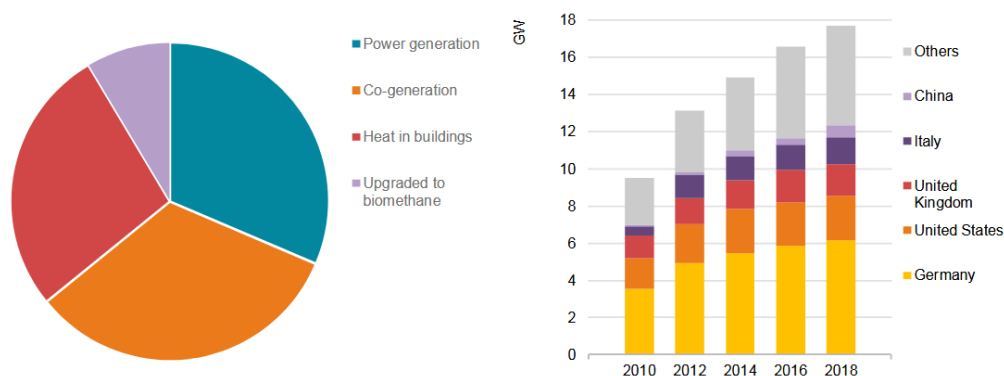


Figure 1.8: (A) Biogas consumption by end use, 2018. (B) Biogas installed power generation capacity, 2010-18.

Effective policies can unlock the full potential of biogas and biomethane, but their future will depend on the availability and cost of these low-carbon gases. Strategic support can help these renewable fuels become a vital part of a sustainable energy system.

1.5 Carbon capture and storage

Currently, Carbon Capture and Storage (CCS) facilities worldwide have a combined capacity to capture over 40 million metric tons of CO₂ (MtCO₂) annually. While this represents a significant technological achievement, it remains marginal when compared to global CO₂ emissions, which are approximately 37.8 gigatonnes (GtCO₂) per year (IEA, 2024). Some of these facilities have been in operation since the 1970s and 1980s, beginning with natural gas processing plants in the Val Verde region of Texas. These early facilities supplied captured CO₂ to local oil producers for use in enhanced oil recovery (EOR) operations, demonstrating the initial commercial application of CCS technology (IEA, 2021). The deployment of CCS is underpinned by various capture technologies, including pre-combustion, post-combustion, and oxy-fuel combustion methods, each tailored to specific industrial applications. The captured CO₂ can then be transported through pipelines or ships to suitable storage locations, which range from depleted oil and gas fields to deep saline aquifers and basalt formations. Storage safety and integrity are ensured through continuous monitoring and the use of advanced sealing techniques. Despite its potential, the adoption of CCS is challenged by high costs, energy consumption, and regulatory uncertainties. However, ongoing research and innovation continue to enhance its efficiency and cost-effectiveness. This section will explore the fundamental principles of CCS, its technological advancements, and its role in the global strategy for climate mitigation.

1.5.1 Routes for CO₂ capture

CO₂ capture technologies can be categorized into three main types: pre-combustion capture, oxy-fuel combustion capture, and post-combustion capture. These methods differ in their underlying principles, technological maturity, fields of application, and commercial scalability:

- **Pre-combustion capture:**

Pre-combustion CO₂ capture is a method that focuses on the removal of carbon dioxide before the combustion of fossil fuels. This process begins with the gasification or reforming of fossil fuels, typically using air and water vapor. Following these reactions, the resulting gas mixture contains primarily CO₂ and H₂. These two gases are then separated using gas separation technologies, such as pressure swing adsorption (PSA), membrane separation, or cryogenic separation. The captured CO₂ can be stored or utilized, while the purified hydrogen is used as a clean fuel, for example, in hydrogen gas turbines for power generation. Pre-combustion capture offers several advantages over post-combustion methods. The higher concentration and pressure of CO₂ in the syngas stream facilitate more efficient separation processes, leading to lower energy consumption.

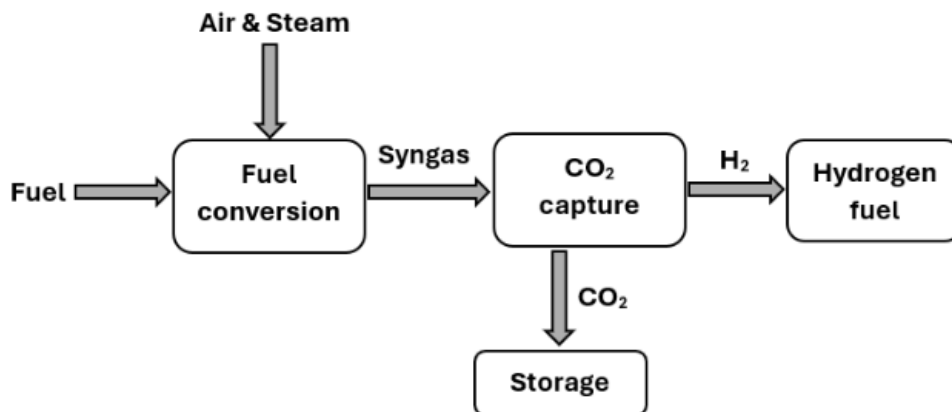


Figure 1.9: General pre-combustion CO₂ capture block flow diagram.

Studies indicate that pre-combustion capture can achieve CO₂ capture rates exceeding 90% (US department of energy, 2025). This technology is particularly suited for new power generation facilities, such as Integrated Gasification Combined Cycle (IGCC) plants and for new hydrogen plants based on steam methane reforming, where the infrastructure can be designed to accommodate the specific requirements of pre-combustion capture. The hydrogen produced can be used in various applications, including electricity generation, industrial processes, and as a transportation fuel. Pre-combustion CO₂ capture is associated with high capital costs due to the complexity of the technologies involved and the need for purpose-built infrastructure. The process requires converting fuels into synthesis gas through gasification or reforming, which

involves high-temperature, high-pressure equipment and advanced control systems. Additionally, effective CO₂ separation and hydrogen handling demand specialized units that must be integrated from the design stage. These requirements make pre-combustion capture feasible mainly for newly built plants, while retrofitting existing facilities is often economically unviable due to the extensive modifications needed.

- **Post-combustion capture:**

In post-combustion capture, CO₂ is removed after the combustion of fossil fuels.

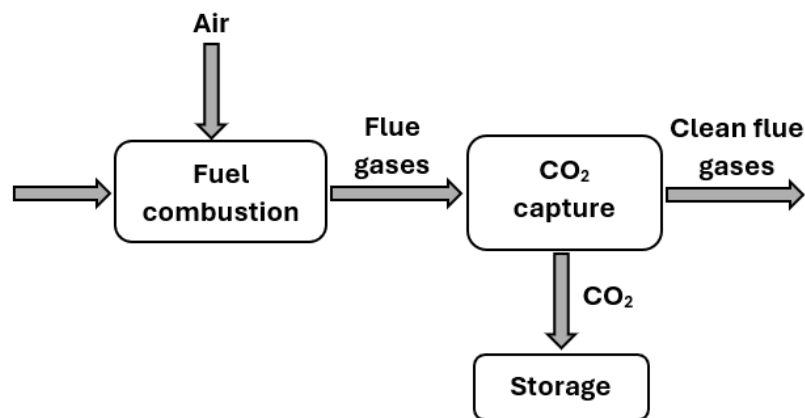


Figure 1.10: General post-combustion CO₂ capture block flow diagram.

This method involves capturing CO₂ directly from the exhaust (or ‘flue’) gases of power plants, industrial facilities or chemical plants. It is the most considered option for carbon capture because it can be retrofitted to existing power plants, making it a flexible solution for reducing emissions without significant modifications to the combustion process itself. The technology is well understood, with a long history of application in various industrial sectors, including natural gas processing, ammonia production, and hydrogen manufacturing (Hua et al., 2023). Despite its operational maturity, post-combustion CO₂ capture faces significant challenges primarily due to the low partial pressure of CO₂ in flue gas, which typically ranges from 0.03 to 0.15 bar, depending on the fuel type. This low driving force, combined with the high volumetric flow rates of flue gas—mainly composed of nitrogen—necessitates the handling of large gas volumes and results in substantial energy consumption for solvent regeneration and gas compression. In contrast, pre-combustion capture deals with syngas streams rich in CO₂ at pressures of 15–40 bar, which allows for more thermodynamically favorable separation. According to the work of Rochelle (2009), regeneration of MEA solvent in post-combustion systems requires approximately 3.5–4.0 GJ per ton of CO₂, leading to an energy penalty that can reduce the net efficiency of a coal-fired power plant by 8–12 percentage points. This substantial parasitic load underscores the importance of developing more energy-efficient solvents and process integration strategies to make

post-combustion capture viable at scale. However, continued research and development are driving down costs and improving performance, making post-combustion capture a key component of future carbon management strategies.

- **Oxy-fuel combustion capture:**

This carbon capture technology relies on the complete combustion of fossil fuels in an oxygen-rich environment, rather than in ambient air. By burning fuel in pure oxygen, the resulting flue gas primarily consists of carbon dioxide and water vapor. As an example, the SynCOR™ Autothermal Reformer (ATR) technology developed by Haldor Topsoe employs oxy-fuel combustion for carbon capture, using pure oxygen instead of air to produce a flue gas rich in CO₂ and H₂O, which significantly facilitates downstream CO₂ separation and capture. This high concentration of CO₂, with minimal impurities, significantly simplifies the capture process.

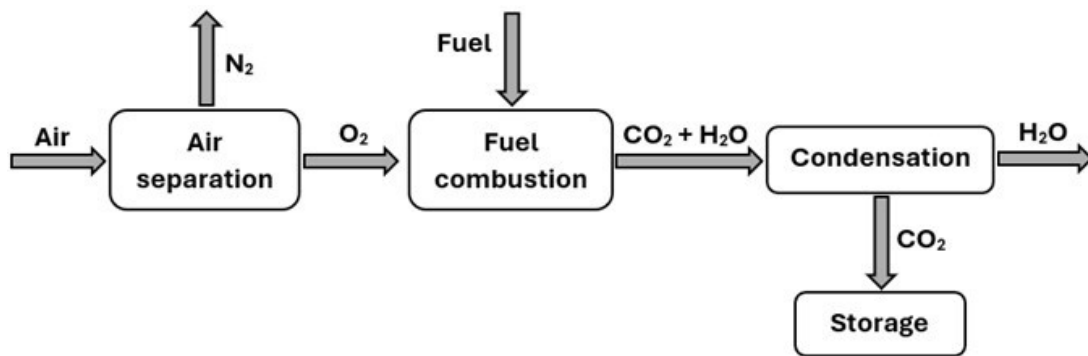


Figure 1.11: General oxy-fuel combustion CO₂ capture block flow diagram.

After combustion, the flue gas is cooled, allowing water vapor to condense, leaving a concentrated stream of CO₂ that can be easily separated and stored. The high CO₂ concentration in oxy-fuel combustion significantly reduces the energy and cost required for CO₂ capture compared to conventional methods. This technology is particularly well-suited for industrial applications where high-purity CO₂ is required, such as in metallurgical industries and coal-fired power plants (Zhang et al., 2018). In these settings, oxy-fuel combustion is used to enhance thermal efficiency while enabling efficient CO₂ capture. However, the broader adoption of oxy-fuel combustion capture in other industries has been limited. This reluctance is primarily due to the high energy costs associated with oxygen production. Despite these challenges, ongoing research aims to optimize oxy-fuel combustion by developing more efficient air separation methods, such as membrane-based oxygen separation and sorbent-enhanced oxygen

production. These advancements could make oxy-fuel combustion a more viable option for a broader range of applications in the future.

The most suitable approach to use for a CO₂ capture depends on critical factors as the operating conditions of the process and constraints given by the objectives to reach. If the goal is to capture CO₂ from sources where it is present in low concentrations and at low pressures, the technology employed will differ significantly from that used in high-pressure, high-CO₂-concentration streams, such as syngas from gasification or hydrogen production. Furthermore, the intended use of the captured CO₂ plays a decisive role in technology selection. For applications requiring high-purity CO₂ such as the food and beverage industry, highly selective capture methods are necessary. In contrast, for geological storage, where ultra-high purity is not required, less selective but more cost-effective methods may be sufficient. Depending on the specific requirements, various CO₂ capture technologies are available, including absorption, adsorption, membrane capture, cryogenic separation, capture via microalgae and chemical looping. These alternatives provide a wide range of options for tailoring the capture process to the specific characteristics of the gas stream and the desired final product. For the aim of this thesis is then fundamental to understand which CO₂ capture technique is suitable for the decentralized case. Table 1.3 presents a comparative overview of the main CO₂ separation methods highlighting their applicability in decentralized systems. Each technology is evaluated with respect to CO₂ purity, capture capacity, energy demand, and scalability, providing a clear framework to identify which solutions are most appropriate for small- to medium-scale, modular installations.

Table 1.3: *Features of main CO₂ capture technologies.*

Technology	Decentralized applicability	Purity (%)	CO₂ capture capacity	Energy demand
Amine absorption	Not ideal	95–99%	High	High
Selexol/Rectisol	No	95–99%	High	Medium-High
PSA	Yes	85–99%	Moderate	Medium
Membranes	Yes	Up to 99% (multi-stage)	Scalable	Low-medium
Cryogenic	No	> 99%	High	Very high
Microalgae	Yes	Variable	Low	Low
Chemical looping	No	> 90%	High	High

Adsorption and membrane separation processes will be analysed in detail respectively on chapter 2 and 3 since they concern the techniques selected for this thesis work. On the next paragraph, absorption techniques are briefly explained.

1.5.2 Absorption techniques

In absorption techniques, CO₂ is selectively removed from a gas mixture using a liquid solvent, known as the absorbent. The process typically occurs in a gas-liquid contactor, such as an absorber column, where the gas stream is brought into direct contact with the absorbent. As the CO₂-rich gas flows upward through the column, it interacts with the descending liquid absorbent. During this interaction, CO₂ molecules are absorbed into the liquid phase due to the solvent's chemical or physical affinity for CO₂, while the remaining gases, which are less soluble, continue to exit the column. After the absorption process, the CO₂-rich solvent is directed to a regeneration unit, such as a stripper column, where it is heated to release the absorbed CO₂. The regenerated solvent is then recycled back to the absorber column for continuous operation. The captured CO₂ can be compressed and stored or utilized for various applications, such as enhanced oil recovery or the production of valuable chemicals. The absorption process offers significant potential for CO₂ capture, characterized by its high selectivity for CO₂ and substantial absorption capacity, making it a widely adopted method in advanced carbon capture applications. Nevertheless, its broader implementation in various industries, including power generation, is hindered by several challenges. These include high energy consumption, particularly during solvent regeneration, susceptibility to corrosion, potential toxicity, elevated costs associated with high-performance solvents, and significant mass loss of the absorbent due to limited chemical stability. Such limitations pose considerable obstacles to the widespread adoption of absorption-based CO₂ capture technologies.

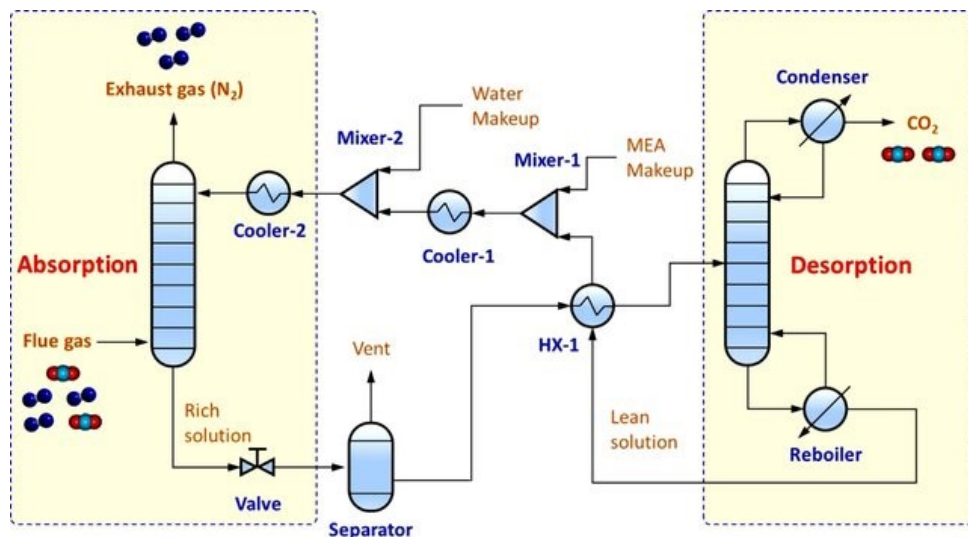


Figure 1.12: Absorption CO₂ capture from a flue-gas stream (Khan et al., 2023)

A notable example of large-scale CO₂ capture via chemical absorption is the Petra Nova project in Texas, USA. Operated at a coal-fired power plant, the system was designed to treat flue gas containing approximately 13% CO₂, capturing around 1.4 million tons of CO₂ per year. The technology employed is Fluor's Econamine FG Plus™ process, a well-established MEA-based

system optimized for post-combustion conditions. The energy consumption profile of the process includes a thermal demand of approximately 3.0 GJ per ton of CO₂ for solvent regeneration and an electrical consumption of 0.4–0.5 GJ per ton, mainly due to CO₂ compression and solvent circulation (Cichanowicz, 2022).

Absorption processes can be categorized into two main types:

- **Chemical Absorption:** This method is the most widely used among absorption techniques and relies on a chemical reaction between the CO₂ and the solvent producing an intermediate molecule. Common chemical solvents include amine-based solutions, such as monoethanolamine (MEA), diethanolamine (DEA) with piperazine as activator. These solvents react with CO₂ to form a stable compound, which can be regenerated by heating, releasing pure CO₂ for capture and reuse. Chemical absorption is extensively employed for separating different gases, and this technology is principally applied for carbon capture at relatively lower values of partial pressure.
- **Physical Absorption:** This uses solvents that physically dissolve CO₂ without a chemical reaction. The solvent at low temperatures and high partial pressure specifically binds to CO₂ thereby obeying Henry's law, which links the solubility of gases to their partial pressure. For high-pressure streams, physical absorption is efficient for capturing CO₂; for instance, CO₂ capture in a pre-combustion stage of the integrated coal gasification combined cycle (IGCC) plants. Here the molecules of CO₂ dissolved into the bulk of the material in absorption. It's important to distinguish this process by the adsorption since in that case the gas is dissolved into the bulk of the solvent.

Absorption is widely regarded as the most versatile and adaptable method for CO₂ capture, applicable across various contexts, including pre-combustion, post-combustion, and oxy-fuel capture systems. Among these, the choice of solvent is paramount, as it directly influences the selectivity, environmental impact, and overall performance of the process. An ideal solvent should exhibit high CO₂ selectivity, low toxicity, and strong chemical stability. One of the most significant barriers to absorption efficiency is the substantial energy consumption associated with solvent regeneration. In chemical absorption, over 60% of the total energy consumed is typically dedicated to solvent regeneration within the stripper unit. Furthermore, the economic viability of absorption-based CO₂ capture remains a subject of ongoing research. To enhance the efficiency and sustainability of the absorption process, future research should prioritize the development of advanced solvents with superior thermal stability and CO₂ absorption capacity. Addressing these challenges is essential for making absorption-based CO₂ capture a viable solution for large-scale industrial applications (Khan et al., 2023).

1.5.3 CO₂ transport and storage

Following the capture, CO₂ can be utilized (CCU) in various application. Utilization pathways include its conversion into value-added products such as urea, methanol, and synthetic fuels, or its incorporation into construction materials through mineralization processes. CO₂ can also serve niche roles in industries such as food and beverage or enhanced oil recovery (EOR). These applications require varying levels of CO₂ purity—ranging from over 99% for chemical synthesis and food use, to 80–95% for mineralization. As an alternative to the usage, the captured CO₂ is transported and then stored to secure storage site (CCS). Among the various transportation methods, pipelines are the most used, particularly for large-scale CO₂ transfer. Pipelines offer an efficient and continuous means of transporting CO₂, and extensive networks already exist globally for various gases, including CO₂. For example, the United States has approximately 800,000 km of hazardous liquid and natural gas pipelines, along with 3.5 million km of natural gas distribution lines, of which around 6,500 km are specifically dedicated to CO₂ transport. While truck and rail transport are also viable options, they are generally limited to small-scale CO₂ movement, such as pilot projects where CO₂ is transported from capture sites to nearby storage facilities. However, these methods are unlikely to be significant for large-scale CCS deployment due to their limited capacity and higher costs. Another practical option, particularly for regions with extensive coastlines, is CO₂ transport via ship. This method is already used in Europe, where ships transport food-grade CO₂ (approximately 1,000 tonnes) from major point sources to coastal distribution terminals. Shipping provides flexibility for regions without direct access to pipeline networks. Looking ahead, the global CO₂ transportation infrastructure will need to expand significantly to accommodate large-scale CCS deployment. According to estimates consistent with the International Energy Agency’s (IEA) least-cost pathway for halving energy-related CO₂ emissions by 2050, the required CO₂ transport capacity is projected to be approximately 100 times greater than current levels. This expansion will necessitate substantial investment in pipeline networks, particularly in regions with high CO₂ emissions and suitable storage sites. The storage of CO₂ can be achieved through various method which the most common is the geological storage. It leverages the natural capacity of the Earth's subsurface to store large volumes of CO₂ safely and effectively by isolate it for an extended period to prevent its release into the atmosphere. This storage can be achieved through various techniques, which can be classified into onshore, offshore, and oceanic storage as reported in fig 1.14 (Bashir et al., 2023). In a typical CO₂ geo-storage process, carbon dioxide emissions from fixed sources, such as power plants, are captured, compressed, and converted into a liquid or supercritical form before being injected into deep geological formations, including saline aquifers, depleted oil or gas fields, or unmineable coal beds. For geological storage, the purity of captured CO₂ typically needs to be 95% or higher, although small amounts of impurities can be tolerated depending on the specific storage site. Water vapor must be

removed to prevent corrosion and hydrate formation in pipelines and reservoirs. Other contaminants like oxygen, nitrogen, sulphur compounds, or hydrogen sulphide are limited because they can affect the chemical stability of the reservoir, increase corrosion risk, or reduce the density and injectivity of the CO₂ stream (IEAGHG, 2010). This method is widely considered the most viable approach for long-term CO₂ sequestration, as it prevents the release of captured CO₂ into the atmosphere. However, it is not without risks. Injecting large volumes of high-pressure liquid CO₂ underground can disturb the mechanical stability of the reservoir, potentially causing induced seismicity, caprock failure, or unintended CO₂ leakage. Careful site selection, geological assessment, and continuous monitoring are therefore essential to ensure long-term storage integrity. CO₂ can also be sequestered through ocean storage, where CO₂ is injected directly into the deep ocean, either as a liquid that dissolves or forms hydrate structures. Given the immense volume and depth of the ocean, this method theoretically offers substantial storage capacity.

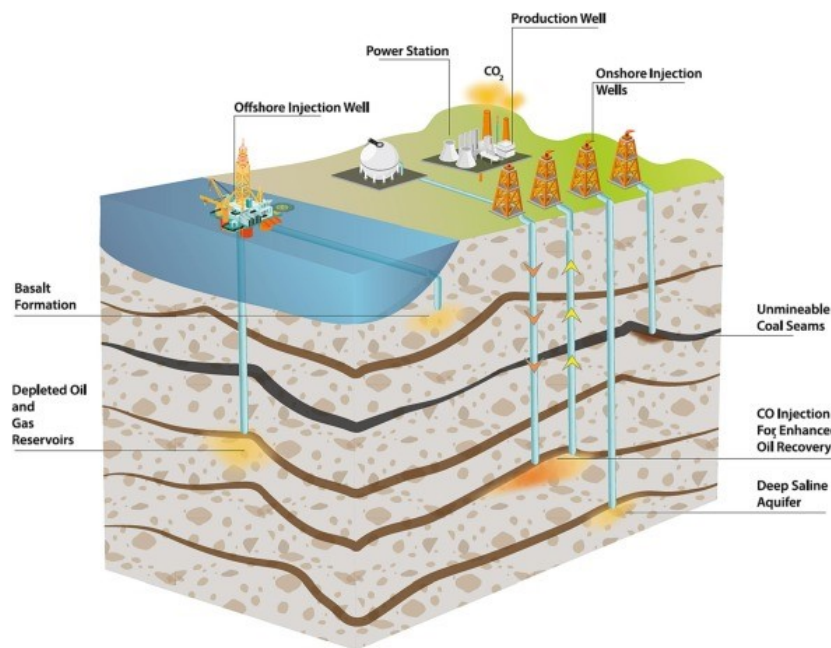


Figure 1.13: CO₂ geo-storage options (Bashir et al., 2023).

It is based on the natural carbon cycle, where oceans serve as a significant carbon sink. However, ocean storage is not without ecological risks. Injecting CO₂ into the ocean can cause localized seawater acidification, primarily due to the formation of carbonic acid when CO₂ reacts with water, which can harm marine ecosystems. Moreover, the process may also result in decreased oxygen levels at the injection site, posing additional threats to marine life. While both geological and ocean storage offer substantial potential for CO₂ sequestration, they each present unique technical, environmental, and economic challenges that must be carefully evaluated (Bashir et al., 2023).

1.6 SYPOX e-SMR biogas-to-hydrogen process

The SYPOX process is a decentralized system for producing renewable hydrogen via electrified steam methane reforming (e-SMR) of biogas. Approximately 1 Nm³ of hydrogen is produced from 0.6 Nm³ of biogas composed of a 50:50 methane and carbon dioxide mixture (Maporti et al., 2022).

1.6.1 Process description

A basic process scheme is reported in Figure 1.15. The core process steps are realized in a shipping container in which the core pieces of equipment are installed.

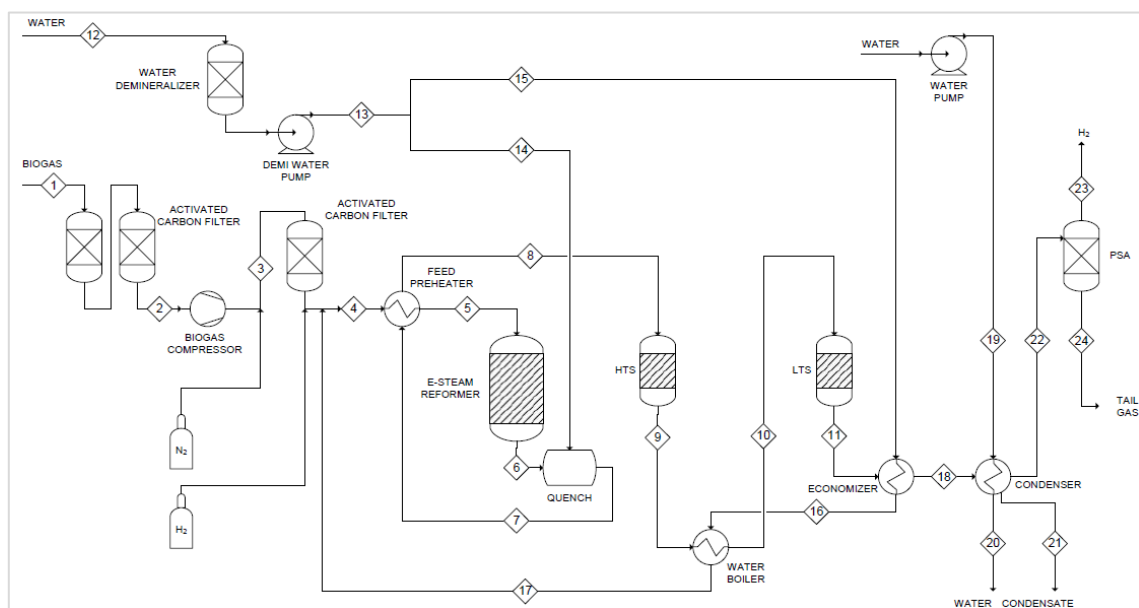


Figure 1.15: PFD of the SYPOX biogas-to-hydrogen plant used as the case study.

Like traditional hydrogen plants, this biogas-to-hydrogen configuration comprises three main sections: reforming, water-gas shift (WGS), and separation section. Biogas from the fermenter (Stream 1) is first treated with activated carbon filters to reduce contaminants (H₂S, siloxanes, VOCs) to <30 ppb. These filters are not shown in the process scheme. The purified biogas (Stream 2) is then compressed to 10 bar (Stream 3) and enters the container. A guard bed filter offers additional protection against trace contaminants. Nitrogen and hydrogen bottles are connected before and after this filter for maintenance and start-up/shutdown operations (N₂ as purge gas, H₂ as a reducing agent). Tap water (Stream 12) is supplied to a demineralization unit, then pressurized to 10 bar (Stream 13) via a pump and split into Streams 14 and 15, used for quenching and steam generation, respectively. Stream 15 is heated to 175°C in an economizer (shell-and-tube heat exchanger) using hot gases (Stream 11) from the Low Temperature Shift (LTS) reactor. The heated water (Stream 16) is sent to a steam generator, producing saturated steam at 180°C (Stream 17). This steam is mixed with the biogas (Stream 3) to form Stream 4, then preheated to 430°C (Stream 5) in the feed preheater before entering

the e-SMR. The e-SMR is a structured catalytic reactor with a Ni-based catalyst coated on the inner walls of ceramic channels (diameter of a few mm). The main reactions include steam reforming, water-gas shift, and dry reforming. Being the overall endothermic process heat must be supplied. That is done via Joule heating, as electric current flows through electrified metallic wires in direct contact with the gases. The reactor outlet (Stream 6) contains a gas mixture of H₂, CO, CO₂, CH₄, and H₂O. The reactor is flanged to a quenchvessel, where hot gases at 950°C (Stream 6) are cooled to 570°C (Stream 7) using water from Stream 14. Stream 7 also serves as the hot fluid in the feed preheater. The cooled gas coming out from the preheater (Stream 8) has a temperature of about 350°C. It is sent to the High Temperature Shift (HTS) reactor, an adiabatic fixed-bed reactor loaded with pelletized Cr-based catalyst. Its primary function is to convert CO via the water-gas shift reaction, increasing H₂ yield. The exothermic reaction raises the outlet temperature to 487°C. This gas (Stream 9) is used as a hot utility in the water boiler where is cooled to 195°C (Stream 10) before entering the Low Temperature Shift (LTS) reactor. It is also an adiabatic fixed-bed reactor with Cu-Zn-Al catalyst, performing the same reaction, further reducing CO concentration. The outlet gas (Stream 11) exits at 260°C and is cooled to 160°C (Stream 18) in the economizer. After the shift reactors, CO content is reduced to approximately 1 mol%. The syngas (Stream 18) is then cooled to 35°C in a condenser/phase separator, where water is removed (Stream 21). Cooling water (Stream 19) is provided by an external pump. The gas, after condensate removal, enters the PSA unit for purification. The PSA achieves a hydrogen recovery of ~78% and a purity of 99.9%. A portion of hydrogen remains in the PSA off-gas (Stream 22), which also contains CO, CO₂, CH₄, and N₂. This stream in the actual PFD is send to a flare losing the energy content present inside.

1.6.2 CO₂ capture unit location

The aim of the thesis is to add to the plant described in the previous section a of CO₂ capture unit and verify the way it impacts in the hydrogen production chain of SYPOX. As the steam reforming is applied to a renewable resource as biogas the hydrogen produced has already a lower carbon footprint than the conventional grey hydrogen. If a carbon capture and storage system were integrated into the SYPOX process, it could potentially result in a net removal of CO₂ from the atmosphere, thereby enabling the production of carbon-negative hydrogen. The feasibility of CO₂ capture implementation is applied also looking at the change in the levelized cost of hydrogen (LCOH) with and without the CCS. When considering the integration of Carbon Capture and Storage (CCS) into the SYPOX e-SMR plant, it is essential to identify an optimal location within the process for CO₂ removal. Since the produced hydrogen is not subjected to combustion, the capture must necessarily follow a pre-combustion strategy. As illustrated in Figure 1.9, this implies targeting a syngas stream with a high CO₂ concentration. Two potential capture points can be identified in the process flow diagram (PFD): Stream 22,

which precedes the PSA unit and contains a CO₂-rich syngas mixture, or Stream 24, corresponding to the PSA tail gas. Table 1.3 reports the features of stream 22, 23 and 24.

Table 1.4: *Stream features of the PSA inlet and outlet*

Stream	22	23	24
Description	PSA inlet	Pure H₂	Tail gas
Temperature [°C]	35	35	35
Pressure [bar]	10	10	1.03
Molar flow [kmol/h]	8.40	4.52	3.88
Mass flow [kg/h]	134.80	9.10	125.70
Composition [-]			
CO₂	0.32	0.00	0.70
CO	0.01	0.00	0.03
H₂	0.66	1.00	0.26
H₂O	0.01	0.00	0.01
Partial pressure [bar]			
CO₂	3.2	0.00	0.72
CO	0.1	0.00	0.03
H₂	6.6	10.00	0.27
H₂O	0.1	0.00	0.01

Both locations offer viable conditions for CO₂ separation, though the choice depends on the desired capture efficiency, integration complexity, and downstream utilization or storage strategy. The technologies that must be considered for the techno economic analysis are PSA and membranes. Both technologies let occur their separation thanks to a partial pressure gradient, then the pressure of the analysed stream becomes a fundamental factor in the choice of the location. For PSA it is well known that CO₂ exhibits strong interactions with certain adsorbents, such as zeolites, even at low pressures. As will be explained in chapter 2, beyond a certain threshold, increasing the pressure does not significantly enhance the amount of CO₂ adsorbed, as the adsorbent approaches saturation. Given this behavior, the most suitable option for CO₂ capture in the SYPOX process is to target the tail gas stream exiting the PSA unit at atmospheric pressure. This approach dictates the use of a vacuum swing adsorption (VSA) cycle to ensure effective regeneration of the adsorbent. On the other hand, the application of membrane gas separation is favoured when there is a significant pressure difference between the feed and permeate sides, as this increases the driving force and enhances the permeation of CO₂ through the membrane. In particular the membrane area necessary for the separation is reduced. Therefore, the optimal configuration would involve placing a membrane module upstream of the PSA unit in the SYPOX process. The permeate will be then a stream full of CO₂ at atmospheric pressure while the retentate, still at high pressure, is a mixture composed of hydrogen and carbon dioxide that is going to be the inlet for the PSA unit. This setup takes

advantage of the elevated pressure of the syngas exiting the Low Temperature Shift (LTS) reactor, thereby maximizing CO₂ separation efficiency prior to hydrogen purification.

1.6.3 Hydrogen Production Cost and Carbon footprint.

The economic analysis will be performed on the two technologies, PSA and membranes calculating the capital and operating requirements to add this processes to the SYPOX plant. The cost calculation will be further used to retrieve two fundamental parameters necessary to assess the efficiency of the application of a CO₂ capture technique. The first parameter considered is the hydrogen production cost (HPC), calculated as the total annualised cost (TAC) of the plant comprising CAPEX and OPEX over the kilograms of hydrogen produced per hour in the plant. The table below represents the data used to retrieve the HPC.

Table 1.5: *Data used for calculating the hydrogen production cost.*

<i>Parameter</i>	<i>Value</i>
Hydrogen recovery [%]	82
Hydrogen productivity [kg/h]	9.1
Skid lifetime [years]	10
Annualized CAPEX [k€]	246
CAPEX impact on TAC [%]	52
OPEX impact on TAC [%]	48
HPC [€/kgH₂]	7.05

The second factor analysed is the carbon footprint of the plant, which—following the implementation of CO₂ capture—becomes the primary target for reduction. The carbon footprint is evaluated in terms of kilograms of CO₂ emitted per kilogram of H₂ produced. CO₂ emissions are further categorized into direct and indirect sources. Direct emissions refer to the carbon dioxide generated during the chemical reactions of the process, while indirect emissions are associated with the electricity consumption required to operate the e-SMR process and its supporting equipment.

Table 1.6: *Data used for calculating the hydrogen carbon footprint.*

<i>Parameter</i>	<i>Value</i>
Plants electricity consumption [kW]	180
Direct CO ₂ emissions [kg/h]	62.5
Hydrogen productivity [kg/h]	9.1
Average carbon intensity electricity [kg CO _{2eq} /kWh]	
	French 30
	Germany 300
	Italy 265

Three countries—French, Germany and Italy—in which to locate the plant have been identified, each with a different carbon intensity, defined as the amount of carbon dioxide (CO₂) emissions produced per kWh of electricity used. It is a key indicator of how “clean” or “polluting” a country's energy and economic systems are.

Table 1.7: *Hydrogen carbon footprint from electrified biogas reforming without carbon capture for different plant location (electricity mix).*

Plant location	Direct process emission [kg CO₂/kg H₂]	Indirect emission from electricity [kg CO₂ /kg H₂]	Total emissions [kg CO₂ kg⁻¹ H₂]	Reduction vs centralized SMR [%]
Italy	6.88	5.51	12.39	+37.6
Germany	6.88	6.24	13.12	+45.7
France	6.88	0.62	7.5	-16.6

Table 1.7 highlights how the environmental impact of decentralized hydrogen production varies significantly depending on the country. A section in which is compared the reduction of the total emissions using a decentralized plant with respect to the centralized case is then added. The process taken as a reference is the SMR fired based on terrace wall reformer by Foster Wheeler (IEAGHG, 2017). In Italy and Germany, producing hydrogen without any carbon capture leads to higher total emissions than centralized SMR, primarily due to the high indirect emissions associated with their electricity mixes. In contrast, France, with its low-carbon electricity mix, achieves lower emissions even without capture, making decentralized production more sustainable. This data will be used as a reference point to assess the change in the carbon footprint after the CO₂ capture with the two different technologies is applied.

Chapter 2

Pressure swing adsorption (PSA)

The first technology that has been analysed in this thesis to make a study over a CO₂ capture in a decentralized plant is the pressure swing adsorption (PSA). PSA has become a prominent sorbent-based technology used for several applications concerning air drying, air separation, hydrogen recovery and separation of hydrocarbons. This chapter presents the general characteristics of pressure swing adsorption (PSA) processes, followed by a detailed discussion of the fundamentals of adsorption and an overview of the most employed PSA cycle configurations. In addition, a mathematical description of the PSA process is provided, including the theoretical framework and assumptions typically used to model it. These elements form the basis for understanding the design and sizing procedures applied in chapter 4 as part of this thesis work.

2.1 General features of PSA

The first patent on PSA was issued in 1933 to the Finlayson and Sharp, indicating that this technique has been in use for nearly a century. Since then, numerous innovations have been applied to this technology, enabling it to achieve high levels of productivity and efficiency in CO₂ capture, both from a technical and economic perspective, comparable to other technologies such as chemical absorption. Fig. 2.1 indicates a historical milestone diagram of PSA technology evolution and upgradation (Shah, 2021). A fundamental aspect of adsorption-based separation technologies lies in the selection of an appropriate adsorbent material, a principle common to all adsorption processes. For any given feed mixture, the chosen adsorbent must preferentially adsorb one specific component over the others. The selectivity of the adsorption process may arise from thermodynamic factors, which govern the equilibrium distribution of species between the gas and solid phases, or from kinetic factors, which relate to differences in the rates of adsorption among the components. Although both factors influence the overall performance of the process, a distinction is typically made between equilibrium-selective and kinetically selective adsorbents. This distinction is based on identifying which step, equilibrium sorption or mass transfer kinetics, constitutes the rate-limiting factor in the process. Adsorption processes typically involve two main stages. The first is the adsorption step, in which the target species—being more favourably adsorbed—is selectively removed from the gas mixture as it passes over the adsorbent surface.

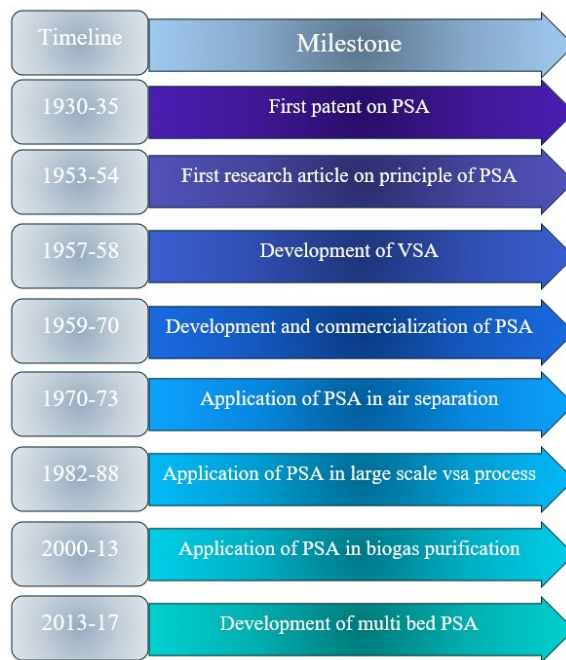


Figure 2.1: Chronological order for the historical developments of the PSA process.

This step results in a separation, producing a raffinate stream that is depleted of the adsorbed component. Adsorption continues until the active sites of the adsorbent are fully occupied and the material reaches saturation. At this point, the desorption step begins, during which the adsorbed species is released from the surface of the adsorbent, often by changing pressure, temperature, or introducing a purge gas. The desorbed gas forms a new stream enriched in the previously adsorbed species, commonly referred to as the extract. This stage also regenerates the adsorbent, allowing the cycle to restart. In (fig 2.2) the two macro-steps are depicted with the regeneration step done with a displacement inert compound called purge. In most practical applications, these steps are carried out in fixed-bed adsorption columns packed with adsorbent material. The feed gas typically enters from the bottom and flows upward through the bed. A critical role in determining the process performances is then given by the flow dynamics in the packed bed. A good design of the column becomes of primary importance to ensure a good process development (Ruthven, 1984).

The defining feature of pressure swing adsorption processes is that the regeneration of the adsorbent is achieved by reducing the total pressure in the column, rather than altering the temperature or introducing an inert purge gas. By depressurizing the column, the adsorbed species are desorbed due to a decrease in their partial pressure, which in turn weakens the molecular interactions between the gas molecules and the adsorbent surface. Although adsorption is an exothermic process, PSA operations are often approximated as isothermal due to the good thermal conductivity of most adsorbent materials, the high surface area of the packed bed, and the fast cycle times, which limit temperature gradients. Additionally,

appropriate system design—such as controlled flow rates, and efficient heat dissipation—helps maintain near-uniform temperature throughout the process.

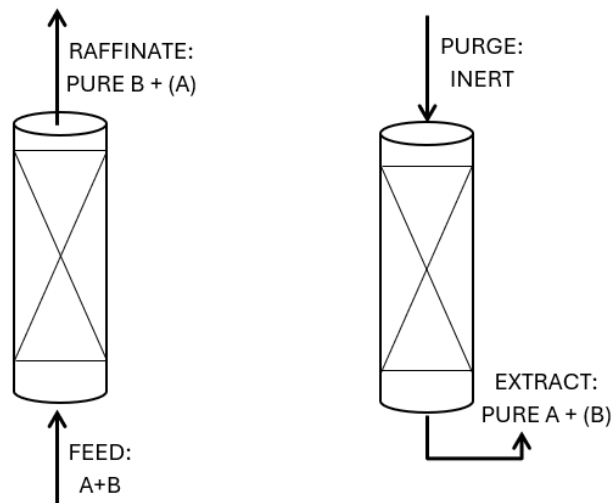


Figure 2.2: *The two macro-steps of an adsorption process in a vacuum column: adsorption step (on the left) and regeneration step with displacement inert purge (on the right).*

The useful adsorption capacity is defined as the difference between the amount of gas adsorbed during the high-pressure adsorption step and the amount remaining on the adsorbent after depressurization. This can be visualized as the difference in loading along the same adsorption isotherm (see Fig. 2.3). One of the principal advantages of PSA is the ability to rapidly alternate pressure within the packed bed, enabling short cycle times. This results in increased throughput per unit of adsorbent volume, enhancing the overall efficiency and productivity of the process with respect to process which regeneration consists in raising temperature or purging with a displacement gas (although during desorption is often adopted a purge step to better purify the adsorbent). A key disadvantage of pressure swing adsorption lies in the difficulty of regenerating adsorbents that strongly retain a particular component. In such cases, achieving desorption requires the application of a deep vacuum, which significantly increases operational costs and energy consumption. Compared to other separation unit operations PSA differs fundamentally in that it operates in a cyclic and inherently transient mode due to continuous pressure variations throughout the cycle.

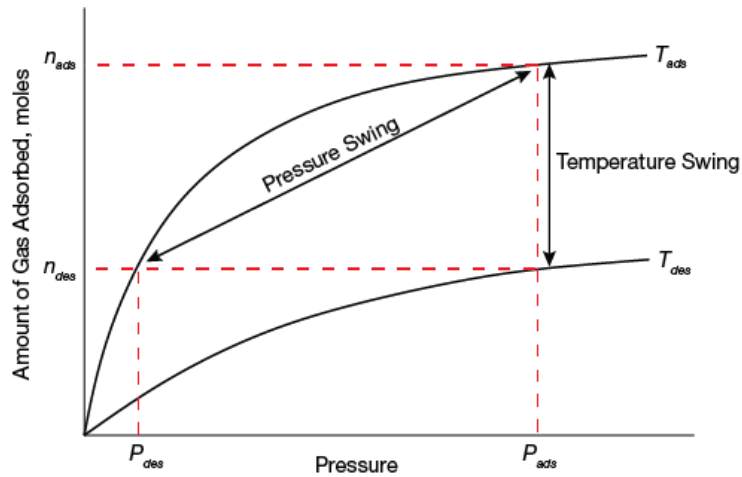


Figure 2.3: Schematic isotherms showing how in pressure and temperature swing equilibrium loading is changed.

While traditional separation processes—such as absorption, distillation, solvent extraction, or stripping—typically reach steady-state conditions and can be described using relatively simple ordinary differential equations (ODEs), PSA processes demand a more complex modelling approach. Because the gas-phase behaviour along the packed bed varies both spatially and temporally, PSA systems are governed by partial differential equations (PDEs). This cyclic and non-steady-state behaviour is a defining feature of PSA and presents unique challenges for both modelling and process optimization. Design and scale-up procedures for PSA units are largely available in the open literature. However, they have not yet been fully integrated into standard chemical engineering curricula, and as a result, an element of uncertainty or complexity still surrounds their practical application. (Ruthven, 1994)

There are five general features of to look at to determine the validity and efficiency of a PSA process and are mostly taken as elements of comparison with other separation technologies.

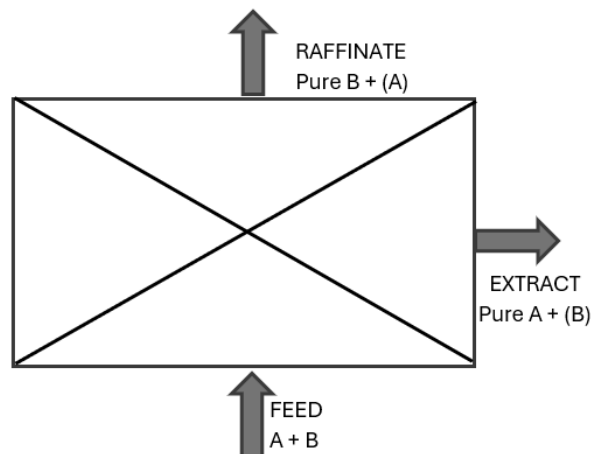


Figure 2.4: Overall material balance of a PSA unit

1. **Product purity:** In a typical PSA process, the raffinate product—corresponding to the less strongly adsorbed or more slowly diffusing species—can be recovered in a highly pure form. In contrast, the extract product, which includes the more strongly adsorbed or faster-diffusing species, is generally released in a less pure form and is often treated as a byproduct, especially in cases in which the product constraints are required high purity levels of the weak adsorbed species. PSA technology is most effective and economically viable in applications where a high purity raffinate is the desired product. Looking at figure 2.4 the product purity corresponds to the molar fraction of the most present component in the raffinate stream (B).

2. **Recovery:** Considering figure 2.4, the fractional recovery of component B in the raffinate product is defined as:

$$Recovery = \frac{\text{Amount of B in the Raffinate}}{\text{Amount of B in the Feed}} \quad (2.1)$$

In a PSA process it is generally lower compared to traditional separation methods such as distillation, absorption, or extraction. While recovery can be improved by incorporating additional steps into the cycle or by increasing the number of adsorption beds, these modifications result in higher capital costs. Therefore, PSA is most suitable for applications in which the feedstock is relatively inexpensive, and achieving high product yield is not the primary economic constraint.

3. **Energy requirements:** The system efficiency—defined as the ratio of separation work to total energy consumed— of a PSA is comparable to that of processes such as distillation or extraction (Ruthven, 1994). However PSA systems rely on mechanical energy, which is generally more expensive than thermal energy. As a result, power consumption represents the major component of operating costs in that type of operations. PSA systems are especially advantageous when the feed stream is naturally or easily available at high pressure. In such cases, capital and energy costs for compression are significantly reduced, and it is generally more economical to recompress the purified product than to compress the feed to the system's operating pressure.

4. **Pressure ratio:** The performance of any PSA process is fundamentally governed by the ratio of absolute pressures. The shape of the adsorption equilibrium isotherms presents the difference between the loading at operating high and low pressures of the process. Overall performances can be enhanced carrying out desorption step in sub atmospheric conditions (VSA).

- 5. Scaling characteristics:** The operating costs of most separation processes tend to increase approximately linearly with throughput. In the case of PSA systems, the capital cost also scales linearly with capacity, which contrasts with many other separation technologies—such as cryogenic distillation—where capital costs exhibit a nonlinear relationship with throughput. In such systems, the incremental cost per unit of capacity decreases as the scale of operation increases, offering greater economies of scale. As a result, when both capital and operating costs are considered, PSA tends to be more economically favourable at low to moderate throughput levels, while other technologies, such as cryogenic separation, may become more cost-effective for large-scale operations.

2.2 Fundamentals of adsorption

Understanding the design and operation of a PSA process requires at least a foundational knowledge of adsorption principles and the dynamic behaviour of adsorption columns. The overall performance of a PSA process is influenced by both equilibrium and kinetic factors, although the relative importance of these factors varies significantly depending on the specific system. In most PSA applications, the process is considered equilibrium-driven, meaning that selectivity arises primarily from differences in equilibrium affinities between the adsorbent and the various components of the gas mixture. In such systems, mass transfer resistance generally has a detrimental effect, reducing performance relative to an ideal system where equilibrium is assumed to be instantaneous. However, there are also PSA processes in which selectivity is entirely kinetic—that is, the separation is governed by differences in adsorption rates rather than equilibrium capacities. In these cases, mass transfer resistance becomes a critical factor, and the system's behaviour cannot be accurately predicted without a detailed understanding of the kinetic mechanisms involved.

2.2.1 Adsorption mechanism

Understanding the fundamentals of adsorption begins with distinguishing it from absorption, as the two processes are often confused despite being fundamentally different. Absorption involves the uptake of a substance (the absorbate) into the bulk or volume of another material (absorbent). It describes the ability of a material to incorporate impurities into its internal structure, allowing for the separation of components from a gas or liquid stream through dissolution or diffusion into the absorbent. In contrast, adsorption is a surface phenomenon in which fluid-phase molecules adhere to the surface of a solid material (adsorbent). Rather than entering the interior of the material, the molecules are retained on the external or internal surface of the solid. This surface adherence enables the selective separation of specific components

from a gas or liquid mixture based on their affinity for the adsorbent surface (Pourhakkak et al., 2021).

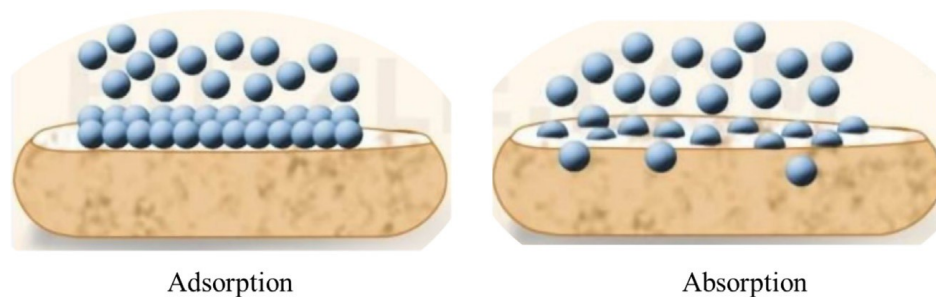


Figure 2.5: Schematic representation of adsorption and absorption processes (Pourhakkak et al., 2021).

During the adsorption mechanism a gas molecule approaching a solid surface experiences a reduction in potential energy due to interactions with the atoms or molecules of the solid. As a result of these attractive forces, gas molecules tend to accumulate near the surface, leading to a local increase in molecular density compared to the surrounding free-gas phase. This concentration effect is the fundamental driving force behind surface adsorption. Another important distinction within the adsorption phenomenon arises from the strength of the surface interactions between the adsorbate and the adsorbent. When these forces are relatively weak, typically involving van der Waals interactions—and, in the case of polar or quadrupolar molecules, supplemented by electrostatic forces such as dipole-dipole or quadrupole interactions—the process is referred to as physical adsorption or physisorption. This form of adsorption is generally reversible and characterized by low enthalpy changes. In contrast, when the interaction forces are strong and involve a significant degree of electron transfer or chemical bonding between the adsorbate and the surface atoms of the adsorbent, the process is known as chemical adsorption or chemisorption. Chemisorption requires an activation energy to initiate the bond formation between the gas and the solid surface, making it more prominent at higher temperatures. The process is often irreversible, or at least difficult to reverse without substantial energy input because of the strong chemical bond created during the adsorption process. Because of the slower kinetics and irreversibility, chemisorption is generally unsuitable for PSA processes, which require rapid and reversible adsorption–desorption cycles driven by pressure changes (Ruthven, 1994). Thus, the phenomenon at which pressure swing adsorption refers is the physisorption. Since adsorption forces depend on both the nature of the adsorbing molecule and the nature of the surface, different substances are adsorbed with different affinities. This selectivity is the foundation of adsorption-based separation processes. The role of the adsorbent is to provide the surface area necessary for the selective adsorption of the preferentially adsorbed species. A high selectivity is the primary requirement, but a high capacity is also desirable, as capacity determines the size and thus the cost of the adsorbent beds and finally the capital cost (CAPEX) of the application.

A key classification which is going to impact on the equilibrium of adsorption concerns the nature of the surface of the adsorbent material which can be hydrophilic and hydrophobic. Polar surfaces, often resulting from the presence of ions in the adsorbent structure, preferentially attract polar molecules. This enhanced selectivity arises from additional interactions, such as field-dipole and field-quadrupole forces, which contribute to the overall adsorption energy. In contrast, on a nonpolar surface, both polar and nonpolar molecules tend to adsorb to a similar extent. In such cases, the selectivity is reduced, and adsorption is governed more by dispersion forces, as van der Waals interactions than by specific bounds. When the adsorbent surface contains hydroxyl groups, strong interactions with molecules like water can occur via hydrogen bonding. Here, selectivity is primarily attributed to H-bond formation rather than general surface polarity. However, in such hydrophilic systems, polar molecules without active hydrogen atoms may exhibit adsorption affinities like those of nonpolar species, since they cannot engage in hydrogen bonding. On the other hand, when hydrophilic selectivity arises specifically from hydrogen bonding, only polar molecules possessing active hydrogen atoms (i.e., those capable of forming hydrogen bonds) will be strongly retained. Polar molecules lacking active hydrogens, therefore, may exhibit adsorption affinities like those of nonpolar sorbates, despite their polarity. It is important to note that hydrophobic surfaces do not entirely repel water. In practice, water will be adsorbed to some extent on nearly any surface, at least to the degree dictated by van der Waals interactions. The key distinction is that on hydrophilic surfaces, water—and other polar molecules—exhibits much stronger adsorption than would be expected from van der Waals forces alone, due to additional specific interactions, such as electrostatic attraction or hydrogen bonding.

The surface structure of an adsorbent material is usually, full of pores of either spherical shape or irregular shape. As a result, the rate of adsorption or desorption is generally governed by diffusion through the adsorbent's pore network. Therefore, pore structure and diffusional limitations must be carefully considered in both the selection of the adsorbent and the determination of appropriate operating conditions. Pores are classified by IUPAC into three different times by their size:

Table 2.1: Pores dimension in Armstrong, according to IUPAC classification.

	Micropores	Mesopores	Macropores
Dimension (Å)	< 20	20-500	> 500

In micropores, guest molecules remain entirely within the influence of the solid surface's force field, even at the centre of the pore. As a result, all molecules confined within a micropore are in the adsorbed phase. In contrast, in mesopores and macropores, only the molecules near the surface experience significant interaction with the solid, while those in the central region of the

pore behave more like free gas-phase molecules. Thus, these pores function as two-phase systems, consisting of an adsorbed layer at the surface and a free gas phase in the core of the pore volume. Macropores contribute minimally to the total surface area and, therefore, to the adsorptive capacity. Their primary function is to facilitate mass transport as they serve as diffusion pathways, enabling efficient access of gas molecules to the narrower mesopores and micropores, where most of the adsorption occurs. The way the pores are distributed in the adsorbent surface structure can affect the selectivity of an adsorption process. Indeed, in some processes, separation is based on differences in adsorption rates rather than differences in equilibrium affinity. This is known as kinetic selectivity, which arises from steric hindrance—the ability or inability of molecules to diffuse into the pores. As a result, kinetic selectivity requires a very narrow pore size distribution, while the chemical nature of the adsorbent material is generally of secondary importance. Practical adsorbents can be broadly categorized based on how their pore size and distribution are determined. Materials such as silica gel, activated alumina, and activated carbon exhibit micropore diameters and pore size distributions that are largely influenced by the manufacturing process.

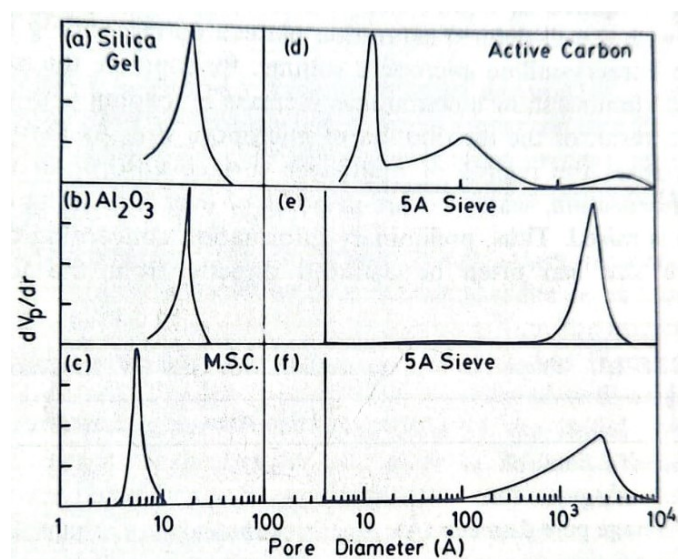


Figure 2.6: Pore size distribution for (a) silica gel; (b) porous alumina; (c) molecular sieve carbon; (d) activated carbon; (e) Davison 5A molecular sieve type 625; (f) Davison 5A molecular sieve type 525 (Ruthven, 1984)

These materials typically have a range of micropore sizes, with both the average diameter and the breadth of the distribution being tunable during production. In contrast, zeolitic adsorbents have micropore sizes precisely defined by their crystal structure. The pores in zeolites are uniform and exhibit no significant distribution in size. This molecular-level uniformity is a result of the ordered, crystalline framework of zeolites, making them particularly suitable for size-selective separations and processes that rely on kinetic selectivity.

Repeated pressurization and depressurization of an adsorbent bed, as occurs in PSA processes, can lead to particle attrition, gradually degrading the mechanical integrity of the adsorbent. Therefore, physical strength is a critical factor in the selection of an adsorbent. Even if a material exhibits favourable kinetic and equilibrium characteristics, it may be unsuitable for practical use if it lacks the mechanical robustness required to withstand the cyclic stress of industrial operation. As such, mechanical durability must be considered alongside adsorption performance in the overall evaluation of an adsorbent's suitability. Table 2.2 offers an overview of the today most practical and used commercial adsorbents.

Table 2.2: Practical adsorbent materials and their features (Ruthven, 1994).

<i>Material</i>	<i>Adsorption Control</i>	<i>Hydrophilicity</i>	<i>Physical structure</i>	<i>Example process</i>
<i>Zeolite</i>	Equilibrium-driven	Depends on the type of zeolite	Crystalline, microporous structure.	CO ₂ capture, Air separation
<i>Activated carbon</i>	Equilibrium-driven	No	Highly porous material, broad range of pore sizes	Hydrocarbon recovery, CO ₂ removal
<i>Silica gel</i>	Equilibrium-driven	Yes	Amorphous silica, high surface area, microporous structure.	Gas drying, dehydration
<i>CMS</i>	Kinetically driven	No	A form of microporous activated carbon.	Nitrogen production
<i>Activated alumina</i>	Equilibrium-driven	Yes	Highly porous, granular form.	Dehydration, CO ₂ removal

2.2.2 Adsorption equilibrium

Since the adsorption mechanism occurs near the adsorbent surface, two distinct phases can be identified: the adsorbed phase, which forms a layer of molecules bound to the surface, and the free-gas phase, consisting of unbound molecules in the surrounding gas. The adsorption–desorption process can be described as a reversible reaction (eq. 2.2) governed by thermodynamic laws, where equilibrium is reached when the rate of adsorption equals the rate of desorption (eq. 2.3). From a dynamic perspective, this equilibrium reflects the continuous exchange of molecules between the adsorbed phase and the free phase, consistent with the principles of chemical kinetics in a homogeneous system (Islam et al., 2004).



$$\text{At equilibrium:} \quad r_{ads} = r_{des} \quad (2.3)$$

$$k_a[ac][B] = k_d[acB] \quad (2.4)$$

Where ac and acB represent free active sites and occupied active sites, k_a and k_d the adsorption and desorption kinetic constants and the term inside the square bracket the equilibrium molar concentration. The efficiency of the adsorption process is typically expressed as the amount of adsorbate retained per unit mass of adsorbent, and can be quantified in terms of grams, moles, or volume per gram of adsorbent. The relationship between this amount (q) and the adsorbate concentration in the fluid phase (C) at a given temperature defines the adsorption isotherm, which describes the system's equilibrium state under constant temperature conditions.

$$q = f(C) \text{ if } T = \text{constant} \quad (2.5)$$

In gas mixtures, the ideal gas assumption is often applied, allowing the concentration of a component to be directly related to its partial pressure, thereby simplifying the analysis of adsorption equilibria. Adsorption isotherms assume the following relationship:

$$q = f(p) \text{ if } T = \text{constant} \quad (2.6)$$

In physisorption, the interaction between the adsorbate and the adsorbent surface occurs through weak physical forces—primarily van der Waals forces—rather than through the formation of chemical bonds. As a result, the adsorbate molecules retain their original identity and remain chemically unchanged. There is no breaking or formation of chemical bonds, and thus no alteration in the electronic configuration, molecular structure, or chemical state of the adsorbate (Ruthven, 1984). As a result, on a uniform surface and at sufficiently low concentrations, where adsorbed molecules are effectively isolated from one another, the equilibrium relationship between the fluid phase and the adsorbed phase becomes linear. This behaviour is described by Henry's Law:

$$q = KC \quad \text{or} \quad q = K'p \quad (2.6)$$

The constant of proportionality of the equation is the adsorption equilibrium constant and it is referred to the Henry's constant. From the ideal gas law, it follows that: $K = K'RT$.

As the concentration of the free-gas phase increases, more sites of the adsorbent are filled, and it becomes harder for new molecules to find free sites where they can be adsorbed. Consequently, the shape of the isotherm deviates from linearity and begins to exhibit a curved profile, reflecting the nonlinear relationship between adsorption capacity and pressure at higher concentrations. Brauner has classified different types of isotherms into five classes by their shape as illustrated in fig 2.7 (Brauner et al., 1940).

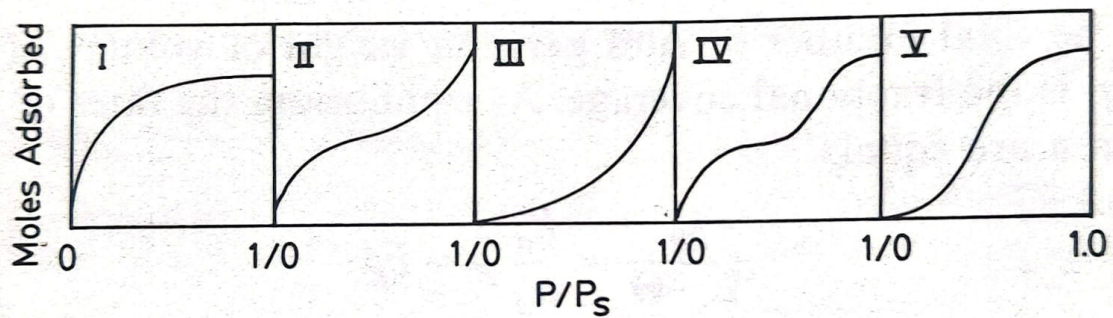


Figure 2.7: Classification of isotherms according to Brauner (Brauner et al., 1940).

A Type I adsorption isotherm is characterized by a clear saturation limit, which corresponds to the complete filling of micropores, and is typical of materials with narrow pore size distributions and high surface area, such as zeolites. In contrast, Type II and III isotherms are observed in adsorbents with a wide range of pore sizes, where adsorption progresses from monolayer formation to multilayer adsorption, eventually leading to capillary condensation in larger pores. A Type IV isotherm suggests the formation of two adsorbed layers, typically within mesoporous structures or along surfaces significantly wider than the adsorbate molecule diameter. Type V isotherms are associated with weak adsorbent–adsorbate interactions and become more prominent when intermolecular attraction between adsorbate molecules plays a dominant role in the adsorption process. In the analysis of adsorption column dynamics, it is useful to classify adsorption equilibria as "favourable," "linear," or "unfavourable", based on the shape of the dimensionless equilibrium curve. A favourable isotherm is characterized by the dimensionless adsorbed phase concentration (y axis) consistently exceeding that of the fluid phase (x axis). However, for desorption, where the direction of mass transfer is reversed, the interpretation of isotherm favourability is also reversed. An isotherm that is favourable for adsorption becomes unfavourable for desorption, and vice versa. In this thesis work it will be considered only adsorption isotherm of type I.

The simplest theoretical model to represent approximately adsorption equilibrium is due to Langmuir. The model is adopted for monolayer adsorption and is based on some assumptions here reported:

1. Molecules are adsorbed at a fixed number of well-defined localized sites.
2. Each site can hold one adsorbate molecule.
3. All sites are energetically equivalent.
4. There is no interaction between molecules adsorbed on neighbouring sites.

The assumptions of the Langmuir adsorption model lead to a simple mathematical expression for adsorption equilibrium that captures monolayer adsorption behaviour.

Adsorption and desorption rate can be written in terms of partial pressure as:

$$r_{ads} = k_a p (1 - \theta) \quad (2.7)$$

$$r_{des} = k_d \theta \quad (2.8)$$

Where $\theta = q/q_s$ is the extent of adsorbed coverage with q_s the maximum adsorbing capacity for the layer. Taking back eq. 2.4, and rearranging it:

$$\frac{\theta}{1 - \theta} = \frac{k_a}{k_d} p = bp \quad (2.9)$$

Where $b = k_a/k_d$ is the adsorption equilibrium constant. The final form of the Langmuir equation is given by:

$$\theta = \frac{q}{q_s} = \frac{bp}{1 + bp} \quad (2.10)$$

The Langmuir isotherm equation exhibits the correct asymptotic behaviour, as it approaches Henry's Law at low concentrations and reaches a saturation limit at high concentrations (Langmuir, 1918). The parameter b in the equation represents an equilibrium constant, which is directly related to the Henry's constant by the relation $K = bq_s$. Since adsorption is an exothermic process, the value of b , like K , decreases with increasing temperature, resulting in less sharply curved isotherms at elevated temperatures. Although relatively few systems conform exactly to the assumptions of the Langmuir model, many systems exhibit approximate conformity, particularly in the moderate concentration range. A key advantage of the Langmuir model is that it reduces to Henry's Law in the low-concentration limit, ensuring thermodynamic consistency—a necessary criterion for any physically realistic adsorption system. For these reasons, the Langmuir model is widely accepted as the foundation for many qualitative and semi-quantitative analyses of PSA systems.

The Langmuir model can be extended to binary and multicomponent systems, capturing the competitive behaviour of different species for available adsorption sites on the adsorbent surface:

$$\frac{q_A}{q_s} = \frac{b_A p_A}{1 + b_A p_A + b_B p_B + \dots} \quad (2.11)$$

$$\frac{q_B}{q_s} = \frac{b_B p_B}{1 + b_A p_A + b_B p_B + \dots} \quad (2.12)$$

At a given temperature and partial pressure, the amount of a component adsorbed in a multicomponent system will be lower than in a single-component system under the same conditions, due to competitive adsorption for available sites.

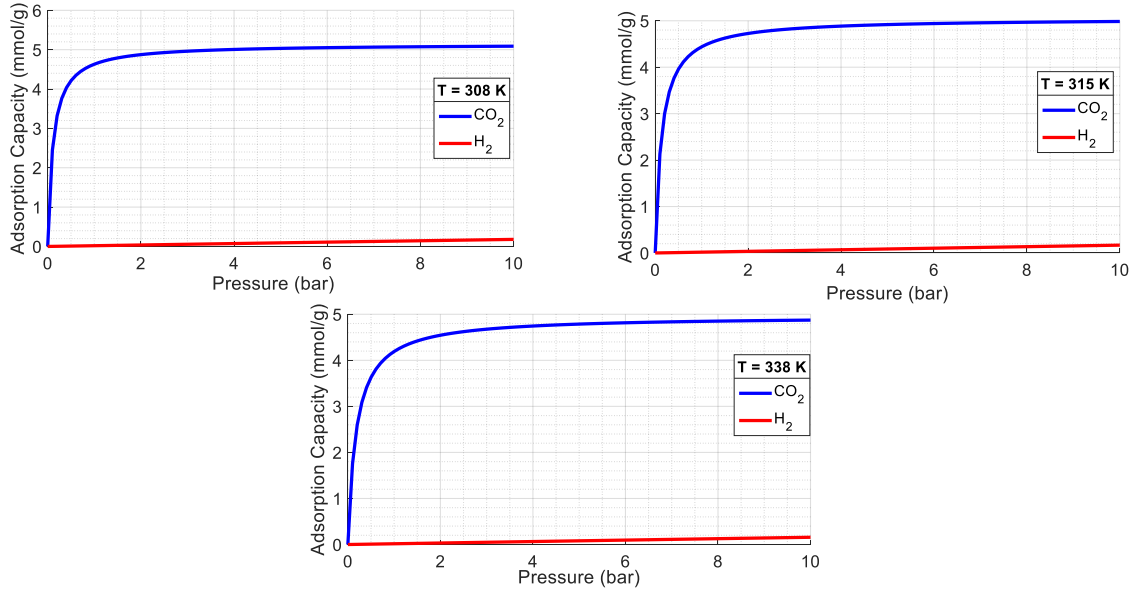


Figure 2.8: Langmuir isotherm of CO₂ and H₂ in zeolite 13X at three different temperatures: 308, 315 and 338 K.

The extended Langmuir model is widely used in the modelling of PSA systems, not only for its mathematical simplicity, but also because many PSA processes operate under relatively low loading conditions (typically $q/q_s < 0,5$), where the assumptions of the model remain reasonably valid. Other models that compensate for the inaccuracies of the Langmuir have been developed in the years, as for example the Freundlich model or the BET model.

2.2.3 Diffusion in porous media

The rate of physical adsorption is generally governed by diffusional limitations, rather than by the intrinsic rate of surface equilibration, which is typically very fast for physisorption due to the weak and non-specific nature of the interactions involved. In porous media adsorption and desorption rates are generally controlled by transport within the pore network. It is convenient to consider intraparticle transport as a diffusive process and to correlate kinetic data in terms of a diffusivity defined in accordance with the Fick's Law:

$$J = -D(c) \frac{\partial c}{\partial x} \quad (2.13)$$

Pore diffusion may occur by several different mechanisms depending on the pore. In fine micropores, the diffusing molecule remains constantly under the influence of the adsorbent's force field, and its movement occurs through an activated process—meaning the molecule must

overcome an energy barrier to move from one adsorption site to another. This stepwise motion, driven by thermal energy, resembles surface diffusion along the pore walls. However, steric restrictions also play a significant role. In many cases, the diffusional activation energy is largely determined by the size of the diffusing molecule relative to the smallest free diameter of the pore. In such confined environments, it becomes physically unrealistic to distinguish between molecules adsorbed on the pore walls and those considered "gaseous" in the centre of the pore. Consequently, it is more appropriate to treat all sorbate molecules within micropores as belonging to the adsorbed phase. Diffusion in larger pores (mesopores or macropores) such that the diffusing molecule escapes from the surface field is referred to as macropore diffusion. Four types of mechanisms contribute to transport within macropores:

- Molecular diffusion: When the pore diameter is large relative to the mean free path of the gas molecules, bulk or molecular diffusion becomes the dominant transport mechanism within the pores. The pore diffusivity in this case is proportional to the molecular diffusivity which may be retrieved from the Chapman-Enskog equation. Thus, it varies with the following relationship:

$$D_m \propto \frac{T^{1.7}}{P * \sqrt{M}} \quad (2.14)$$

Molecular diffusivity has an exponential dependence from the temperature with a grade equal to 1.7, while it is inversely proportional to the pressure. M is the mean molecular weight of the mixture. The dependence shown in equation 2.14 does not hold true for a binary gas mixture where the diffusion process is simply governed by collisions between just two types of molecules, and the statistical average behaviour stays consistent regardless of whether one component is in higher or lower concentration. The molecular diffusivity is then essentially independent from the composition. That is not true for multicomponent mixture even if the variations are generally relatively small (Yang, 1987)

- Knudsen flow: In molecular diffusion the resistance to flow arises from collisions between diffusing molecules. However, in small pores and at low pressure, the mean free path of the gas is greater than the pore diameter and collisions of the molecule with the pore walls occurs more frequently than collisions between molecules, providing the main diffusional resistance. This condition is called Knudsen flow and has the following relationship:

$$D_k \propto r \sqrt{\frac{T}{M}} \quad (2.15)$$

Where r is the pore radius. Also, it can exist a range in which both Knudsen and molecular diffusion are significant. In this intermediate region both intermolecular and wall collisions contribute to the diffusional resistance and the effective diffusivity depends on both type of diffusivity:

$$\frac{1}{D} = \frac{1}{D_m} + \frac{1}{D_k} \quad (2.16)$$

- **Poiseuille flow:** If a pressure gradient exists across an individual particle, there may be a direct contribution to the adsorption flux due to laminar flow through macropores. However, in most packed bed systems, this effect is negligible, as the pressure drop across a single particle is typically very small. Nevertheless, under conditions of high operating pressure and large pore sizes, this contribution can become more significant. This phenomenon is known as Poiseuille flow, and when present, its effect is added to the overall diffusional flux through the pore network
- **Surface diffusion:** As adsorption progresses, a layer of physically adsorbed particles forms on the macropore surface, potentially contributing to transport through the pore walls. Although these adsorbed molecules are less mobile than free gas molecules, they can still migrate by hopping from one adsorption site to another. This process is thermally activated and occurs along the pore walls. When the surface coverage is high—meaning many adsorption sites are occupied—the concentration of adsorbed molecules increases, and surface diffusion can contribute significantly to overall mass transport. In such cases, the thickness of the adsorbed layer becomes non-negligible, and even though the individual molecules move more slowly, the collective flux of the adsorbed phase can be substantial, especially in narrow or tortuous pores where gas-phase diffusion is limited.

2.3 PSA cycles: basic principles

The dynamic nature of a PSA process, driven by the need to regenerate the adsorbent once saturation is reached, entails that a PSA cycle consists of multiple steps, during which the column undergoes varying operations and conditions. Paragraph 2.1 introduced the two general macro-steps of the cycle: adsorption and regeneration of the adsorbent. This section provides a more detailed examination of the possible operational strategies within these steps and explores how they have evolved over time. Any PSA cycle can be regarded as a sequence of these elementary steps, the most common of which are described in the following sections. PSA processes differ in the order of the steps and in the specific way they are executed.

Table 2.3: Summary of the elementary steps used in PSA cycles (Ruthven, 1984).

Elementary step	Mode of operation	Principal features
Pressurization	1. Pressurization with feed from feed end.	Enrichment of the less selective adsorbed species in the gas phase at the product end.
	2. Pressurization with raffinate from the product end.	Sharpens the concentration front, which improves the purity and recovery of raffinate.
High-pressure adsorption	1. Raffinate withdrawal at constant column pressure.	Raffinate product is delivered at high pressure.
	2. The column pressure is allowed to decrease while the raffinate is drawn from the product end.	Very high recovery of the less selective adsorbed species may be achieved. but the product is delivered at low pressure.
Blowdown	1. Countercurrent blowdown to a low pressure.	Used when only raffinate is required at high purity; prevents contamination of the product end with strongly adsorbed species.
	2. Cocurrent blowdown to an intermediate pressure.	Used when extract product is also required in high purity; may also increase raffinate recovery.
Desorption at low pressure	1. Countercurrent desorption with product purge.	Improves raffinate purity at the expense of decrease in recovery: purge at sub atmospheric pressure reduces raffinate product loss but increases energy costs.
	2. Countercurrent desorption without external purge.	Recovery enhancement. Maintaining high product purity is possible only in certain kinetic separation.
	3. Vacuum evacuation.	High purity of both extract and raffinate products; advantageous over product purge when the adsorbed phase is very strongly held.
Pressure equalization	High- and low-pressure beds are either connected through their product ends or feed and product ends of the high-pressure bed are connected to the respective ends of the low-pressure bed.	Conserves energy and separative work.

Some of the most significant steps, their variants, along with their associated benefits, are summarized in Table 2.3 (Ruthven, 1984). It is important to note that in a PSA cycle a minimum of two adsorbent columns are used. The idea is the one to make the proper adsorption step to be carried out in different moment of the cycle. While one column undergoes the adsorption phase, the other can be simultaneously regenerated. This configuration allows for a cyclic exchange between adsorption and regeneration steps, but this do not include the fact that two columns are enough to guarantee continuous operation and cyclic steady state. As will be later explained continuous operations will be achieved with the adoption of the multiple bed system.

2.3.1 The Skarstrom cycle

Early PSA processes were developed using equilibrium selective adsorbents, with the objective to obtain highly pure raffinate products. In 1957, Skarstrom filed a patent with the United States Patent Office for a method and apparatus designed to remove nitrogen from a stream of atmospheric air, thereby increasing the oxygen concentration in the resulting effluent. This method gained widespread adoption in the following years due to its simplicity and high efficiency, laying the foundation for the modern PSA technology. This approach is particularly advantageous when the feed is supplied at high pressure, as it eliminates the need for additional mechanical energy typically required for compression. Furthermore, desorption can occur at atmospheric pressure, thereby avoiding the need for supplementary energy input associated with gas expansion. The Skarstrom cycle utilize two packed bed columns connected to each other and adopts four basic steps:

1. Pressurization.
2. High-pressure adsorption.
3. Blowdown.
4. Counter current purge.

In the cycle, the two columns operate in an alternating sequence, each performing the various process steps in turn. The valves there presented are of two types, the switching valves which simply allow or not the passage of the fluid through a pipe, and the backpressure regulator—the only valve represented with the hat—which maintains a certain pressure upstream the valve. During the initial step, the left column undergoes pressurization using the feed gas. In this phase, the feed valve remains open while the product (or refined) valve is closed, allowing the column to rapidly reach the desired feed pressure. Simultaneously, the right column initiates the blowdown phase by opening the vent valve, enabling depressurization in the direction opposite to the incoming feed flow. Once the column reaches the desired pressure, the second step begins with the opening of the product valve of the left bed, initiating the adsorption process. During this phase, the most readily adsorbed component is selectively retained within

the column, allowing for the recovery of a high purity raffinate at a pressure comparable to that of the feed.

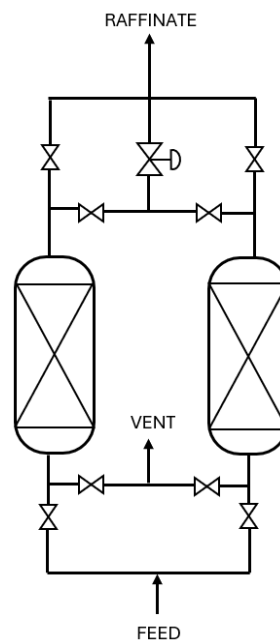


Figure 2.9: *The basic two-beds Skarstrom system.*

Simultaneously, a small fraction of the gaseous effluent is diverted through a control valve that connects the two columns. This purge stream is directed toward the right bed, which remains at low pressure following the preceding blowdown step. The purpose of the purge step is to flush the void spaces within the bed and to ensure that the end of the column—where the product will be withdrawn during the next half-cycle—is completely free of the strongly adsorbed component. The direction of the purge is also opposite to the one of the feeds. It is evident that increasing the purge flow enhances product purity; however, this improvement comes at the expense of reduced product recovery (Skarstrom, 1960). Beyond a certain point, the incremental gain in product quality becomes marginal compared to the corresponding loss in product quantity. After a certain period, the left column reaches the breakthrough point, indicating that the adsorbent has become saturated. The most strongly adsorbed species begins to appear in increasing concentrations in the raffinate product, signalling the need to initiate the regeneration phase of the column. Third and fourth step can then start following the same way of operation of the previous two with the bed interchanged. Fig 2.10 taken from the article of Quaranta et al., 2021, shows the four steps two bed cycle and highlights the valve opening during each of the phase of the process. Furthermore, the pressure trends for the two columns during the time is represented.

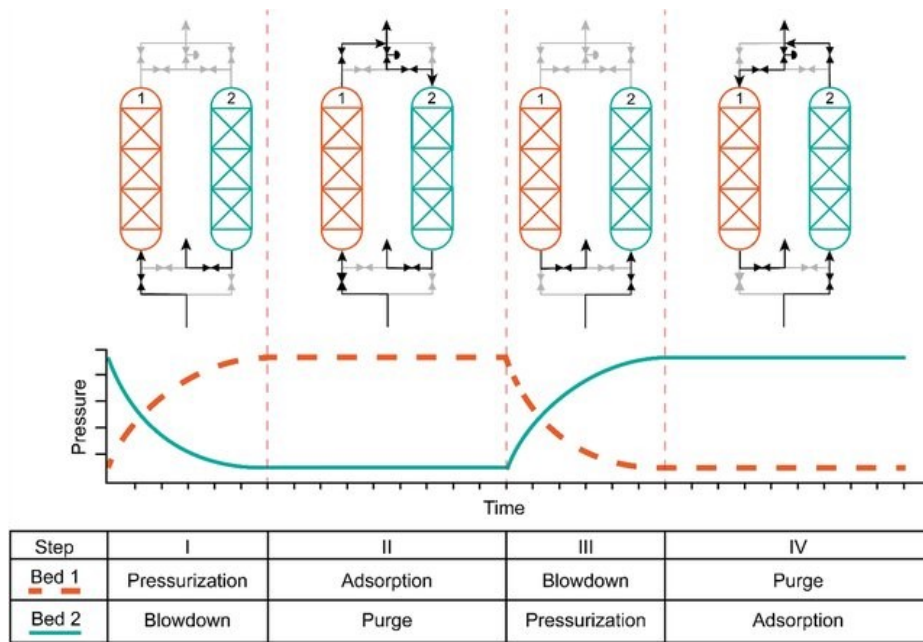


Figure 2.10: Skarstrom cycle steps and pressure history through the cycle (Quaranta et al., 2021).

Skarstrom suggested that, to achieve high purity of the desired product in a PSA process, it is important that the volume of purge gas used to clean the bed during the desorption step—measured at the lower purge pressure—is greater than the volume of feed gas introduced during adsorption—measured at the higher feed pressure. This ensures that impurities are effectively removed from every part of the bed in each cycle.

In a Skarstrom cycle, the effluent released during the blowdown and purge steps is typically regarded as waste gas. This stream is enriched in the more strongly adsorbed species but also contains a non-negligible fraction of the less strongly retained components. This loss directly impacts product recovery and must be accounted for in the overall economic assessment of the PSA process, as it represents a true loss of raffinate. The relative contribution of the blowdown and purge streams to the total loss of raffinate depends on the system’s operating pressure. Since the product is withdrawn at high pressure while purging occurs at atmospheric pressure, the portion of the product stream lost through purging is relatively small and becomes negligible when the pressure ratio is large. Conversely, blowdown losses increase with rising operating pressure and become the dominant source of product loss at higher pressures. The improved performance of more complex PSA cycles is largely attributed to the reduction of these blowdown losses.

2.3.2 Pressure equalization

Since the loss of raffinate during the blowdown step is directly linked to the pressure difference between the high and low operating levels, it became necessary to develop strategies for

reducing the column pressure prior to initiating the blowdown phase. In this sense the first innovation is due to Berlin which proposed the introduction of a fifth step to add to the Skarstrom cycle: the pressure equalization. After the first bed has been purged and the second bed has completed the high-pressure adsorption step, the two columns are connected at their product ends to allow for pressure equalization, rather than immediately initiating blowdown in the second bed. During this step, the first bed is partially pressurized using gas from the outlet region of the second bed. In that way the pressure of the two columns reaches an intermediate value between the high- and low-pressure level. Following pressure equalization, the columns are disconnected: the first bed is further pressurized with fresh feed gas, while the second bed undergoes venting to complete the blowdown phase. The pressure equalization step offers significant advantages. It conserves energy by utilizing compressed gas from the high-pressure bed to partially pressurize the low-pressure bed.

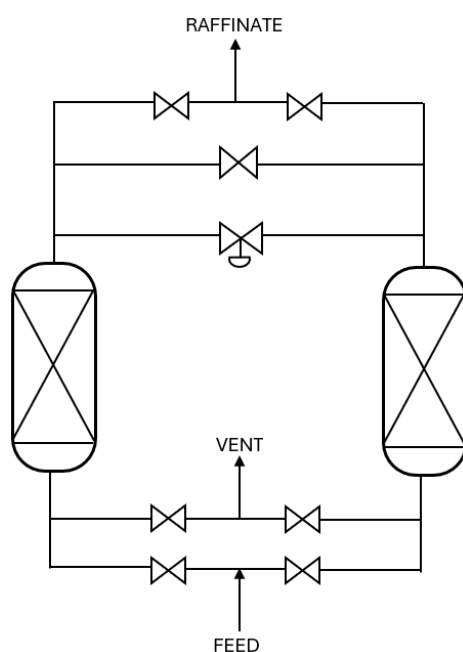


Figure 2.11: Schematic diagram of the Skarstrom cycle including pressure equalization

Additionally, since this gas is partially depleted of the strongly adsorbed species. As a result, the purge step does not waste valuable product, and the overall separation efficiency—or separative work—is largely maintained. Consequently, blowdown losses are reduced by approximately half, leading to a marked improvement in raffinate recovery. From the plant point of view a pipeline which connect the two columns must be added since there is the need for one that regulates the pressure and was present also in the original Skarstrom cycle and a second where switching valves regulate the passage of the gas. Figure 2.12 presents the steps of a Skarstrom cycle included of pressure equalization step.

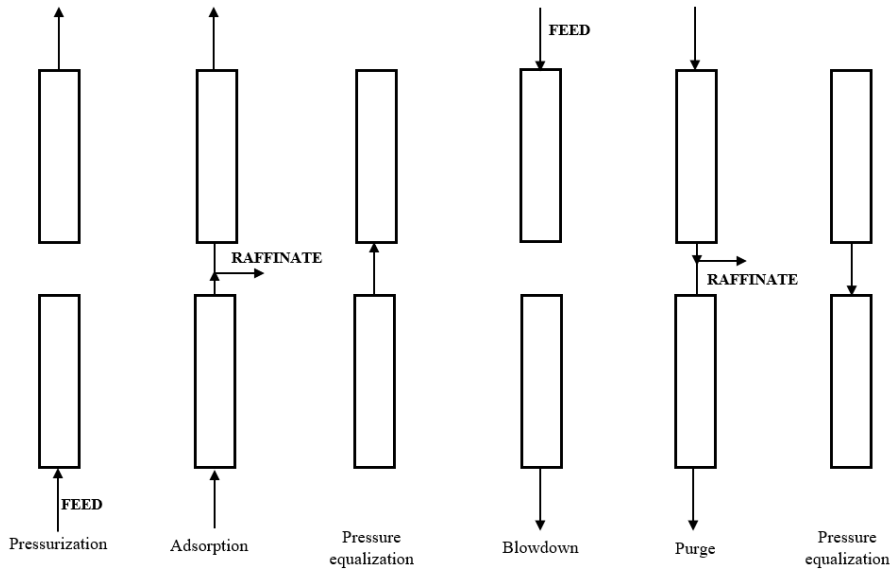


Figure 2.12: *Sequence of operations in the modified Skarstrom cycle including pressure equalization*

Prior to Berlin's modification of the Skarstrom cycle, an alternative approach to reducing blowdown losses was proposed in a patent assigned to Marsh et al. The process configuration involves the use of an empty storage tank in addition to the two adsorbent beds.

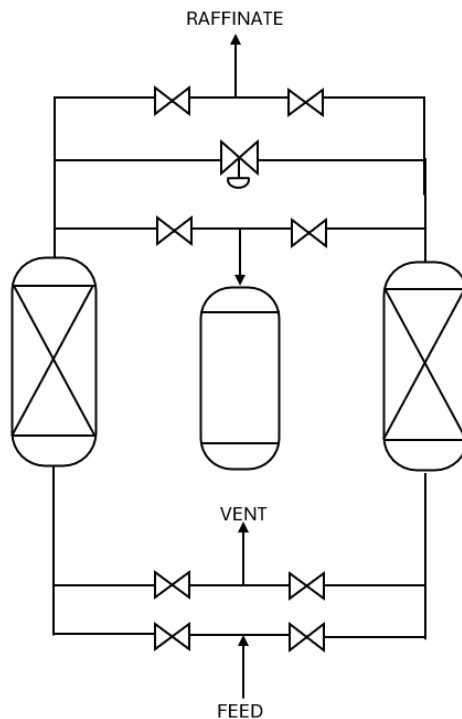


Figure 2.13: *Schematic diagram of a PSA cycle showing the use of a third empty tank*

At the end of the high-pressure adsorption step—well before breakthrough occurs—the feed flow is halted, and the product end of the high-pressure bed is connected to the empty tank. A portion of the compressed gas, rich in raffinate product, is transferred to the tank for temporary

storage. Subsequently, the high-pressure bed undergoes blowdown by venting to the atmosphere in the reverse-flow direction. The stored gas is then used to perform the initial purge of the bed, followed by a final purge using product gas. However, the energy savings associated with this method are generally lower than those achieved through direct pressure equalization.

2.3.3 Multiple-bed systems

Further improvements in PSA efficiency are typically achieved using multiple adsorbent beds, combined with a sequence of pressure equalization steps integrated into the cycle. In such multi-bed systems, blowdown gas from one column is often utilized to purge another, especially at pressure levels where additional equalization is no longer beneficial. This strategy results in enhanced recovery by reducing the amount of raffinate lost in the purge and blowdown phases. A representative example is illustrated in figure in figure 2.14 (Flowserve, 2017).

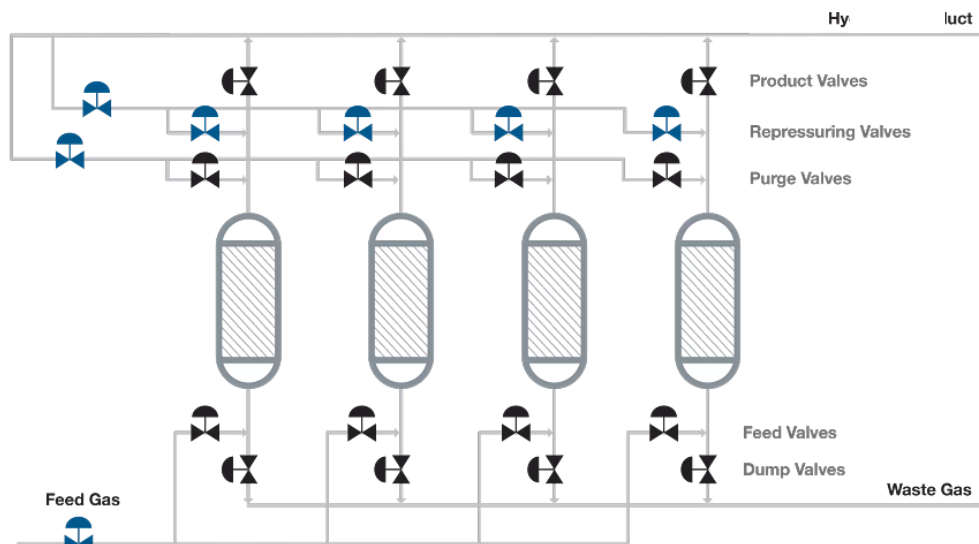


Figure 2.14: Schematic diagram of a four multi-bed PSA cycle (Flowserve, 2017).

In this type of configuration—involving three or more columns—one bed operates in the adsorption phase, while the others are in various stages of pressurization, depressurization, or purging. The system functions across two intermediate pressure levels, situated between the feed pressure and the exhaust pressure (usually atmospheric). At the end of the adsorption step, the column at high pressure is connected at its discharge end to a second column that has just completed purging and is at near-atmospheric pressure. Pressure equalization takes place, and a fraction of the remaining gas from the first bed is subsequently used to purge a third bed in reverse flow. Once the first bed reaches the desired low pressure, it is disconnected from bed 3 and vented to atmosphere through its inlet. It is then purged in reverse flow using gas from a fourth column and subsequently repressurized to the first intermediate pressure using gas from the second bed, which has just completed its adsorption step. Final repressurization is

performed using a portion of the product gas, after which feed is introduced to the inlet of the first bed. The complete cycle configuration is summarized in figure 2.15.

Vessel number												
1	Adsorption			PeD1	CoD	PeD2	CcD	Purge	PeP2	PeP1	Rep	
2	CcD	Purge	PeP2	PeP1	Rep		Adsorption			PeD1	CoD	PeD2
3	PeD1	CoD	PeD2	CcD	Purge	PeP2	PeP1	Rep		Adsorption		
4	PeP1	Rep		Adsorption			PeD1	CoD	PeD2	CcD	Purge	PeP2

PeD—Pressure equalization, depressurizing CcD— Countercurrent depressurization
 CoD—Cocurrent depressurization Rep—Repressurization

Figure 2.15: Four-bed PSA steps in the cycle

Pressurization with product gas helps displace residual adsorbates toward the feed end of the column, thereby improving product purity. Additionally, the multi-bed arrangement enables continuous product withdrawal and eliminates the need for a dedicated purge gas storage tank. A plant that employs three beds are enough to operate in continuous. Furthermore, while multi-bed systems significantly enhance energy efficiency and separative performance, they do so at the cost of increased process complexity. In some large-scale hydrogen purification PSA systems, configurations involving up to twelve adsorbent beds are employed to achieve optimal performance.

2.3.4 Vacuum swing cycle

In certain systems, the interactions between the adsorbed molecules and the adsorbent material can be highly favourable. As a result, a significant number of molecules remain adhered to the adsorbent surface even after the pressure is reduced during the blowdown step. In such cases, relying solely on a purge stream is not feasible, as it would require an impractically large volume of gas to thoroughly clean the bed. This challenge can be addressed by further lowering the pressure at which the bed is regenerated. Traditionally, blowdown is achieved by opening a valve that vents the column to the atmosphere, thereby reducing the internal pressure to atmospheric levels. However, applying a vacuum—thus lowering the pressure below atmospheric—also reduces the partial pressure of the adsorbed gas. This weakens the physical interactions between the gas and the adsorbent, thereby enabling more efficient desorption of the strongly adsorbed species. The simplest way to conceptualize a Vacuum Swing Adsorption (VSA) Cycle is as a modified Skarstrom cycle in which the low-pressure countercurrent product purge step is replaced by vacuum desorption. In this configuration, the product end of the

column remains closed, and a vacuum is applied through the feed end, as illustrated in Figure 2.16. When operated at the same high pressure as a conventional Skarstrom cycle, the VSC typically results in lower losses of the less strongly adsorbed species during evacuation compared to purge-based regeneration. This leads to an improvement in raffinate recovery, although at the cost of additional mechanical energy required for vacuum generation.

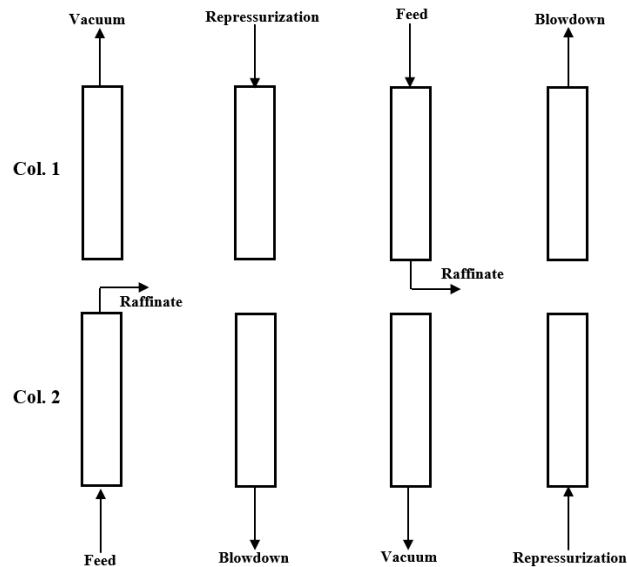


Figure 2.16: *Vacuum swing cycle simplified steps.*

Significant energy savings are possible if the cycle operates with a feed pressure slightly above atmospheric and a very low desorption pressure. In the low-pressure (linear) region of the adsorption isotherm, it is the pressure ratio—rather than the absolute pressure levels—that governs achievable purity and recovery. That is because is the pressure ratio that determines how well the adsorbent loads and releases the target gas. Consequently, a vacuum swing cycle is particularly advantageous over a Skarstrom cycle when a near atmospheric-pressure product is acceptable. However, the operating cost benefits may be partially offset by increased capital expenditures due to the larger equipment required due to the operation at atmospheric pressure. The concept of vacuum regeneration was originally proposed by Guerin de Montgareuil and Domine in a patent assigned to Air Liquide (Guérin de Montgareuil & Domine, 1964). However, the pressure swing cycle they described differs in several aspects' respects from the simplified VSA cycle shown in Figure 2.16. Depending on the nature of the gas mixture to be separated, the Air Liquide process may vary in terms of the number of adsorbent beds, the specific cycle steps, and other operating conditions. A two-bed version of this process is depicted in Figure 2.17. In this scheme, bed 1 is first pressurized to the high operating pressure via compressed feed gas introduced through the inlet. Once pressurized, the adsorption step starts retaining the most adsorbable component. After a certain time, close to the saturation of the first column, inlet is closed, and the gas is co-currently expanded through bed 2 (co-current

depressurization), with the effluent collected as raffinate product. When the pressure in bed 1 reaches a predetermined intermediate value, its discharge end is closed, and a vacuum line located at the centre of the bed is opened to initiate regeneration. Simultaneously, bed 2 begins repressurization: its inlet end is opened to the high-pressure feed stream while its discharge end remains closed. A primary drawback of the Air Liquide cycle is that the product is delivered at a sub-atmospheric pressure, which may limit its applicability in processes requiring higher delivery pressures. The improved raffinate recovery in VSA cycle results from two main factors: vacuum regeneration and co-current depressurization. The latter conserves a portion of the raffinate that would otherwise be lost, as it expels gas from the void spaces ahead of the mass transfer zone while retaining the more strongly adsorbed species near the product end. However, this advantage may diminish if co-current depressurization is combined with product purge regeneration, which can introduce the strongly adsorbed species into the product end. Depending on the feed composition and component affinities, the increase in purge demand may offset the recovery benefit.

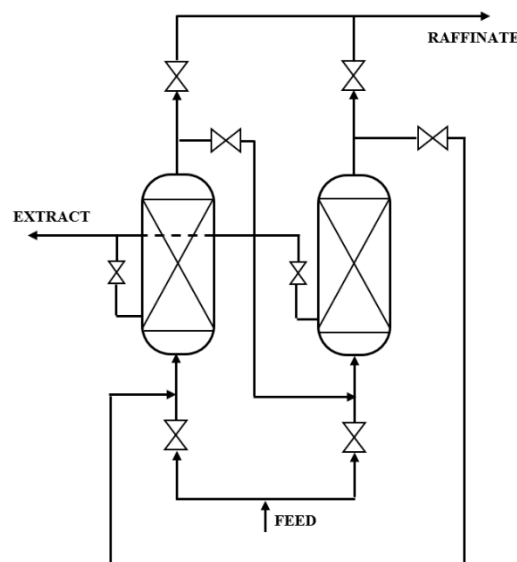


Figure 2.17: Schematic diagram of the two-bed Air Liquide PSA system. Bed 1 is the one on the left, bed 2 the one on the right.

Nevertheless, co-current depressurization remains valuable for enhancing the purity of the strongly adsorbed product. During high-pressure adsorption, the feed-penetrated region of the bed approaches equilibrium with the feed gas. Due to dispersive effects—such as mass transfer resistance, axial dispersion, and thermal gradients—the mass transfer zone spreads, leaving a region ahead of it available for further adsorption. When co-current depressurization is applied, the lighter component in the void spaces is expelled, and the concentration of the strongly adsorbed species increases in both the solid and gas phases. Vacuum desorption then effectively recovers this component at high purity and recovery. In cases where the extent of adsorption and consequently, the adsorbed-phase concentrations of the components are similar, co-current

depressurization may not sufficiently purify the extract. A more effective approach in such systems is to purge the void spaces with the strongly adsorbed species in the feed direction. The effluent from this step, having a feed-like composition and pressure, can often be recycled. Ultimately, the purity of the strongly adsorbed component depends critically on co-current depressurization or purging with the target species. Vacuum desorption becomes essential primarily when dealing with strongly adsorbed species exhibiting a Type I isotherm. For bulk separations involving components with moderate isotherm curvature, high-quality raffinate and extract products can often be obtained by cycling entirely within a pressure range above atmospheric.

2.4 Dynamics and operation of a PSA column

PSA processes are typically conducted using packed adsorption columns; therefore, a fundamental understanding of the dynamic behavior of a packed adsorbent bed is a critical prerequisite for accurate process modeling and analysis. In a packed bed column, the adsorbent particles are exposed to a time-dependent surface concentration. Under these conditions, the rates of sorption and desorption are influenced by both the mass transfer resistance and the temporal variation of the local gas-phase concentration:

$$q = f(C); C = f(t, z) \quad (2.17)$$

The dynamic behavior of an adsorption column is governed by the interplay among adsorption kinetics, equilibrium relationships, and fluid dynamics.

2.4.1 Pressure drops in packed beds.

Before discussing the inherent dynamics of a packed bed, it is important to briefly describe its physical structure. A packed bed typically consists of a cylindrical column filled with adsorbent particles characterized by a specific size distribution and porosity. In adsorption processes, the adsorbent interacts with the fluid phase, flowing through the void spaces between the particles. Key variables such as fluid velocity, particle size, bed porosity, and column dimensions significantly influence the pressure drop across the bed, which in turn affects both mass transfer efficiency (velocity of the fluid to be adsorbed) and the energy requirements of the process. Pressure drops in flow through packed beds have been investigated by several authors trying to carry out correlation to estimate them. One of the most widely used correlations for estimating pressure drop in packed beds is the Ergun equation (eq. 2.18), which accounts for both viscous and inertial contributions to flow resistance:

$$\frac{\Delta P}{L} = \frac{150\mu(1 - \epsilon)^2}{\epsilon^3 \phi^2 d_p^2} u + \frac{1.75\rho_g(1 - \epsilon)}{\epsilon^3 \phi d_p} u^2 \quad (2.18)$$

Where $\Delta P/L$ are the pressure drops for unit of length, μ and ρ_g are the viscosity and density of the gas phase, ε is the bed porosity and d_p the particle diameter of the adsorbent. The bed porosity, defined as the portion of the bed volume not occupied by adsorbent particles:

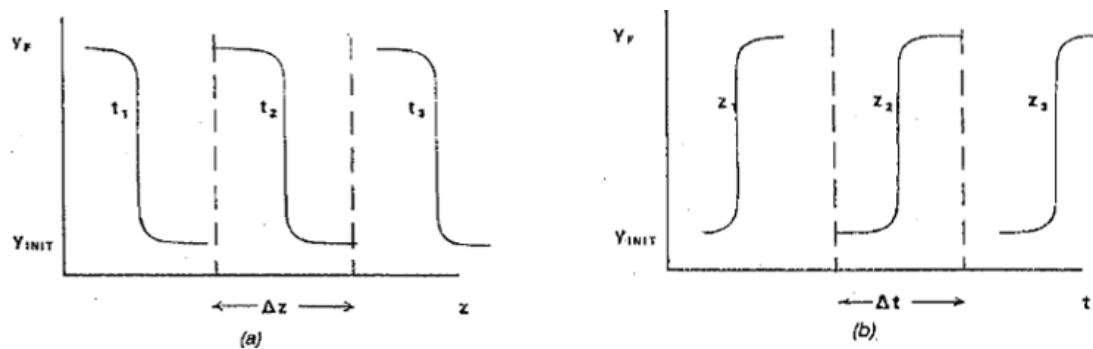
$$\varepsilon = \frac{V_{void}}{V_{Tot}} \quad (2.19)$$

As the void fraction increases, more space is available for gas flow, leading to a reduction in pressure drop. Conversely, a lower void fraction results in tighter packing, which restricts flow and significantly increases pressure losses. Packed beds with different void fractions will therefore have different energy efficiency and adsorption performance. Regarding the particle diameter, it also affects the extent of the pressure drops. Smaller particles create narrower flow channels and a larger surface area for interaction but also result in a higher pressure drop due to increased flow resistance. In contrast, larger particles offer less resistance to flow, leading to a lower pressure drop, but may reduce adsorption efficiency due to decreased surface area. Therefore, choosing the appropriate particle diameter involves a trade-off between mass transfer efficiency and energy consumption. Estimating the pressure drop in a column is therefore essential for achieving an appropriate design. The sizing of the column is carried out by considering the fluid properties, particularly the inlet velocity. By defining a maximum allowable pressure drop along the column, a corresponding maximum velocity can be determined using the Ergun equation. Based on this velocity and the known flow rate of the incoming fluid, the minimum required diameter of the column can then be calculated. This approach will be used in chapter 4 to size the PSA columns.

2.4.2 The adsorption front

In the context of a PSA process, the term *front* refers to the adsorption front, which denotes the region within the adsorbent bed where the adsorption of the target gas is actively occurring. As the gas mixture flows through the bed, this front advances along the column, separating the saturated region—where adsorption has already taken place—from the unsaturated region, where adsorption is ongoing or yet to begin. This dynamic behavior is effectively illustrated through breakthrough curves, which track the concentration of the target component in the effluent. These curves can be represented on two different bases: time-based and space-based (fig. 2.18). In time-based breakthrough curves (fig. 2.18 a), the effluent concentration of the most adsorbable component (Y), is represented as a function of time at a fixed position (typically the column outlet). The limits of the ordinate axis are written in figure 2.18 as Y_{init} which represent the minimum concentration of the highly adsorbed component in the gas phase after the adsorption and Y_F which is the concentration of the same component in the feed. These curves are particularly useful for determining operational parameters such as the breakthrough point, which marks the time when the impurity first appears in the outlet stream

in significant concentration and consequently the moment to apply the swing. In contrast, space-based breakthrough curves (fig. 2.18 b), plot the concentration along the bed length at a specific time. This spatial representation reveals the location and movement of the adsorption front within the column at various moments during the cycle. It allows for a more detailed visualization of how the front propagates through the bed and how far the mass transfer zone extends. Breakthrough curves are crucial for optimizing the PSA cycle. If the column is operated beyond the breakthrough point, impurities will begin to contaminate the product stream. Monitoring these curves helps define the optimal switching time for regeneration,



ensuring efficient use of the adsorbent.

Figure 2.18: (a) Space-based breakthrough curves: composition front for an adsorption step shown as three consecutive instantaneous profiles, as it passes through an element of adsorbent. (b) Time-based breakthrough curves: composition front for an adsorption step, shown as histories recorded at three consecutive axial positions within the adsorbent.

Furthermore, the shape and slope of the breakthrough curve provide insights into adsorbent performance. A steep, sharp front indicates high selectivity and effective mass transfer, whereas a gradual curve may point to adsorbent aging, low diffusivity, or poor separation. Overall, breakthrough curves reflect the dynamic behavior of the adsorption process, capturing both temporal and spatial aspects of how the adsorbent interacts with the feed gas and approaches saturation.

2.4.3 Mathematical model of a PSA column

The formal analysis of adsorption column dynamics begins with the fundamental differential equation derived from a transient mass balance on a differential element of the column. Considering an element of the bed through which a multicomponent ideal gaseous stream is flowing, the flow pattern of an adsorbable species can be represented by the axially dispersed plug flow model (Schmidt, 2005). The model is based on the following assumptions:

- One-dimensional flow: Variations are considered only along the axial direction (z -axis); radial gradients are neglected.

- Axial dispersion is included: Mass transfer along the axial direction is modelled with an axial dispersion coefficient D_L to account for non-ideal flow pattern phenomena (e.g. diffusion, eddies, back-mixing).
- No radial dispersion or gradients: Radial concentration and temperature gradients are assumed negligible.
- Ideal gas behaviour: The gas mixture behaves ideally, which simplifies the thermodynamic modelling.
- Constant or known pressure profile: Often, pressure is assumed to vary linearly along the column or be calculated from a momentum balance.
- No accumulation in the solid phase beyond sorption: The solid phase is stationary, and there's no axial movement of the adsorbent.
- Gas properties (e.g., viscosity, diffusivity) and bed properties (e.g., porosity, particle size) are often assumed constant

The consequent material balance hold that form:

$$\frac{\partial c_i}{\partial t} = D_L \frac{\partial^2 c_i}{\partial z^2} - \frac{\partial(v_s c_i)}{\partial z} - \left(\frac{1 - \varepsilon}{\varepsilon}\right) * \rho_s \frac{\partial q_i}{\partial t} \quad (2.20)$$

The left-hand-side represents the rate of accumulation of component i in the gas phase. During the adsorption step this term is expected to be negative since i passes from the gas to the adsorbed phase. The balance contains the adsorption rate expression of a single component which may be written as:

$$\frac{\partial q_i}{\partial t} = f(q_i, c_i) \quad (2.21)$$

This term represents how the amount of component i (typically expressed in mol/kg_{adsorbent}) in the adsorbed phase vary over the time. It is important since it contains the information of both the equilibrium isotherm and mass transfer resistance. Given the complexity of adsorption kinetics, numerous models have been developed over the years to describe the rate of adsorption with increasing accuracy. In the simplest approach, known as the equilibrium theory, mass transfer resistance is assumed to be negligible. Under this assumption, local equilibrium is considered to exist instantaneously at all points within the system. For an isothermal process, the adsorption rate is thus assumed to depend solely on the local gas-phase concentration. The shape of the isotherms influences the velocity at which the single component is adsorbed along the column. Although it serves as a valuable tool for understanding the fundamental separation potential and for guiding the initial design and analysis of PSA units, equilibrium theory tends to overestimate real system performance due to its simplifying assumptions. In most adsorption systems, the kinetics are predominantly controlled by intraparticle diffusion, modelling this

diffusion process requires the formulation of an additional differential equation along with its associated boundary conditions, which increases the complexity of the system. To simplify the analysis while still capturing the essential kinetic behaviour, diffusion-controlled kinetics are often approximated using the so- called Linear Driving Force (LDF) expression (Ruthven, 1984). The LDF model provides a satisfactory representation of the adsorption rate under a wide range of boundary conditions, offering a practical balance between accuracy and computational efficiency. The mass transfer rates are represented by linear driving force rate expressions:

$$\frac{\partial q_i}{\partial t} = k_i (q_i^* - q_i) \quad (2.21)$$

With k_i LDF mass transfer coefficient, which reflects how fast mass is transferred from the gas to the solid. A large k_i value indicates fast mass transfer and, consequently, a rapid system response, whereas a small k_i reflects slow mass transfer, signifying a strong resistance to mass transfer and a delayed response. This value contains the effective diffusivity of the component i in an adsorbent particle and can be estimated through empirical correlations. The adsorption rates term then contains also the terms q_i^* which represents the equilibrium loading from the isotherm at the local gas concentration and q_i which is the actual amount of component i in the adsorbed phase. If described by the Langmuir model the expression of q_i^* takes the following form:

$$q_i^* = q_{s,i} * \frac{b_i p_i}{1 + b_i p_i} \quad (2.22)$$

The term $q_{s,i}$ (saturation capacity), represents the maximum allowable capacity of the adsorbent for the component i . The adsorption rate term thus serves as a bridge between thermodynamics, represented by the adsorption isotherms, and kinetics, captured by the Linear Driving Force (LDF) model. An important detail in adsorption modelling is the definition of the void fraction ε . When the adsorbed phase concentrations are expressed on a particle volume basis, ε refers specifically to the extra-particle or interstitial bed voidage and can be expressed by equation 2.19. This definition is particularly appropriate when mass transfer rates are finite and the associated resistance arises from mechanisms such as external film diffusion, macropore diffusion, or solid-side mass transfer resistance at the particle surface (Perry et al., 2018). With this definition, the total bed density ρ_b and the solid particle density ρ_s are interrelated by the porosity ε :

$$\rho_b = (1 - \varepsilon)\rho_s \quad (2.24)$$

The bed voidage affect also the convective term $\partial(v_s c_i)/\partial z$ which shows how the flow of gas moves the component through the bed. The gas velocity appearing in this term refers to the

superficial velocity, which assumes that the entire cross-sectional area of the column is available for fluid flow, thereby neglecting the presence of solid particles. This superficial velocity can be related to the actual velocity of the gas flowing through the void spaces between the particles, known as the interstitial velocity, by accounting for the bed void fraction:

$$v_s = v_i \varepsilon \quad (2.25)$$

The interstitial velocity more accurately represents the actual behaviour of the fluid within the column, as it accounts for flow through the void spaces between the solid particles.

The effects of all mechanisms contributing to axial mixing—such as molecular diffusion, eddy diffusion, and flow maldistribution—are typically lumped into a single effective axial dispersion coefficient, D_L . This approach captures the essential non-idealities of one-dimensional flow without requiring more complex models, such as those accounting for radial dispersion, which are generally unnecessary. The axial dispersion term $D_L (\partial^2 c_i) / (\partial z^2)$ represents the spreading of concentration fronts along the column due to these mixing effects. While it can enhance model accuracy it is often negligible when mass transfer resistance is the dominant limiting factor. In such cases, the system may be approximated by plug flow (eq. 2.20), simplifying the mass balance without significant loss of accuracy.

$$\frac{\partial c_i}{\partial t} = - \frac{\partial(v_s c_i)}{\partial z} - \left(\frac{1 - \varepsilon}{\varepsilon} \right) * \rho_s \frac{\partial q_i}{\partial t} \quad (2.26)$$

This assumption is particularly valid in large-scale industrial units, where high velocities and column dimensions minimize axial mixing. In contrast, small laboratory columns may require inclusion of axial dispersion due to enhanced mixing effects, such as particle clustering, which disrupts uniform flow and leads to non-ideal breakthrough behaviour (Ruthven, 1984).

Chapter 3

Membrane gas separation

A membrane is a semi-permeable physical barrier that enables the selective transport of specific chemical species, typically driven by gradients in pressure, concentration, or chemical potential. Owing to this selective permeability, membranes are widely employed for separation and purification processes across numerous industries, including chemical, petrochemical, pharmaceutical, food, and environmental engineering. In gas separation applications, membranes offer an energy-efficient and compact alternative to conventional technologies.

3.1 General features of membrane separation

The basic configuration of a membrane separation module used in gas separation applications is shown in Figure 3.1. A feed gas mixture is introduced into the module, where selective transport occurs across the membrane. The membrane itself allows certain components to permeate through, driven by a partial pressure gradient. The permeate stream, enriched in the more permeable component, exits on one side of the membrane, typically under reduced pressure or with a sweep gas. The residue stream, containing the less permeable gases, exits on the opposite side and is called retentate (Lu et al., 2007).

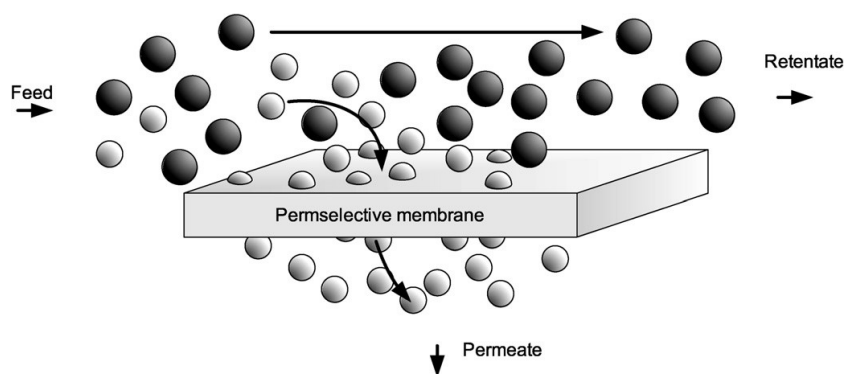


Figure 3.1: Basic schematic of a membrane gas separation (Lu et al., 2007).

Membranes used in separation processes can be classified based on their material composition, structure, and transport mechanism. Among the most widely employed are polymeric membranes, favoured for their low cost, ease of fabrication, and good processability, although they often exhibit a trade-off between permeability and selectivity. Inorganic membranes,

including those based on zeolites, silica, or carbon molecular sieves, offer higher thermal and chemical resistance as well as improved selectivity, but are typically more expensive and fragile. An emerging category is that of mixed matrix membranes (MMMs), which combine the processability of polymers with the enhanced performance of inorganic fillers, aiming to overcome the limitations of pure polymeric systems. Structurally, membranes may be either dense or porous. In modelling the transport of a fluid through a membrane, two main approaches are commonly used: the first one operate via the solution-diffusion mechanism, where gas molecules dissolve in the membrane material and diffuse through it at different rates. This mechanism is predominant in gas separation applications and will be seen in detail in the next paragraph. In contrast, the second model rely on Knudsen diffusion or molecular sieving, which are more suited to very small molecules like hydrogen. For gas separation, polymeric membranes are the most commercially applied. Indeed, in this thesis work there will be used a polymeric membrane made of PEBA^X® blended with PG. The characteristic of this membrane materials will be explained better in chapter 5. Inorganic and mixed matrix membranes are under active development and are considered promising for future applications that demand higher selectivity, greater resistance to harsh conditions, or improved long-term stability—particularly relevant for CO₂ capture technologies.

3.2 Solution-diffusion model

The most critical property of membranes is their ability to control the rate of permeation of different species. Two primary models are used to describe the mechanisms of gas transport, as illustrated in Figure 3.2. The first is the pore-flow model, in which permeants are transported by pressure-driven convective flow through microscopic pores. Separation occurs when certain permeants are excluded from specific pores, while others are allowed to pass through. The second is the solution-diffusion model, wherein permeants dissolve in the membrane material and subsequently diffuse across it, driven by a concentration gradient. In this case, separation is achieved due to differences in solubility and diffusivity of the permeants within the membrane material.

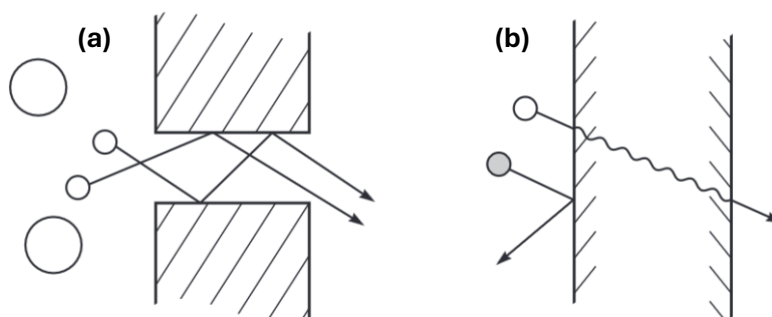


Figure 3.2: Molecular transport through membranes. (a) Pore-flow model. (b) Solution-diffusion model (Baker et al., 2012).

The key distinction between the solution-diffusion and pore-flow mechanisms lies in the size and permanence of the membrane's pores. In membranes where transport is governed by the solution-diffusion model, the pores are transient, consisting of minute free volume elements formed by the thermal motion of polymer chains. These pores appear and disappear on a timescale comparable to the motion of the permeant molecules, making the diffusion process inherently dynamic. Conversely, in membranes where transport follows the pore-flow model, the pores are relatively large, permanent, and interconnected. These structural characteristics remain stable over time, allowing for pressure-driven convective flow. The likelihood of observing pore-flow behaviour increases with the size and stability of these pores. As a general guideline, the transition between transient (solution-diffusion) and permanent (pore-flow) pore behaviour occurs at pore diameters in the range of 5–10 Å. Direct measurement of the average pore diameter is often challenging; it is typically inferred indirectly, based on the size of the permeating molecules or through other characterization techniques. Although microporous membranes remain a subject of active research, most commercial gas separation processes rely on dense polymer membranes, where separation occurs via the solution-diffusion mechanism (Baker, 2012).

3.2.1 Assumptions of the model

The mathematical description of diffusion in membranes begins with a fundamental thermodynamic principle: the driving forces of pressure, temperature, concentration, and electrical potential are interrelated. The overall driving force for the movement of a permeant is expressed as a gradient in its chemical potential, which integrates these factors into a unified framework for modelling transport through membranes. Thus, the flux of a component i is simply described by:

$$J_i = -L_i \frac{d\mu_i}{dx} \quad (3.1)$$

Where $d\mu_i/dx$ is the chemical potential gradient and L_i is a coefficient of proportionality which links the flux with the chemical potential. The solution-diffusion model is based on two fundamental assumptions:

1. The fluids on either side of the membrane are in thermodynamic equilibrium with the membrane material at the interface.
2. The driving force for permeation is entirely described by the concentration gradient of the dissolved permeant within the membrane, rather than by the external pressure or concentration differences alone.

According to the second assumption of the solution-diffusion model, the chemical potential gradient can be fully represented by a concentration gradient across the membrane. In gas

separation processes, this concentration difference arises from the application of different absolute pressures on either side of the membrane. The model assumes that the pressure within the membrane remains constant, typically equal to the feed-side pressure p_f . Under this condition, the concentration of a given component on the feed side increases with increasing p_f , and consequently, so does its partial pressure $p_{f,i}$. The concentration reaches a maximum when $p_{f,i}$ approaches the saturation vapor pressure of the component, $p_{sat,i}$. Thus, increasing the feed-side pressure enhances the concentration gradient and, in turn, the molecular flux through the membrane. Alternatively, the driving force can be increased by reducing the pressure on the permeate side p_l . If a sufficiently deep vacuum is applied, the permeate-side concentration of the target component approaches zero, thereby creating a steep concentration gradient relative to the feed side and significantly boosting the permeation flux.

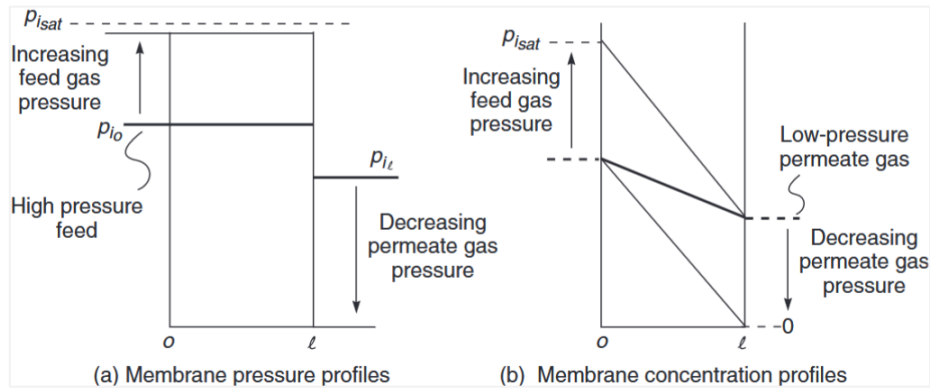


Figure 3.2.1 Changes in (a) the pressure and (b) the concentration profiles through a gas permeation membrane, according to the solution-diffusion model (Baker et al., 2012).

In gas separation therefore, the pressures on either side of the membrane must follow the relationship:

$$p_{sat,i} \geq p_{f,i} \geq p_{l,i} \quad (3.2)$$

3.2.2 Flux equation

Starting from equation 3.1 and considering the assumptions of the model, the flux equation can be rewritten in a form equal to the Fick's law:

$$J_i = -D_i \frac{dc_i}{dx} \quad (3.3)$$

And integrating through the membrane thickness:

$$J_i = D_i \frac{(c_{i,0,(m)} - c_{i,l,(m)})}{l} \quad (3.3)$$

Where D_i is the diffusion coefficient of species i that quantifies the mobility of gas molecules within the membrane material. $c_{i,0}$ and $c_{i,l}$ are the molar concentration at the feed side and at the permeate side of the membrane and l is the membrane thickness. Molar concentration can be defined by

$$c_i = MW_i \rho_i x_i \quad (3.4)$$

With MW_i , ρ_i , x_i , molecular weight, molar density and molar fraction of the component i . By considering the first assumption, the gas in the fluid in contact with the membrane at the feed (and in the permeate) interface are in equilibrium with the gas in the membrane phase. Thus, the chemical potential of the two phases can be set equal. By rearranging, the molar fraction at the feed membrane interphase can be represented in terms of activity coefficient:

$$x_{i,0,(m)} = \frac{\gamma_{i,0}^G}{\gamma_{i,0,(m)}} * \frac{p_0}{p_{i,sat}} * x_{i,0} \exp \left[\frac{-v_i (p_0 - p_{i,sat})}{RT} \right] \quad (3.5)$$

On the right-hand-side, $\gamma_{i,0}^G/\gamma_{i,0,(m)}$ is the ratio of the activity coefficients, with the numerator that refers to the one in the gas bulk phase and the denominator refers to the one at the interphase gas membrane. Then, $p_0/p_{i,sat}$ is the ratio of the absolute pressure on the feed side and the saturation vapor pressure of component i . The exponential term—known as the Poynting correction—quantifies how total pressure influences the partial pressure driving force. Importantly, v_i in this context refers not to the molar volume of component i in the gas phase, but to its partial molar volume in the membrane, which approximates its liquid molar volume. For most permanent gases, this correction factor is close to 1, and the molar fraction can be expressed through:

$$x_{i,0,(m)} = \frac{\gamma_{i,0}^G}{\gamma_{i,0,(m)}} * \frac{p_0}{p_{i,sat}} * x_{i,0} \quad (3.6)$$

Substituting concentration for mole fraction and expressing $p_0 x_{i,0}$ as the partial pressure $p_{i,0}$, Equation 3.4 can be rewritten as

$$c_{i,0,(m)} = \frac{MW_i \rho_i \gamma_{i,0}^G}{\gamma_{i,0,(m)} p_{i,sat}} * p_{i,0} \quad (3.7)$$

A sorption coefficient K_i can be defined:

$$K_i = \frac{MW_i \rho_i \gamma_{i,0}^G}{\gamma_{i,0,(m)} p_{i,sat}} \quad (3.8)$$

The sorption coefficient is determined by the gas–polymer interaction and quantifies the extent to which a gas dissolves into the membrane material under a given partial pressure. This coefficient is the one expressed for the Henry's law (Odani & Uyeda, 1991). The molar concentrations at the membrane side can be then represented as:

$$c_{i,0,(m)} = K_i * p_{i,0}; \quad c_{i,l,(m)} = K_i * p_{i,l} \quad (3.9)$$

K_i could be generally be assumed as constant for moderate pressure (< 20 bar) since at this pressure strong interactions between components of the mixtures are avoided and the Henry's law is followed. Equation 3.3 can be then expressed in terms of partial pressure and thus recast to:

$$J_i = D_i K_i \frac{(p_{i,0} - p_{i,l})}{l} \quad (3.10)$$

The product $D_i K_i$ can be written as a single coefficient, called the membrane permeability, and measures the ability of a membrane material to permeate a given component of a gas normalized for pressure driving force, and membrane thickness.

$$P_i = D_i K_i \quad (3.11)$$

For two components i and j in a gas mixture, the ratio of their permeability coefficients defines the membrane's selectivity, which measures its ability to separate the two gases. This ratio is a key performance indicator in gas separation applications, as it reflects the extent of separation achieved by the membrane and, consequently, its efficiency.

$$\alpha_{ij} = \frac{P_i}{P_j} = \left(\frac{D_i}{D_j} \right) \left(\frac{K_i}{K_j} \right) \quad (3.12)$$

The ratio (D_i/D_j) represents the diffusivity selectivity, reflecting the relative mobility of the two gas molecules and is primarily influenced by their molecular sizes. In contrast, the ratio (K_i/K_j) denotes the sorption (or solubility) selectivity, which is governed by the relative solubilities of the gases in the membrane material (Baker, 2012).

3.2.3 Sorption and diffusion coefficients

The sorption coefficient K_i for a given gas tends to remain surprisingly constant across a wide range of chemically diverse polymers. This behaviour arises from the fact that gas sorption in most polymers resembles that in ideal liquids. It can be demonstrated that all ideal liquids exhibit similar sorption capacities for the same gas, and that the sorption of different gases is inversely proportional to their saturation vapor pressure. A practical approximation for saturation vapor pressure is the gas boiling point or critical temperature, making it possible to correlate gas sorption behaviour with critical temperature as a convenient predictive parameter. In contrast to gas sorption, gas diffusion coefficients vary significantly with the type of polymer material. For example, diffusion coefficients in natural rubber are relatively high and often within one order of magnitude of those observed in liquids such as water. Conversely, in unplasticized polyvinylchloride—a rigid, high glass transition temperature, amorphous glassy

polymer—gas diffusion coefficients can be 5 to 8 orders of magnitude lower. Additionally, as the molecular size of the gas permeant increases, its diffusion coefficient decreases sharply. Most polymers exhibit diffusion behaviour that falls between these two extremes, representing the typical range observed in practical applications.

In polymeric membranes operating via the solution-diffusion mechanism, high selectivity between two gases is best achieved when the permeating component is both smaller and more condensable than the non-permeating one. A typical example is the separation of CO₂ from methane. CO₂ has a slightly smaller kinetic diameter than methane, resulting in mobility selectivity which is the ratio of the diffusion coefficients ranging from 2 to 10. In addition, CO₂ is significantly more condensable, leading to sorption selectivity of 3 to 4. The combined effect yields overall selectivity between 6 and 40 in favour of CO₂, making it the preferentially permeating species in most polymeric membranes. However, in some applications, the sorption and diffusion selectivity may oppose each other. A notable example is the separation of hydrogen from CO₂, a key process in hydrogen production plants. CO₂, with a boiling point of −56 °C, is much more condensable than hydrogen (boiling point −253 °C), which gives a sorption selectivity that favours CO₂. In contrast, hydrogen has a smaller kinetic diameter, so the diffusivity selectivity favours hydrogen transport. Depending on the polymer structure and properties, it is therefore possible to engineer membranes that selectively permeate either CO₂, driven by sorption selectivity, or H₂, driven by diffusivity selectivity. Trade-off between permeability and selectivity between two pure gases can be found in a type of graph called Robeson plot. Figure 3.4 represent the Robeson plot for hydrogen and carbon dioxide.

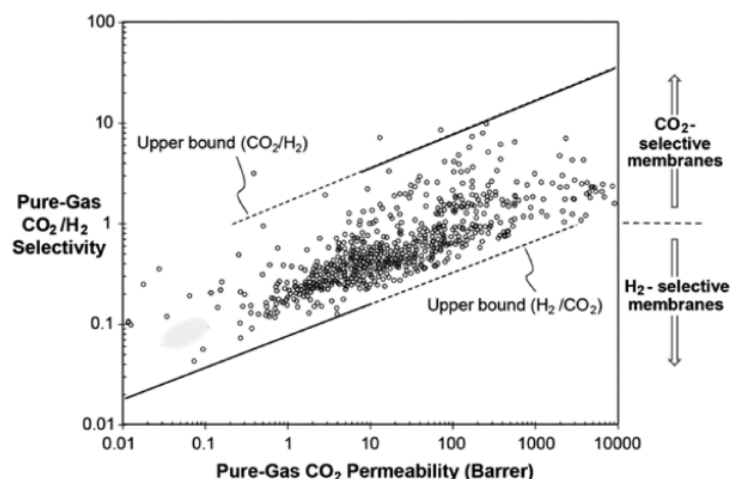


Figure 3.4: Robeson plot for commercially CO₂-H₂ membrane gas separation (Baker & Low, 2014).

Many materials are shown by the dot, but the most permeable material at a particular selectivity is of the most interest. The line that links these materials is called the upper bound, beyond

which no better materials are known. Upper bounds are shown for both type membranes in which the separation occur in favour of hydrogen and CO₂ (Baker & Low, 2014).

3.3 Membrane types for H₂/CO₂ separation

Several types of membranes have been extensively investigated for gas separation over the years. This section briefly summarizes the main categories used for hydrogen and carbon dioxide separation, with the aim of familiarizing the reader with the membrane technologies relevant to this application. Most commonly, membranes are designed to preferentially permeate hydrogen while retaining CO₂. However, since the focus here is on CO₂ capture, particular attention is given to membranes that preferentially permeate CO₂ and retain hydrogen.

3.3.1 Membrane modules

Industrial membrane plants often require hundreds to thousands of square meters of membrane surface to achieve the desired separation at commercial scale. To enable this, membranes must be packaged efficiently and economically into compact units known as membrane modules. A module is then the smallest unit into which the membrane area is packed. The earliest membrane module designs were based on conventional filtration technology and consisted of flat sheet membranes arranged in a structure like a filter press. These are known as plate-and-frame modules. Membranes, feed spacers, and product spacers are layered together between two end plates in the module assembly. The feed mixture is forced to flow across the surface of the membrane. A portion of the gas permeates through the membrane, enters the permeate channel, and is then directed to a central permeate collection manifold. In tubular membrane systems, five to seven smaller tubes are nested within a larger outer tube that serves as the pressure vessel, allowing for a higher membrane surface area within a compact module. Multiple tubes are manifolded in series, with the permeate collected from each tube and directed to a common header. The feed flows through all connected tubes in series, maintaining a high fluid velocity that helps minimize membrane fouling. Both plate-and-frame and tubular modules are still used but since their cost can be expensive, they have been replaced by other types of design. Gas separation membrane can be packed into spiral-wound or hollow-fiber modules.

The spiral wound modules design shown in Figure 3.5, consists of a membrane envelope of spacers and membrane wound around a perforated central collection tube; the module is placed inside a tubular pressure vessel. Feed passes axially down the module across the membrane envelope. A portion of the feed permeates into the membrane envelope, where it spirals toward the centre and exits through the collection tube.

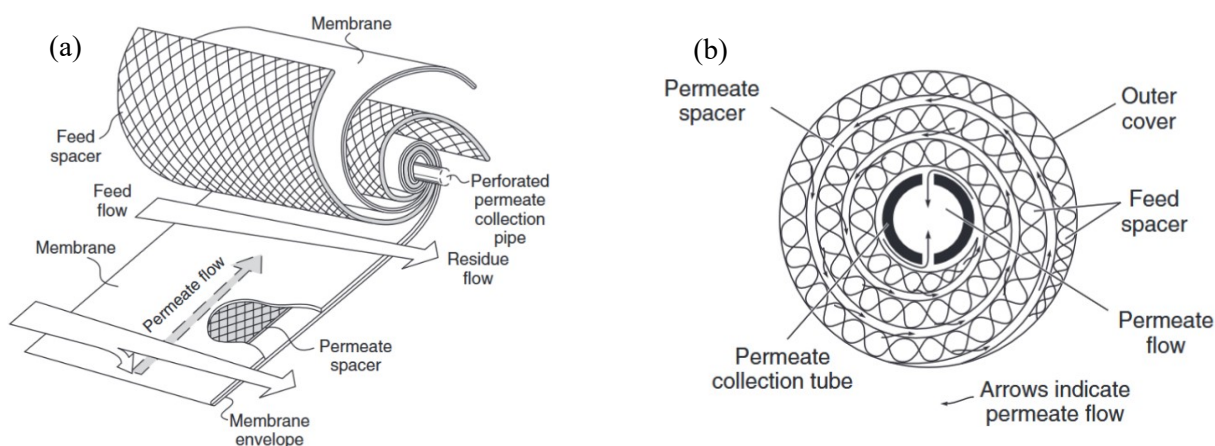


Figure 3.5: *Spiral-wound module. (a) Exploded view. (b) Cross-section view (Baker, 2012).*

For many years, the standard spiral-wound module used in industrial gas separation had a diameter of 20 cm and a length of 1 m. However, recent trends show a shift toward larger diameters, with modules of 40 cm now commonly adopted in large-scale plants to increase membrane area and improve process efficiency.

Hollow fiber membrane modules are typically configured in two main geometries: shell-side feed and bore-side feed designs. In the shell-side feed configuration (Figure 3.6 a), a closed bundle or loop of fibres is enclosed in a pressure vessel. The feed gas is applied externally, on the shell side, and permeates through the fiber walls. The permeate exits via the open ends of the fibres. This design is cost-effective, supports high membrane surface area, and is structurally robust. Due to the need to withstand substantial hydrostatic pressure, the fibres have small internal diameters ($\sim 50 \mu\text{m}$) and thick walls ($100\text{--}200 \mu\text{m}$ outer diameter). In the bore-side feed configuration (Figure 3.6b), the feed flows internally through fibres that are open at both ends.

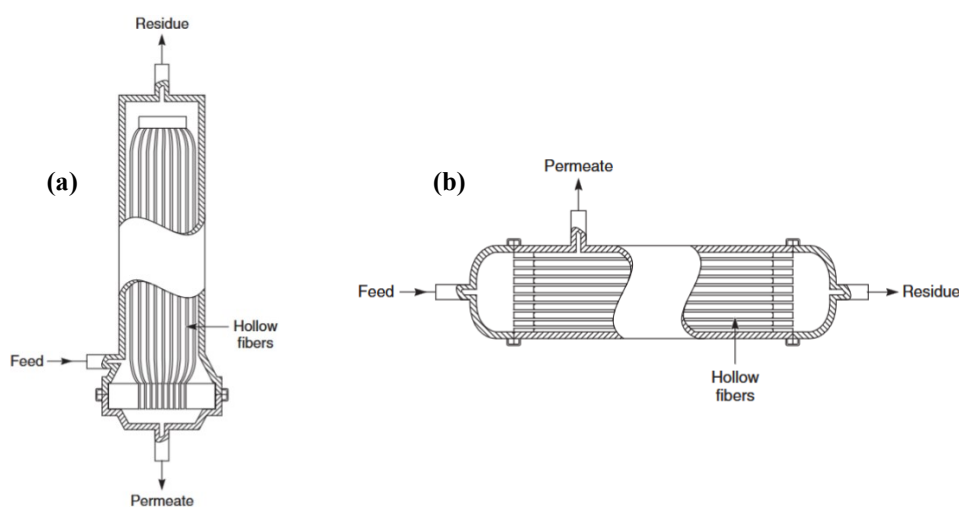


Figure 3.6: *Hollow-fibre module. (a) Shell side feed design. (b) Bore side feed design (Baker, 2012).*

To reduce pressure drops, these capillary fibres are larger in diameter. This geometry is suitable for low-to medium-pressure gas separations, with operating pressures generally below 150 psig.

3.3.2 Polymeric CO₂ selective membranes

For polymeric membranes to exhibit CO₂ selectivity, it is essential that solubility selectivity strongly favours CO₂, while diffusivity selectivity, which typically favours H₂, is minimized. In all polymers, the diffusion coefficient decreases with increasing molecular size of the permeant, as larger molecules interact with more segments of the polymer chains than smaller ones. As a result, mobility selectivity inherently favours the passage of smaller molecules. However, the extent of this selectivity strongly depends on whether the membrane material operates above or below its glass transition temperature (T_g). Below T_g , polymer chains are essentially fixed with limited segmental motion, and the material behaves as a glassy polymer—tough and rigid. Above T_g , thermal energy allows some rotation of chain segments, giving the polymer rubbery characteristics with drastically different mechanical and transport properties. Rubbery polymers are particularly suitable for this purpose due to the high mobility of their chains, which enhances gas diffusivity. These materials also tend to favour the solubility of condensable gases like CO₂, organic vapours, and hydrocarbons. To the aim of this thesis there must be then selected a membrane material which T_g is lower than the operative temperature. Common examples include polydimethylsiloxane (PDMS) and polyamide-b-ethylene oxide (PEBAX[®]). To further enhance CO₂ selectivity, membranes can be designed with polar functional groups—as found in polymers such as polyether oxide and polypropylene oxide—which interact more strongly with CO₂ than with non-polar gases like H₂. Table 3.1 lists a series of polymeric membrane used for CO₂ separation from hydrogen. Molecular size, shape, and chemical affinity all play critical roles in optimizing membrane performance for selective gas separation. CO₂ permeability and selectivity are highly dependent on temperature and pressure. At higher CO₂ partial pressures, membranes tend to plasticize, resulting in increased permeability of all gases, which can reduce selectivity. Conversely, lower temperatures enhance CO₂ solubility in the membrane, which can lead to improved CO₂ permeability and overall selectivity (Duthie et al., 2007).

Table 3.1: *CO₂ permeability and selectivity with respect to H₂ through a range of facilitated transport membranes. All data is based on single gas measurements at the cited temperature and pressure.*

<i>Membrane</i>	<i>CO₂ permeability (Barrer)</i>	<i>CO₂/H₂ selectivity</i>	<i>Temperature (°C)</i>	<i>Pressure (atm)</i>	<i>Reference</i>
<i>Poly(styrene-co-butadiene)</i>	15	1.9	30	2	Orme et al. (2003)
<i>Poly(ethylene oxide)-semicrystalline</i>	17	9.9	35	14.6	Lin and Freeman (2004)
<i>PEBAX[®] 3533</i>	20	6.1	25	4	Kim et al. (2001)
<i>Poly(cis-isoprene)</i>	134	2.7	35	5	Bondar et al. (2000)
<i>PEBAX[®]-PG</i>	28	15.5	35	10	Franz & Scherer (2010)
<i>PDMS</i>	3100	4.3	35	5	Orme et al. (2003)
<i>PDMS</i>	1300	3.5	30	2.04	Orme et al. (2003)

The performance of polymeric membranes in gas mixtures typically declines compared to pure gas conditions due to competitive sorption and plasticization effects. Additionally, maintaining long-term separation efficiency is a critical factor, as membrane properties can degrade over time under operational conditions.

3.3.3 Facilitated transport membranes

Facilitated transport membranes are an advancement of traditional polymeric membranes, incorporating a facilitator species that undergoes reversible complexation with CO₂ inside the membrane, dramatically enhancing solubility. This mechanism, analogous to solvent absorption, adds an extra separation pathway to the conventional solution-diffusion process. Typically, these membranes use water-soluble polymers like polyvinyl alcohol, forming hydrogels in the presence of humidified feed gas. The facilitator—which can be either fixed-site or mobile—transports CO₂ across the membrane. Common facilitators include amine groups, polar polymers, and ionic liquids. The performance of such membranes depends critically on the selectivity and reversibility of the CO₂-facilitator interaction, though the partial pressure difference across the membrane remains the main driving force. Facilitated transport membranes offer high CO₂ permeability and excellent selectivity, especially at low CO₂ partial pressures, making them valuable for CO₂/H₂ separation. Compared to rubbery polymers, they often exhibit a tenfold increase in selectivity. However, it is important to note that the selectivity of these materials decreases markedly as the CO₂ partial pressure increases (Scholes et al., 2010). Once all carriers are occupied, further increases in CO₂ pressure no longer enhance flux,

causing permeability and selectivity to drop. This behaviour limits their effectiveness in high-pressure applications such as IGCC (Integrated Gasification Combined Cycle) processes. Table 3.2 shows various types of facilitated transport membranes:

Table 3.2: Carbon dioxide permeability and selectivity with respect to H_2 through a range of facilitated transport membranes. All data is based on single gas measurements at the cited temperature and pressure.

<i>Membrane</i>	<i>CO₂ permeability (Barrer)</i>	<i>CO₂/H₂ selectivity</i>	<i>Temperature (°C)</i>	<i>Pressure (atm)</i>	<i>Reference</i>
<i>PVBTAf composite</i>	6.0	87	23	0.5	Quinn and Laciak (1997)
<i>[(CH₃)₄N]F-4H₂O</i>	445	10	50	0.3	Quinn et al. (1995)
<i>Chitosan membrane</i>	482	43	110	1.5	El-Azzami and Grulke (2008)
<i>[hmim][Tf2N]</i>	900	7	100	1	Myers et al. (2008)
<i>PEI-SPBI composite</i>	1262	50	100	2	Bai and Ho (2009)

Other challenges include:

- Temperature sensitivity, as higher temperatures cause water loss and hinder CO₂ transport.
- Mechanical instability, where the liquid phase cannot be retained under large pressure gradients.
- Chemical degradation of the facilitator due to reactive trace components like NH₃ and H₂S.

These limitations have so far prevented commercial deployment of facilitated transport membranes in syngas applications, despite promising lab-scale performance.

3.4 Process design

This section provides the foundational concepts needed to understand the basic design of a membrane separation system. The key factors influencing the choice of a specific configuration include membrane selectivity, pressure ratio, and stage cut—each of which will be examined in detail later. Beyond these parameters, two critical decisions must be made when designing a membrane system:

1. Whether a single-stage configuration is sufficient, or if a multi-stage system is required to achieve the desired separation performance.

2. If a multi-stage system is selected, whether incorporating a recycle stream can improve overall efficiency or recovery.

3.4.1 Design factors

The three factors that determine the performance of a membrane gas separation system are the membrane selectivity, the pressure ratio and the stage cut. Selectivity definition and effect has already been presented in paragraph 3.1.2. Thus, there must be understood how the other two parameters affect the separation process. The pressure ratio is defined as the ratio of the absolute pressure at the feed (p_0) and at the permeate side of the membrane (p_l).

$$\varphi = \frac{p_0}{p_l} \quad (3.13)$$

A flow of component i across the membrane can only occur if the partial pressure of i on the feed side of the membrane $x_{i,0}p_0$ is greater than the partial pressure of i on the permeate side of the membrane $x_{i,l}p_l$, it follows that:

$$\frac{x_{i,l}}{x_{i,0}} \leq \varphi \quad (3.14)$$

Pressure ratio and selectivity are key parameters whose relative values help determine which factor most strongly influences the membrane separation performance. By analysing the interplay between these two, it is possible to identify whether the driving force for separation is primarily governed by the pressure differential or by the membrane's intrinsic ability to discriminate between different gas species. Two limiting cases can be considered. If the membrane selectivity is greater than pressure ratio:

$$\alpha \geq \varphi \quad (3.15)$$

This operating condition is referred to as the pressure-ratio-limited region, where the separation performance is dictated solely by the pressure ratio across the membrane. In this regime, the membrane selectivity has negligible influence on the overall process efficiency.

If membrane selectivity is smaller than pressure ratio:

$$\alpha \leq \varphi \quad (3.16)$$

This condition is known as the membrane-selectivity-limited region, where the membrane's separation performance is governed exclusively by its selectivity, with minimal influence from the pressure ratio. Naturally, there exists an intermediate region between the pressure-ratio-limited and membrane-selectivity-limited extremes, wherein both factors—pressure ratio and membrane selectivity—contribute to determining the system's efficiency. These three

operational regimes are depicted in Figure 3.7, where the calculated permeate concentration is plotted against the pressure ratio for a membrane with a selectivity of 30.

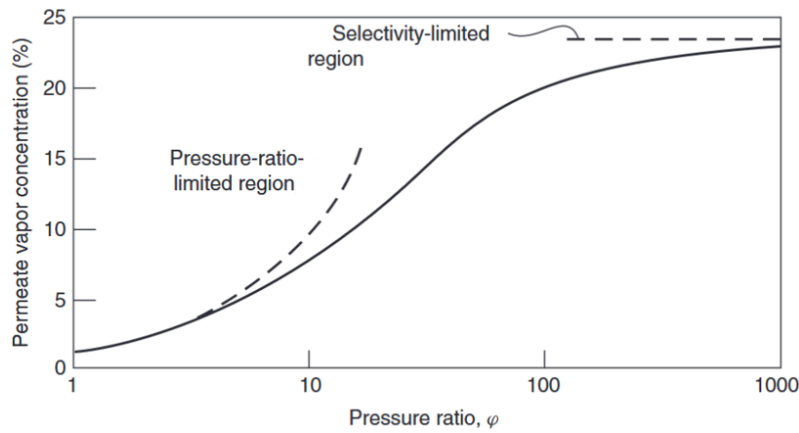


Figure 3.7: Permeate vapor concentration, for a vapor-permeable membrane with a vapor/nitrogen selectivity of 30, as a function of pressure ratio (Baker, 2012).

At a pressure ratio of 1, where the feed and permeate pressures are equal, the membrane is unable to induce any separation. As the pressure difference increases, the concentration of the more permeable component in the permeate stream also increases. In the intermediate region, where both the pressure ratio and membrane selectivity contribute to performance, the rate of increase in permeate concentration begins to diverge from the initial trend. At very high-pressure ratios—typically four to five times greater than the membrane selectivity—the system enters the membrane-selectivity-controlled region, where further increases in pressure ratio yield minimal improvements, and the separation is essentially governed by the membrane’s intrinsic selectivity. In this region the permeate concentration reaches the limiting value. The relationship between pressure ratio and membrane selectivity is crucial, given the practical limitations of pressure ratios in gas separation systems. Achieving extremely high-pressure ratios—either by compressing the feed stream to very high pressures or by applying a deep vacuum on the permeate side—demands substantial energy input and costly compression or vacuum equipment. Consequently, in industrial applications, pressure ratios are typically constrained to a range of 5–20, balancing technical feasibility and economic sustainability. Another key factor influencing membrane system design is the degree of separation required. In most gas separation applications, the objective is to produce a residue stream depleted of the more permeable component and a permeate stream enriched in that component. However, these goals are inherently conflicting; achieving high removal from the feed often comes at the expense of permeate purity, and vice versa. This trade-off between feed component removal and permeate enrichment is quantitatively described by the third main parameter known as the stage-cut:

$$\theta = \frac{\text{Permeate flow}}{\text{Feed flow}} \quad (3.17)$$

A low stage cut favours the production of a permeate stream with high purity, as only the most permeable components pass through the membrane. However, this comes at the expense of recovery, which remains low due to the limited fraction of feed processed. Conversely, a high stage cut increases recovery but leads to a decline in permeate purity, as the permeate composition begins to resemble that of the feed. Additionally, increasing the stage cut reduces the partial pressure driving force across the membrane, potentially lowering the separation efficiency and requiring a larger membrane area to maintain throughput. Therefore, optimizing the stage cut involves a trade-off between purity, recovery, and membrane area, and in many applications, multi-stage configurations are employed to balance these competing objectives.

3.4.2 Multistep and recycle system design

Due to the inherent limitations in membrane selectivity and achievable pressure ratio in commercial membrane systems, a single-stage configuration may be insufficient to attain the desired level of separation. In such cases, the stream that is necessary to purify can undergo a second separation step using a different membrane from the first. The way in which the operation is carried out changes based on the objective to be achieved. In certain cases, it may be necessary, following an initial membrane separation step, to further remove a specific component from the permeate stream to obtain a retentate that meets environmental standards for discharge, ensuring minimal concentrations of the most permeable component. This could be, for example, the case of a nitrogen feed stream from which Volatile Organic Compounds (VOC) must be removed as shown in figure 3.8.

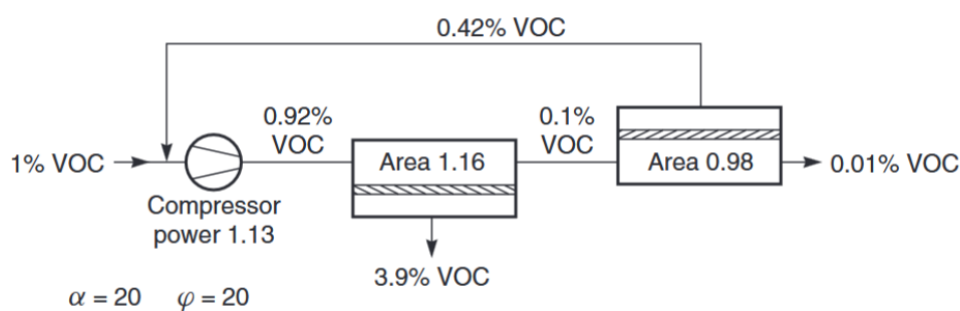


Figure 3.8: A two-step system to achieve 99% vapor removal from the feed stream (Baker, 2012).

A second membrane stage is therefore installed downstream of the first stage's retentate, where the VOC concentration is further reduced to nearly zero. Due to the low concentration of VOCs in the feed to this second membrane unit, the resulting permeate stream is relatively dilute and is recirculated back to the feed stream of the first stage, thereby enhancing overall process efficiency.

The other situation that can happen is the one in which after a first stage of membrane separation, the composition of permeate needs to be further increased. In the case of VOCs for

example it may be desired to obtain a product of much higher composition also to have a retentate that can be full of nitrogen.

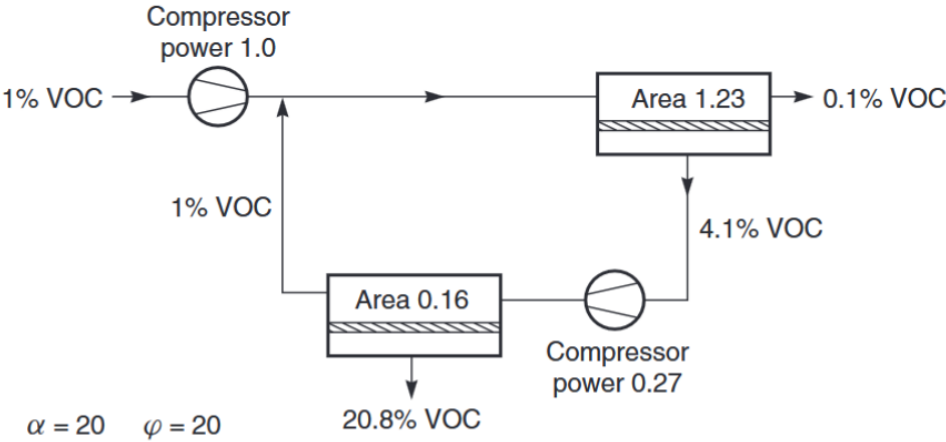


Figure 3.9: A two-stage system to produce a highly concentrated permeate stream (Baker, 2012).

In a two-stage membrane design, the permeate from the first membrane unit is recompressed and fed into a second membrane unit, where an additional separation step further enriches the target component. As a result, the final permeate stream achieves a higher concentration of the desired gas. In the most efficient two-stage configurations, the residue stream from the second stage is reduced to a concentration like that of the original feed gas and is typically recycled by mixing it with the initial feed stream. This approach enhances overall separation efficiency while minimizing product losses. In both the multistage separation systems represented in figure 3.8 and 3.9 is present the incorporation of a recycle loop. It can offer significant performance benefits but also introduces additional complexity. One of the main advantages is the improvement in overall recovery, as recycling the retentate or permeate allows further separation of valuable components that would otherwise be lost. This enhances the efficiency of membrane utilization and reduces waste. Moreover, recycle configurations provide greater flexibility in achieving specific purity and recovery targets. They also typically require additional energy input for recompression of recycled streams, leading to higher capital and operating costs. A recycle stream inherently requires the presence of a purge stream, which may result in material losses. Furthermore, the performance gains may exhibit diminishing returns, particularly when approaching the theoretical limits of separation. Thus, the use of recycle loops must be carefully evaluated considering both technical and economic trade-offs (Fan et al., 2024).

Chapter 4

PSA unit design

This chapter introduces the technical work carried out for this thesis. It focuses on the design of the PSA unit which includes the cycle analysis where all the steps will be examined and scheduled in a proper way for the application. Then, a preliminary sizing of the PSA column is performed, looking for the better diameter and length of the packed bed column to carry out the CO₂ capture. To conclude, a dynamic simulation of the adsorption step performed using MATLAB.

4.1 CO₂ capture PSA unit location within the SYPOX process

The stream treated in the PSA unit originates from the tail gas of a preceding PSA system, which is employed for hydrogen recovery in the biogas-to-hydrogen plant developed by SYPOX. The conceptual scheme relative to the addition of the PSA unit for CO₂ capture is shown in figure 4.1.

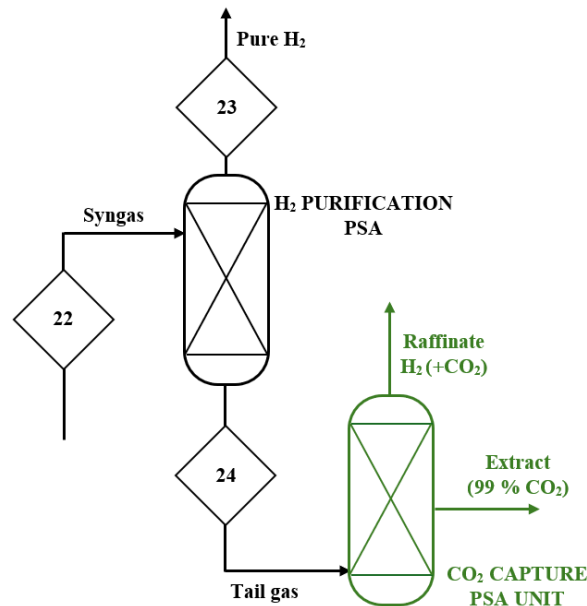


Figure 4.1: BFD with the inclusion of the PSA unit for CO₂ capture.

It was selected to apply the capture in the tail gas stream because it is at atmospheric pressure. Usually, CO₂ capture with PSA technology implies the usage of a vacuum swing cycle. For that reason, the pressure of the adsorption step does not require high absolute values also because

to avoid large in the swing of pressure and consequent large energy requirements (Liu et al., 2011). The characteristics of tail gas stream are reported in Table 4.1.

Table 4.1: Tail gas stream details and composition.

Stream	24
Description	Tail gas
Temperature [°C]	35
Pressure [bar]	1.03
Molar flow [Kmol/h]	3.88
Mass flow [kg/h]	125.70
Composition [mol/mol]	
	CO₂ 0.70
	CO 0.03
	H₂ 0.26
	H₂O 0.01

The objective is to obtain a carbon dioxide stream with high purity, meeting the specific requirement of achieving in a product stream a 90% CO₂ recovery defined as:

$$Recovery = \frac{Flowrate\ of\ CO_2\ in\ the\ product}{Flowrate\ of\ CO_2\ in\ the\ Feed} \quad (4.1)$$

In the same stream there must be reached also a 0.99 of molar fraction of CO₂ satisfying purity requirements. A key assumption made in this study is that the tail gas stream is composed solely of hydrogen and carbon dioxide. This simplification is justified by the relatively low concentrations of water and carbon monoxide in the tail gas, which are not expected to significantly affect the separation process. Moreover, the adsorption behaviour of CO and H₂O on the selected adsorbent is comparable to that of hydrogen, further supporting the validity of this assumption. Therefore, the mixture is modelled as a binary system, consisting of 70% CO₂—retaining the original concentration to ensure the same adsorption load—and 30% H₂. A second important assumption made to simplify the operations is that the mixture is assumed to be ideal. To verify the validity of that assumption, a study to assess its feasibility has been conducted and it has been compared with two other thermodynamic model: the Peng Robinson and the Soave Redlick Kwong. The mass density data were obtained using Aspen Plus by conducting two separate sensitivity analyses. In the first analysis, the pressure was held constant at the feed pressure (1.03 bar), while the temperature was varied in the range of 20°C to 60°C. In the second analysis, the temperature was fixed at the operating value of the feed stream (35°C), and the pressure was varied from 0.01 to 2 bar. To understand the deviation from ideal gas assumption, the compressibility factor for each of the model is then calculated:

$$Z = \frac{PV}{nRT} = \frac{P MW_{mix}}{\rho_{mix} RT} \quad (4.2)$$

For each analysis the corresponding plot is retrieved. Both graphs show that the two models deviate only slightly from the ideal gas assumption, which is represented by the yellow line corresponding to $Z = 1$.

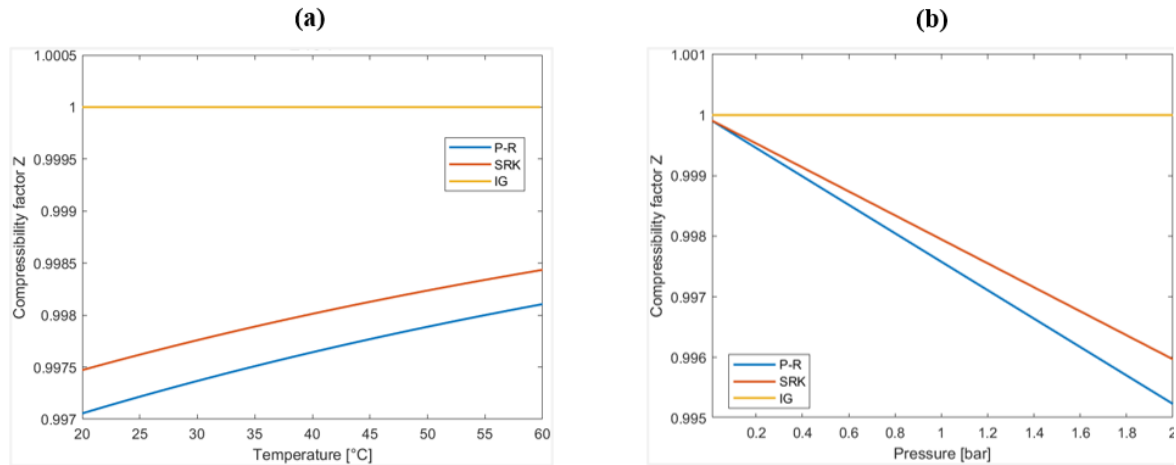


Figure 4.2: Compressibility factor of the binary mixture hydrogen-carbon dioxide for Peng-Robinson and Soave-Redlick-Kwong. (a) temperature varies. (b) pressure changes.

Following those two assumptions a macroscopic material balance, can be performed also considering the requirements of purity and recovery pre-established. The PSA unit can be considered as a single block which has reached a cyclic steady state (figure 4.3). In CO_2/H_2 separation the carbon dioxide is generally the most strongly adsorbed component for a wide range of adsorbent materials. For this reason, the target stream that meets the specified requirements is the extract product stream, obtained after a vacuum desorption step following the adsorption of CO_2 at feed temperature, as will be discussed in the next paragraph. The raffinate stream, on the other hand, is primarily composed of hydrogen. To further purify and recover this hydrogen, the raffinate can be recycled. After recompression, it can be mixed with Stream 22 (see Figure 1.15), thereby increasing the hydrogen recovery and decreasing the hydrogen production cost.

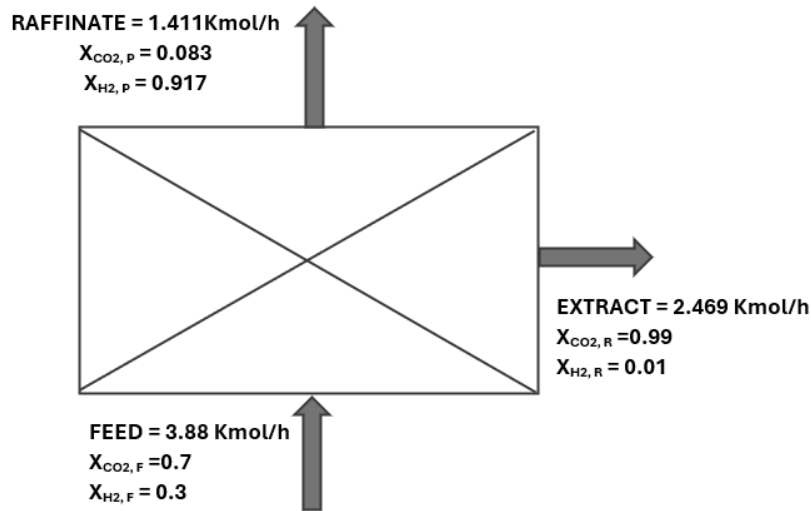


Figure 4.3: Macroscopic material balance performed over the entire PSA unit.

This balance serves as a starting point for the sizing of adsorption columns as it can be understood, after the choice of the adsorption time, the amount of moles that must be removed from the feed stream.

4.2 Design of the PSA cycle

This section outlines the scheduling of the PSA process cycle and provides the rationale behind the selection of each step. It is important to note that the design presented is not based on experimental data. Rather, the objective is to develop a cycle that is both realistic for the intended operation and suitable as a foundation for the subsequent sizing of the columns involved in the process.

4.2.1 Adsorption step time

The first and most critical decision in properly scheduling a PSA cycle is setting the duration of the adsorption step. Determining the appropriate adsorption time is essential to ensure efficient and effective gas separation. It enables optimal utilization of the adsorbent, preventing both underuse and premature saturation that could lead to impurity breakthrough. A well-chosen adsorption time also ensures high product purity and recovery by minimizing losses and avoiding contamination. Moreover, this choice directly influences the overall cycle balance, as the durations of the subsequent steps are closely linked to the adsorption time. An accurate assessment prevents process inefficiencies and reduces energy consumption by avoiding excessively long steps. In summary, selecting the correct adsorption time is key to maximizing performance, purity, and energy efficiency in PSA systems. Similar works concerning a CO₂ capture from a stream containing hydrogen have been analysed to understand which could be an optimal adsorption time for this work (Subraveti et al., 2021; Liu et al., 2020; Khurana & Farooq, 2019; Susarla et al., 2015; Ho et al., 2008). It is important to note that the works

referenced refer to studies involving larger-scale plants, where the treated streams contain significantly greater quantities of material compared to those considered in this thesis. Nevertheless, they provide a solid foundation for selecting an appropriate adsorption step time, as the type of separation involved treats flue gases and it is then similar in terms of temperature pressure, composition and adsorbent material used. The selected adsorption time is then selected as the same of the article of Subraveti et. al. (2021), which has applied the carbon capture to a flue gas stream which similar CO₂ composition to the one of this thesis work and has retrieved the optimal time for each step of the cycle by performing an optimization on more process variables using Aspen adsorption. This time is $t_{ads} = 300$ s.

4.2.2 Steps of the cycle

Nearly all PSA processes involving carbon dioxide adsorption employ vacuum extraction for column regeneration. This approach is primarily motivated by the strong interactions between CO₂ and various adsorbents, owing to the polar nature of the gas. For example, when using zeolite as the adsorbent, significant amounts of CO₂ are retained even at atmospheric pressure. To weaken these interactions and effectively reduce the adsorbed loading, it is necessary to achieve a high degree of vacuum. Thus, a VSA cycle, based on the Air Liquide model (see section 2.3.4) is selected. Each column of the unit undergoes five distinct steps to complete one full cycle. These steps are analysed for a single column as follows:

1. Adsorption step: The cycle begins with the introduction of the feed stream into the packed bed. Due to the preferential adsorption of CO₂ over hydrogen, a purified hydrogen-rich raffinate stream is obtained.
2. Pressure equalization, depressurization: Once the adsorption step is ended, the column is got in contact with another bed that has just finished a vacuum extraction step. The raffinate coming from the previous step is expanded co-currently in the second column causing an increase in the fraction of adsorbed CO₂. The pressures of the two columns are then equalized to an intermediate pressure.
3. Vacuum extraction: The column almost full of adsorbed carbon dioxide is disconnected from the second column and is get in contact with a vacuum pump. Sub atmospheric pressure is then achieved inside the bed to a level equal to 0.05 bar and a flowrate of extract stream at vacuum pressure is obtained.
4. Pressure equalization, pressurization: Once the vacuum step ends, the adsorbent is completely regenerated from the CO₂. The column has a large grade of vacuum which can be exploited to equalize another column of the unit which needs its internal pressure to be reduced while it is going to face a vacuum extraction step.

5. Re-pressurization: The connection with the other column is closed. The feed enters the column but is not delivered as a raffinate since the product end valve is closed. This step ends when the column reaches the same pressure of the feed and can then start another adsorption step.

The five steps for a single column are schematized in figure 4.4.

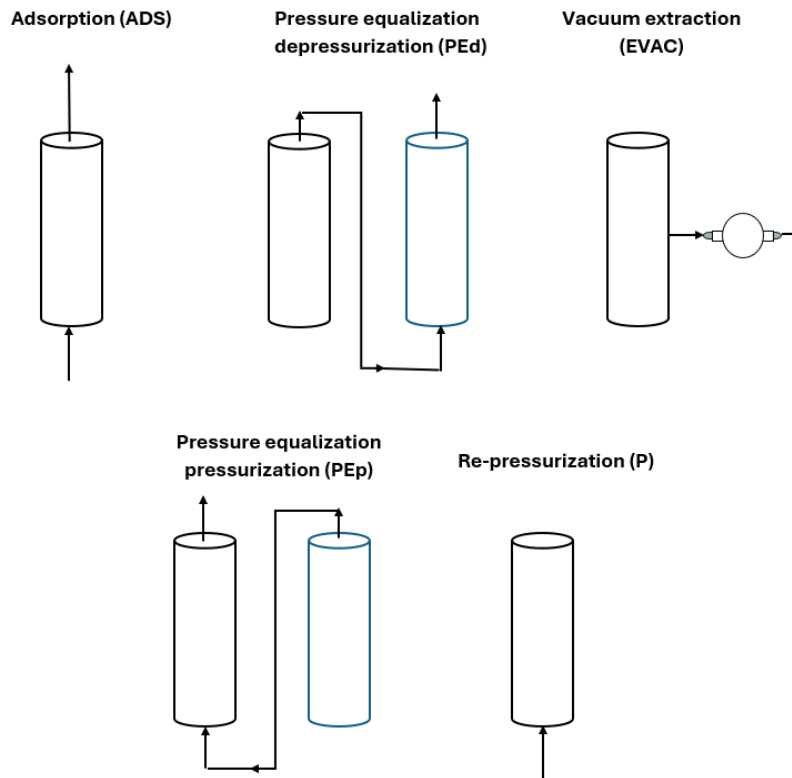


Figure 4.4: The five steps of the PSA unit cycle used for the CO₂ capture. The black column is the one which the described steps refer to. The blue column is used for illustrative purposes to represent the equalization steps.

Alternative cycle design choices could have been adopted, such as those proposed by Gholami et al. Also in their configuration, a depressurization step precedes the vacuum extraction phase at the end of adsorption. The key difference lies in the fact that the columns are not connected through pressure equalization; instead, each column is individually connected to a blowdown pump that reduces the internal pressure. This causes a co-current expansion of the column's fluid content, while a significant amount of the adsorbed phase remains within the bed. In the present work, however, a pressure equalization step was preferred. This choice is primarily motivated by the minimal amount of material that needs to be transferred after the adsorption phase. Implementing blowdown pumps in this context would increase capital costs without offering substantial improvements in process efficiency. Furthermore, the pressure equalization avoids any other creation of further stream that should be either vented or in atmosphere or recompressed and recycled to the PSA unit for hydrogen recovery further increasing operative costs.

4.2.3 Cycle scheduling

To properly schedule the cycle of a PSA unit, it is essential to determine the number of columns required to complete the process. The system must operate in such a way that both the raffinate and extract streams are delivered continuously. To meet this condition, at any given moment, at least one column must be in the adsorption phase while another is undergoing vacuum extraction. Therefore, before calculating the number of columns needed, the duration of each of the five process steps must be defined. The time of each step is chosen consulting the works cited in section 4.1.1 and scaling these times based on the adsorption time.

Table 4.2: Time of each single step.

<i>Step</i>	<i>Time [s]</i>
<i>Adsorption</i>	300
<i>Pressure equalization</i>	100
<i>Vacuum evacuation</i>	1000
<i>Re-pressurization</i>	50

The pressure equalization step must be accounted for twice in the total cycle time calculation: once when it is adopted for the depressurization of the column and once during its pressurization whose follow the vacuum step. Once the duration of each step has been defined, the number of columns required for continuous operation N can be determined. This is done by taking the ratio of the total cycle time—obtained as the sum of all individual step durations—to the adsorption time and rounding the result up to the nearest whole number.

$$N = \text{ceiling} \left(\frac{\sum_{i=\text{steps}} t_i}{t_{ADS}} \right) \quad (4.3)$$

Where t_{ADS} is the adsorption step time and i defines each step. The result obtained from this calculation indicates that five columns are necessary to carry out the operations.

With the same principle also the number of vacuum pumps N_v needed to maintain a continuous vacuum extraction can be calculated starting from the ratio between the vacuum extraction step and the adsorption step time and by rounding up also that ratio it is found that four vacuum pumps are needed

$$N_v = \text{ceiling} \left(\frac{t_{EVAC}}{t_{ADS}} \right) \quad (4.4)$$

In some cases, the scheduling of PSA cycle steps may result in a total cycle time that is not an exact multiple of the adsorption time. To address this, an idle step is introduced following the evacuation phase. This additional step helps minimize disturbances to the bed profiles and ensures that the cycle can be completed in a synchronized manner across all columns (Subraveti et al., 2021). In that case the times of the steps are chosen in a way to be the total cycle time a multiple of the adsorption time. The complete organization of the cycle and the relative steps are shown in figure 4.5.

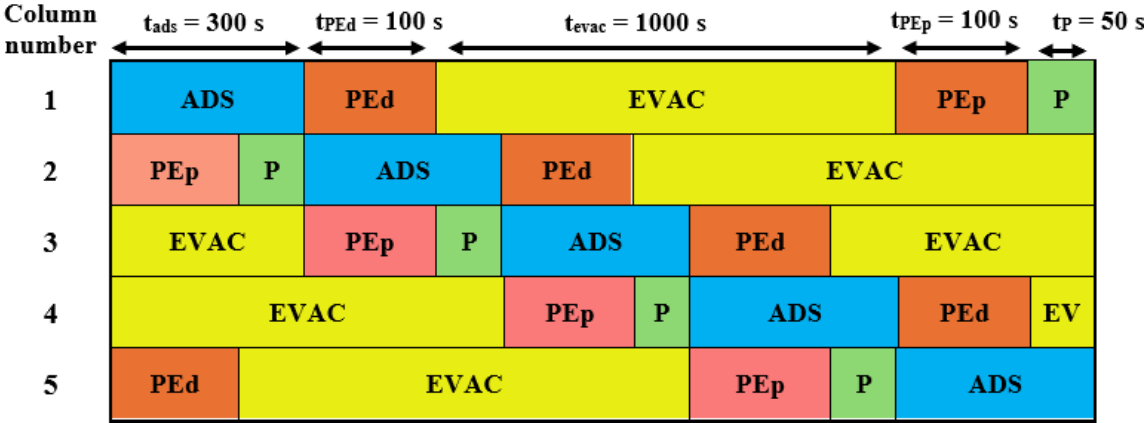


Figure 4.5: Cycle scheduling of the 5-steps for the five PSA columns.

The pressure change trend along the time for the first column is also represented in figure 4.6 highlighting each step.

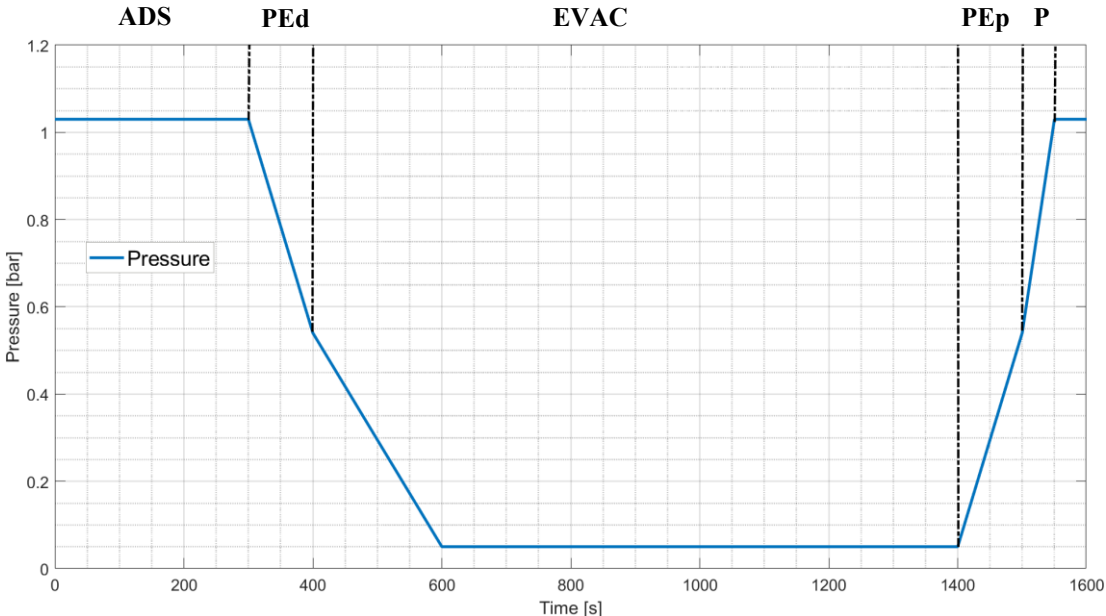


Figure 4.6: Pressure change over the cycle step for the first column. Each step is delimited by the dotted lines.

The image denotes the various pressure level that must be reached during a cycle of the selected process. The final PFD of the PSA process is shown in figure 4.7:

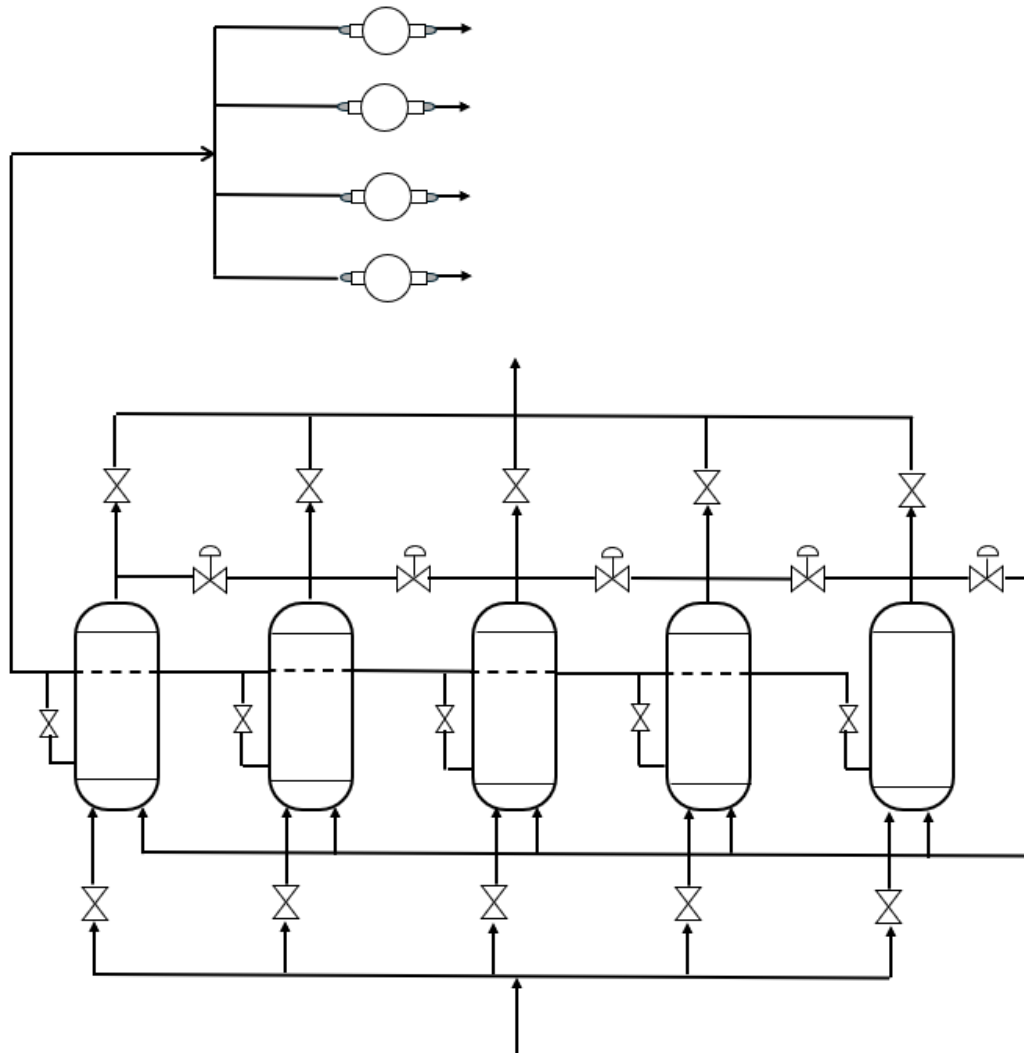


Figure 4.7: PFD of the five-columns CO_2 capture PSA process.

In addition to the columns and vacuum pumps, the PFD also shows the control and switching valves necessary to regulate the cycle.

4.3 Column sizing

The material balance illustrated in Figure 4.3 serves as the foundation for sizing a single adsorption column. The sizing is based on the quantity of adsorbent material required for the process. This amount is determined by considering the duration of the adsorption step and the total molar flow rate of the species to be adsorbed during this phase, prior to the sequent vacuum extraction. It is important to emphasize that the literature lacks a definitive and universally accepted procedure for the sizing of adsorption columns, and this is even more pronounced in the case of PSA systems. The design presented in the following chapter is the result of a synthesis of information drawn from reference textbooks (Perry, 2018), general design guidelines (Knaebel, 1992), and selected research articles on the subject (Ali Abd et al., 2023).

4.3.1 Adsorbent material selection

The selection of an appropriate adsorbent is fundamental in the design of the PSA systems since the isotherm data are necessary to understand the capacity of the material and consequently the amount of material needed. In processes aimed at purifying hydrogen by removing carbon dioxide, zeolite 13X emerges as one of the most effective and industrially reliable materials (Park et al., 2016), combining high selectivity, adsorption capacity, and operational stability. Zeolite 13X is a synthetic aluminosilicate with relatively large pore openings (~ 10 Å), is particularly well-suited for CO₂ capture. This material exhibits a strong electrostatic field due to the presence of exchangeable Na⁺ cations, which enhances its interaction with polarizable molecules like carbon dioxide. In contrast, hydrogen, being a non-polar and very small molecule, is only weakly adsorbed by the zeolite framework. This sharp contrast in adsorption behaviour results in excellent selectivity toward CO₂, allowing hydrogen to pass through the adsorbent bed with minimal retention. Moreover, zeolite 13X offers a high adsorption capacity for CO₂ at low to moderate pressures, which is critical for the efficiency of the considered PSA operation since the feed pressure is atmospheric. Another critical advantage of zeolite 13X is that it can be simply regenerated. Unlike materials that require thermal regeneration, zeolite 13X can be effectively regenerated through simple depressurization, which is the basis of PSA technology. Additionally, the material shows strong mechanical stability and resistance to thermal degradation, tolerating temperatures up to approximately 600 °C, which ensures its robustness over extended operation and many PSA cycles (Cavenati et al., 2004). In comparison, other materials such as activated carbons and metal-organic frameworks (MOFs) present important limitations. Activated carbons are more tolerant to moisture and are widely available at a lower cost. However, their interaction with CO₂ is governed mainly by physisorption with relatively weak forces, resulting in lower selectivity and capacity. The system may then require more cycles or larger volumes of material to achieve equivalent performance. On the other hand, MOFs offer outstanding potential due to their highly tuneable structure and, in some cases, superior CO₂ selectivity. However, their practical application is still limited by high production costs, poor mechanical stability, and a general sensitivity to moisture, which leads to rapid degradation of performance unless strict gas conditioning is applied (Kumar et al., 2015). Ultimately, zeolite 13X presents the best trade-off among performance, cost, availability, and industrial maturity. It is already used commercially in PSA units for CO₂ capture, especially in VSA cycle, making it a highly reliable choice for CO₂/H₂ separation. Many studies have been performed regarding the adsorption equilibria and of zeolite materials for specific components within a target effluent gas. In the study by Park et al. (2016), the adsorption equilibria of six pure components—including CO₂ and H₂—on pelletized zeolite 13X were measured using the volumetric method. The adsorption behaviour of each component was analysed by considering their partial pressures within various effluent mixtures, with

measurements conducted up to 1000 kPa at temperatures of 293, 308, 315 and 323 K. The experimental adsorption isotherms were then correlated using the Langmuir, Sips, and temperature-dependent Sips models. Because of its simplicity the Langmuir model is selected to calculate the equilibrium behaviour of zeolite 13X. The isotherm trends were subsequently obtained by implementing the model parameters reported in the reference article and plotting the resulting curves using MATLAB.

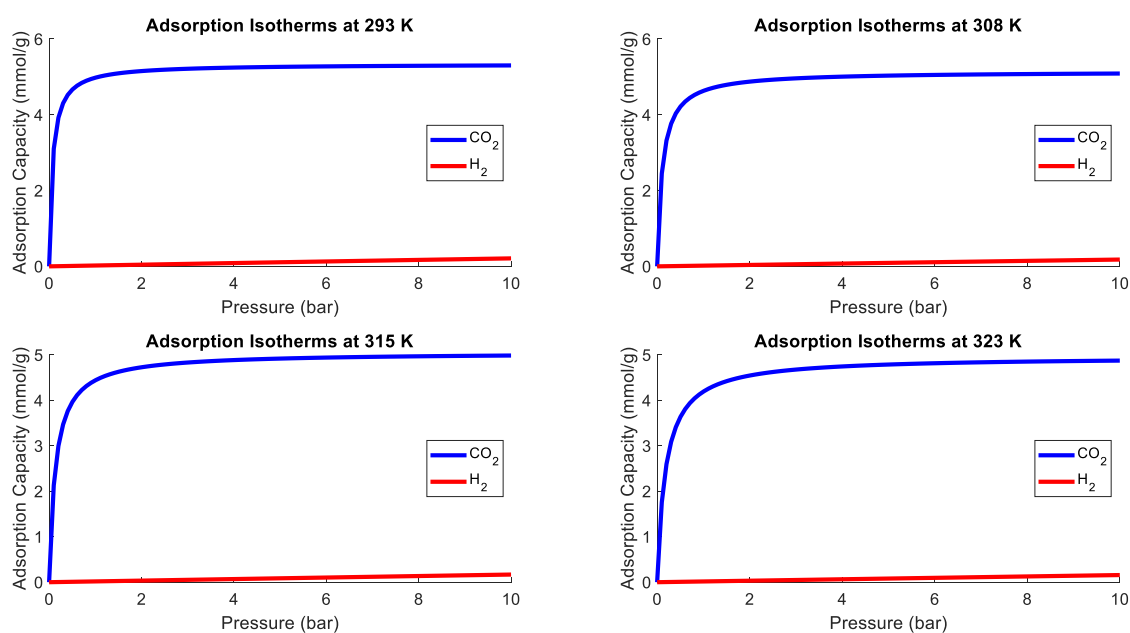


Figure 4.8: Langmuir isotherm for CO₂ and H₂ in zeolite 13X at four different temperatures.

As expected, the equilibrium loading decreases with increasing temperature, even if with limited magnitude. Nevertheless, the decrease does not overcome more than some decimal of mmol/g of loading. This result supports the assumption that will be made in the column sizing to consider the process as isothermal. The isotherm of carbon dioxide clearly corresponds to a Type I isotherm and at all investigated temperatures, a steep increase in adsorption capacity is observed starting from vacuum pressure. Once atmospheric pressure is reached, the loading curve starts to curve and then remains essentially constant, even with substantial increases in pressure. In contrast, hydrogen exhibits a linear adsorption trend on zeolite 13X across the entire pressure range. These trends highlight the significant difference in adsorption behaviour of the two components on this adsorbent. Moreover, they confirm the necessity of operating under vacuum conditions to reduce the strong interactions between CO₂ and zeolite 13X, thereby enabling effective column regeneration and purification. On table 4.3 are reported a range of materials over a CO₂ capture can be carried out.

Table 4.3: Adsorbent materials comparison in terms of CO₂ capacity, thermal stability and cost.

<i>Adsorbent material</i>	<i>CO₂ capacity (mmol/g)</i>	<i>Thermal stability</i>	<i>Cost</i>	<i>Reference</i>
<i>Zeolite 13X</i>	High (~4–6)	Good (up to ~550°C)	Moderate	Park et al. (2016)
<i>Zeolite 5A</i>	Moderate (~2–4)	Good	Moderate	Choi et al. (2009)
<i>Activated carbon</i>	Moderate (~2–4)	Excellent (>600°C)	Low	Wang et al., (2011)
<i>Carbon molecular sieve (CMS)</i>	Moderate (~3–4.5)	Excellent	Low	Siriwardane et al., (2001)
<i>MOFs</i>	1262	Often Poor (unstable)	High	Li et al., (2011)

The table gives a rapid comparison with different types of adsorbent highlighting how the zeolite 13X gives the best compromise between the parameters considered.

4.3.2 Column design steps

Before to start with the design steps, is important to retrieve some data concerning the adsorbent material and the flowing gas mixture. Starting from the adsorbent, it is important to understand the size of the particle diameters, the solid particle density and the sphericity. These data are obtained from the article of Park et al. (2016) and from the one of Subraveti et al. (2020). Concerning the feed gas mixture the volumetric flowrate is estimated with the ideal gas law, starting from the molar flow rate, and mass density is obtained via Aspen Plus. It is then to be choice the porosity of the bed, typical values for packed bed stays around 0,35 and 0,45. It is assumed here a porosity of 0,4. A clarification must be then made regarding the evaluation of fluid velocity. In processes involving fixed-bed units, it is common practice to assume an average velocity for the fluid flowing through the column. This assumption is generally justified by the fact that many of these processes operate under steady-state conditions, where flow characteristics remain constant over time (Schmidt, 2005). In gas solid adsorption separation processes, a portion of the feed is adsorbed along the column and the fluid velocity would, in principle, vary with time and along the length of the bed. The volumetric flow rate indeed diminishes of the 60% along the column. However, for simplification, the velocity is assumed to remain constant and equal to the feed velocity. Although this assumption is not strictly accurate, it leads to an overestimation of the pressure drop rather than an underestimation, thereby enabling a conservative design of the adsorption column.

The first step in column sizing is to determine the bed diameter, which is dependent on the chosen superficial velocity. If the diameter is too large, undesirable phenomena such as channelling—a phenomenon where the fluid flows preferentially through certain paths or "channels," bypassing other areas of the bed, leading to poor contact between the fluid and the

adsorbent—may occur within the packed bed. Conversely, a diameter that is too small can result in excessive pressure drops, potentially damaging the adsorbent material. The pressure drops across the bed is typically estimated using a modified form of the Ergun equation (eq. 2.15), which relates pressure drop to superficial velocity, particle size, bed porosity, and fluid properties. In this study, the maximum allowable pressure drop is assumed to be 0.07 bar/m. However, the total pressure drop must be verified after defining the bed height; as a rule of thumb, it is generally recommended that the overall pressure drop per unit length does not exceed approximately 0.55 bar (Gas Processors Suppliers Association, 2004). Once the maximum allowable superficial velocity is determined, it is used to calculate the minimum required cross-sectional area of the bed A_{min} . This is done by dividing the volumetric flow rate \dot{Q}_{feed} by the calculated maximum velocity $v_{s,max}$.

$$A_{min} = \frac{\dot{Q}_{feed}}{v_{s,max}} \quad (4.5)$$

The minimum diameter is then simply calculated as the cross-section area of the column is circular:

$$D_{min} = \sqrt{\frac{A_{min} * 4}{\pi}} \quad (4.6)$$

The minimum diameter obtained serves as a reference for the subsequent design step, which involves selecting the appropriate column diameter. Diameters smaller than this value cannot be considered, as they would result in higher superficial velocities than the established limit, consequently leading to excessive pressure drops within the column. In table 4.4 are reported the values obtained from the calculation of the parameters involved in this first step and the features of the adsorbent and of the gas mixture.

Table 4.4: Parameters and results retrieved by pressure drops calculation.

Parameter	Unit	Value
Zeolite 13X		
Solid density	kg/m ³	1130
Particle diameter	mm	1,6
Sphericity	-	0,9
Feed gas		
Vol. Flowrate	m ³ /s	0,027
Max. velocity	m/s	0,393
Mass density	kg/ m ³	12,024
Viscosity	Pa*s	1,596e-5
Column		
Max. Pressure drops	bar/m	0,07
Bed porosity	-	0,4
Minimum area	m ²	0,068
Minimum diameter	m	0,295

The second step concerns the calculation of the total volume of adsorbent required to pack the fixed bed. This begins with an estimation of the mass of adsorbent needed to capture the moles of CO₂ within the column. To obtain this value, two key parameters are required: the equilibrium loading of CO₂ on the adsorbent and the total number of moles to be adsorbed during the adsorption step. The equilibrium loading can be calculated using isotherm data derived from the Langmuir model. At the feed pressure, zeolite 13X can adsorb a specific amount of CO₂ $q_{CO_2,f}$ (mol/kg_{adsorbent}), which will vary as the pressure decreases following the adsorption step. The total moles of CO₂ to be adsorbed $n_{CO_2,ads}$ (mol) can be calculated directly by multiplying the duration of the adsorption step t_{ads} by the molar flow rate of CO₂ to be adsorbed during the adsorption phase to meet the process requirements $\dot{Q}_{CO_2,ads}$. This value is obtained from the overall balance (fig. 4.2)

$$n_{CO_2,ads} = t_{ads} * \dot{Q}_{CO_2,ads} \quad (4.7)$$

The mass of the adsorbent is simply calculated by performing the ratio between the loading and the total moles to be adsorbed.

$$m_{ads} = \frac{n_{CO_2,ads}}{q_{CO_2,f}} \quad (4.8)$$

To determine the total volume of the packed bed, the required mass of adsorbent is divided by its bulk density. This density accounts for both the internal porosity of the adsorbent particles and the interstitial voids between them in the packed bed. As such, the bulk density reflects the overall packing characteristics of the bed and is calculated as shown in Equation 2.19. The bed volume is thus obtained as follows:

$$V_{bed} = \frac{m_{ads}}{\rho_b} = \frac{m_{ads}}{\rho_s * (1 - \varepsilon)} \quad (4.9)$$

This relationship holds for any favourable isotherm under the assumptions of isothermal plug flow and constant fluid velocity (Knaebel, 1992). The volume of the adsorbent bed V_{bed} is also given by the product of the column length and its cross-sectional area, i.e., $V_{bed} = L * A$.

The third and last step of the sizing starts with a design choice. The minimum diameter obtained in step one serves indeed as a starting point to select the proper diameter of the bed that must be greater than or equal to this value. It follows that the resulting cross section area must be evaluated:

$$A = \frac{\pi}{4} D_{sel}^2 \quad (4.10)$$

And the length of the column is finally calculated by dividing the volume of the bed found in the previous step with the cross-section area:

$$L = \frac{V_{bed}}{A_{sel}} \quad (4.11)$$

It must be ensured a proper ratio between the length and the diameter of the column. Typical values of the PSA length-to-diameter ratio (aspect ratio) range between 2 and 5 (Ruthven, 1994). In this study, a ratio of 3 is selected. To determine the corresponding column diameter that satisfies this criterion, a range of 200 diameters—from D_{min} and $2D_{min}$ —is evaluated. This analysis is performed using MATLAB, where all necessary calculations are implemented. The resulting relationship between the L/D_{sel} ratio and the selected diameters is illustrated in Figure 4.9.

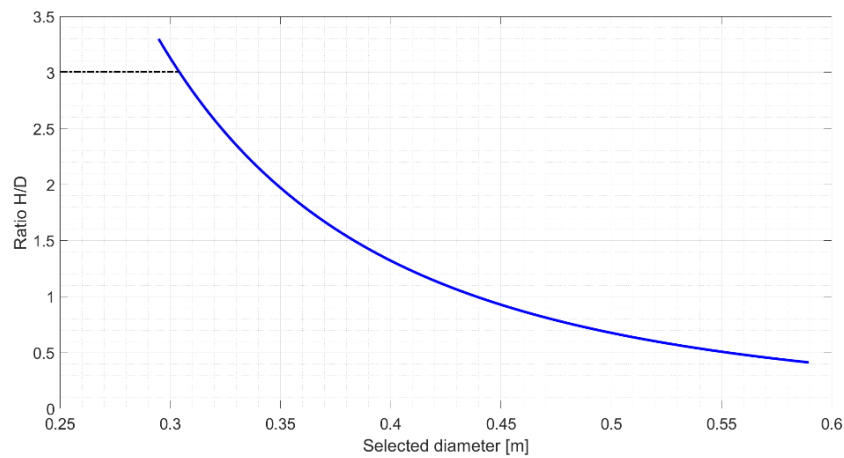


Figure 4.9: Length-to-diameter ratio over the range of possible diameter to choose. The dotted line intersects the diameter to select to obtain a ratio of 3.

It is important to specify how in the evaluation of the length only equilibrium effects are considered. To include also kinetic effects, a dynamic non-steady-state balance must be considered. In gas solid adsorption systems, a mass transfer zone (MTZ) reflecting the occurring of the adsorption process must be accounted. In this zone, the concentration of the adsorbate component drops from its inlet value to nearly zero. Furthermore, at breakthrough point, the adsorbate begins to appear at the outlet even though part of the bed—typically near the exit—still has unused capacity. Therefore, a part of bed unused (LUB i.e., length of unused bed) must be accounted for when sizing the column to ensure that the required outlet purity is maintained and to prevent premature breakthrough. Ignoring the LUB would lead to underestimating the required bed length and compromising process efficiency (Kohl & Nielsen, 1997). These two factors will be considered in the next section.

Table 4.5: Results of step 2 (volume calculation) and 3 (equilibrium length calculation).

Parameter	Unit	Value
Step 2		
Adsorption step time	s	300
Flowrate of CO ₂ to adsorb	kmol/h	2.44
Moles of CO ₂ to adsorb	mol	203.67
Loading of CO ₂ at feed pressure	mol/kg _{ads}	4.64
Adsorbent mass needed	kg _{ads}	45
Bulk density	kg _{ads} /m ³	678
Bed volume	m ³	0.07
Step 3		
Selected diameter	m	0.31
Equilibrium length	m	0.92
Ratio L/D	-	3
Adjusted velocity	m/s	0.37
Adjusted pressure drops	bar/m	0.06
Total pressure drops	bar/m	0.06

After the proper diameter has been selected, the adjusted velocity which derives from the diameter is calculated to get which will be the superficial feed velocity:

$$v_{s,adj} = v_{s,max} \left(\frac{D_{min}}{D_{sel}} \right)^2 \quad (4.12)$$

And consequently, also the pressure drops across the column can be retrieved:

$$\left(\frac{\Delta P}{L} \right)_{adj} = \left(\frac{\Delta P}{L} \right)_{max} \left(\frac{v_{s,adj}}{v_{s,max}} \right)^2 \quad (4.13)$$

To conclude this section the overall pressure drops over the column are calculated by multiplying the adjusted pressure drops value by the equilibrium length. This number is well above the limit of pressure drops in packed columns previously described. Table 4.5 shows the results of the calculations performed in step 2 and 3.

4.4 Dynamic simulation of the adsorption step

The sizing of the column performed in the previous section accounts only for equilibrium. To provide in a most accurate way the dimension of the length of the adsorption column also kinetic effects must be considered. The material balance for a single species represented in equation 2.19 is the starting point of this discussion. Some assumptions will be added to the ones made in the previous discussion to simplify the development and resolution of the balance. A plug flow model is then considered for the fixed bed neglecting axial dispersion. A simulation of the adsorption step is going to help to understand the final size of the column. The balance can then be expressed in molar fraction terms, (y_i) and since in the adsorption step the pressure does not undergo step changes, it is assumed constant. The balance has then this form:

$$\frac{\partial y_i}{\partial t} + \frac{v_s}{\varepsilon} \frac{\partial y_i}{\partial z} + \frac{RT}{P} \left(\frac{1 - \varepsilon}{\varepsilon} \right) \rho_s \frac{\partial q_i}{\partial t} = 0 \quad (4.14)$$

As the extent of hydrogen adsorbed is minimal compared to the one of carbon dioxide, it is assumed that only carbon dioxide is retained by the zeolite 13X. This assumption will have minimal impact on the overall balance, as the amount of hydrogen adsorbed is significantly smaller than that of CO₂ as can be seen in the isotherm in figure 4.6; consequently, the adsorption term ($\partial q_i/\partial t$) would exhibit only negligible variation.

4.4.1 Mass transfer

In a gas-solid separation process within a packed-bed adsorption column, mass transfer refers to the movement of adsorbate molecules from the fluid phase to the solid adsorbed phase. The efficiency of this mass transfer strongly influences the overall performance of the separation. If the transfer is slow, the adsorption process is delayed, leading to a broader concentration front, premature breakthrough, and underutilization of the adsorbent. As a result, a longer bed is required to achieve the desired separation. The mass transfer rate is described with a LDF model as shown in equation 2.19. The mass transfer coefficient k_i is assumed as constant and can be written as the product of the specific surface a and the interfacial mass transfer coefficient $h_{m,i}$. The specific surface quantifies the available surface for adsorption per unit volume of the adsorbent. It influences the rate of adsorption since the higher the specific surface the faster will be the mass transfer and so the adsorption. This quantity can be written as a function of the particle diameter of the adsorbent:

$$a = \frac{6}{D_p(1 - \varepsilon)} \quad (4.15)$$

Regarding the interfacial mass transfer coefficient, the ones of the CO₂ from the gas to the adsorbed phase must be calculated. It can be derived thanks to the Chilton-Colburn analogy. This tool links mass transfer to momentum and heat transfer, allowing to use correlations developed for one type of transport to predict another. Extensive data on forced convection for the flow of gases and liquids through shallow packed beds have been critically analysed (Williamson et al., 1963), leading to the development of the following local heat transfer correlation:

$$j_h = 2,19 Re^{-2/3} + 0,78Re^{-0,381} \quad (4.16)$$

An identical formula for the mass transfer function j_d , is defined thanks to the Chilton-Colburn analogy:

$$j_h = j_d \quad (4.17)$$

The analogy has proven to be effective for describing transverse flow around cylinders as well as flow through packed beds. The Chilton-Colburn factor can be described with a combination of dimensionless number as

$$j_d = \frac{Sh}{Re Sc^{1/3}} \quad (4.18)$$

Where Re is the Reynolds number, the ratio of inertial forces to viscous forces in a flowing fluid and indicates whether flow is laminar or turbulent. Sh is the Sherwood number representing the ratio of convective and diffusive mass transfer. Sc is the Schmidt number and is the ratio of momentum diffusivity to mass diffusivity. They are described by the following equations:

$$Re = \frac{\rho_g * \bar{v}_s * D_p}{\mu} \quad (4.19)$$

$$Sc_{CO_2} = \frac{\mu}{\rho_g * D_{CO_2,mix}} \quad (4.20)$$

$$Sh_{CO_2} = \frac{h_{m,CO_2} * D_p}{D_{CO_2,mix}} \quad (4.21)$$

$D_{CO_2,mix}$ represents the molecular diffusivity of CO₂ in the fluid mixture, this value is retrieved via Aspen Plus. Finally, the mass transfer coefficient for the CO₂ is (Bird et al., 2002):

$$h_{m,CO_2} = \frac{j_d}{(Sc_{CO_2})^{2/3}} \bar{v}_s \quad (4.22)$$

The parameters of the gas are assumed constant along the column even if the adsorption process leads to a change in the composition of the mixture and consequently of those properties.

Table 4.6: Results for the calculation of the mass transfer coefficient

Parameter	Unit	Value
Particle diameter (D_p)	m	0.0016
Bed Porosity (ε)	-	0.4
Specific surface (a)	1/m	6250
Gas density (ρ_g)	kg/ m ³	12.02
Viscosity (μ)	Pa s	1.60e-5
Averaged velocity (\bar{v}_s)	m/s	0.25
Reynolds number (Re)	-	301.3
Molecular diffusivity ($D_{CO_2,mix}$)	m ² /s	6.43e-6
Schmidt number (Sc_{CO_2})	-	0.21
Colburn factor (j_d)	-	0.13
Interfacial MT coefficient (k_{m,CO_2})	m/s	9.83e-4
Overall MT coefficient (h_{m,CO_2})	1/s	6.14

These parameters—namely, density, viscosity, and molecular diffusivity—are evaluated based on the composition of the feed stream. This choice is justified by the fact that the mixture that approach a zone of the bed has always the initial composition. Only when the adsorption process is ended the mixture change its composition. All the values to calculate the dimensionless numbers and the mass transfer coefficient are reported in the table 4.6.

With the calculation of the mass transfer coefficient, all the elements necessary to perform a simulation are obtained. The objective is to obtain a breakthrough curve that shows the length of the mass transfer zone and thus the length to add to the equilibrium length to have a correct dimension of the adsorption bed. A first simulation is performed using the function *pdepe* on MATLAB[®] to solve the material balance which is a partial differential equation in time and space. On this first simulation the isotherm assumption is carried forward.

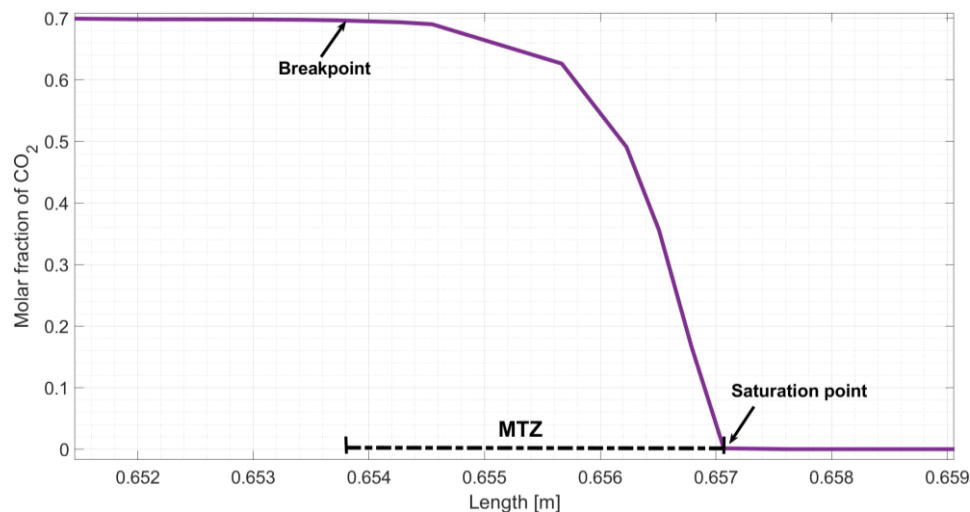


Figure 4.10: *The fracture curve and the manner of mass transfer zone length.*

In figure 4.10 a picture of a length-based breakthrough curve is shown. The curve describes the behaviour of the CO₂ molar fraction in the fluid phase for a fixed time over the adsorption bed. In the first part of the plot the molar fraction of the carbon dioxide is constant at 0.7. At a certain point, it is reached a zone in the bed in which the adsorbent is free from adsorbed material and can start to retain the carbon dioxide present in the gas, this point is called the break point. The amount of CO₂ in the gas phase starts to diminish with a certain shape that is the one of the breakthrough curves of the figure, until the saturation the adsorbent is reached. From that position, at the specific analysed time, all the amount adsorbable of carbon dioxide has been retained. This point is called the saturation point. The area between the break point and the saturation point is called the mass transfer zone and it is the length to be added to the equilibrium one. This zone is negligible compared to equilibrium height measuring some millimetre because of a high value of the mass transfer coefficient. This means that a fast transfer between the two phases occur and so a little resistance is due to this phenomenon.

4.4.2 Length of unused bed

In the design described in section 4.2.2, it is considered the length necessary to consider the effect due to thermodynamic effect. In the previous paragraph also kinetic effects due to the mass transfer were considered. Furthermore, in sizing a column, there must be account for a portion of the column that remains unsaturated at the time of breakthrough. Looking at figure 4.11 are shown the length-based breakthrough curves at six moments of the adsorption step. At the last seconds of the adsorption step the break point is not reached.

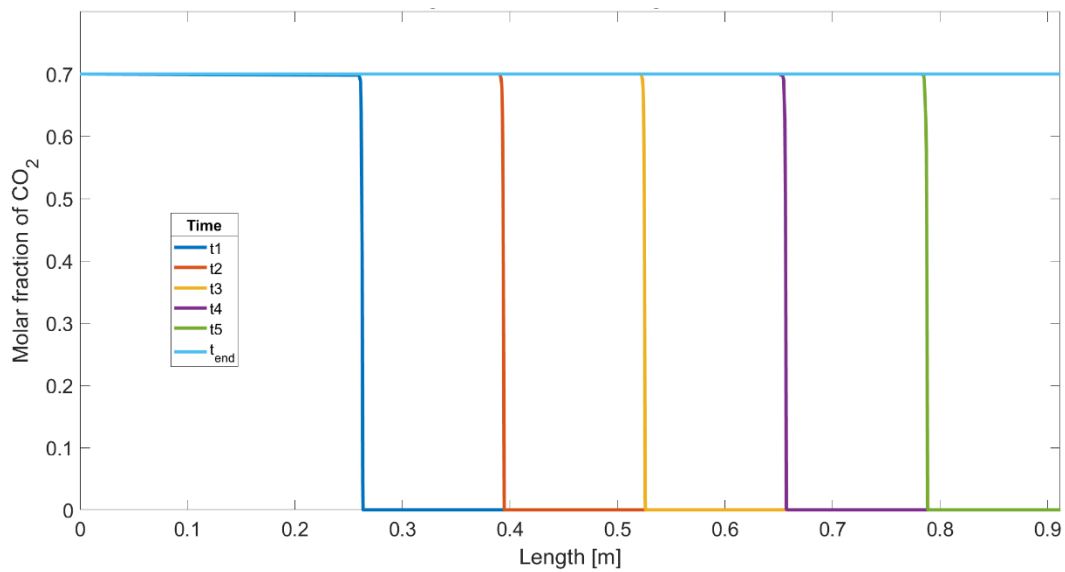


Figure 4.11: Length-based breakthrough curves with the length of the column equal to the equilibrium one. The curves are parametrized for six different fixed time of the adsorption step; the last one is the final instant of the step.

The meaning is that there must be added a portion of the bed to avoid the completely saturation of the adsorbent during the adsorption step. It can be confirmed also by the time-based breakthrough curves in figure 4.12 where five different point of the bed are examined over the

adsorption step. Even in the last examined point, which is the closest to the bed outlet, the molar fraction of CO₂ increases showing the achievement of the saturation.

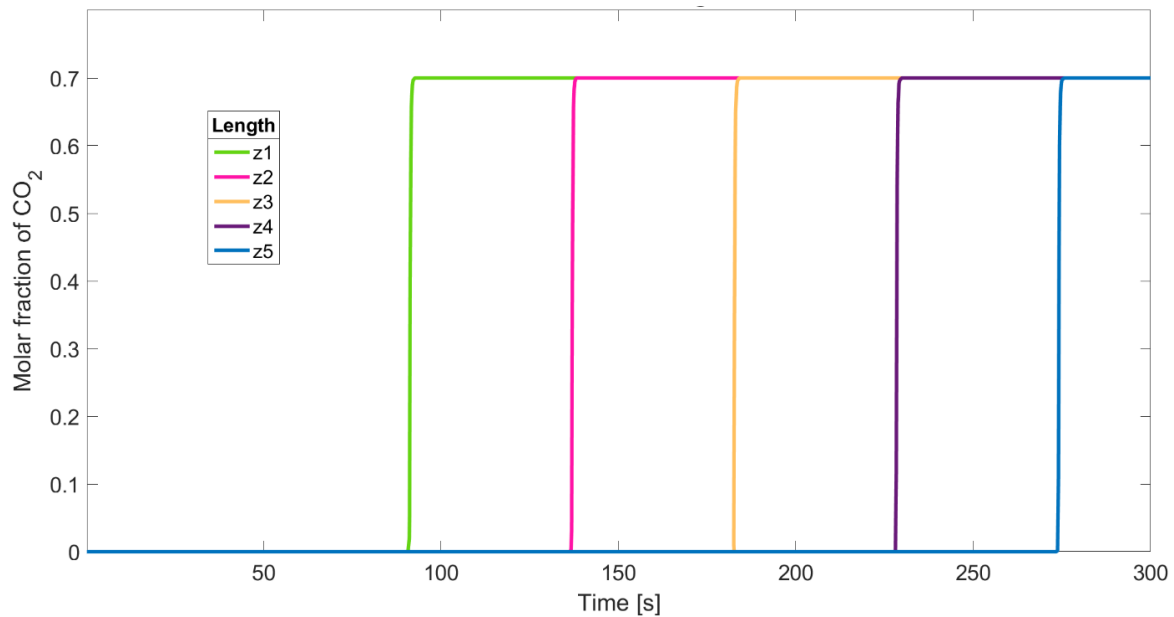


Figure 4.12: Time-based breakthrough curves with the length of the column equal to the equilibrium one. The curves are parametrized for six different consecutive zones of the adsorption step; the last one is the final section of the column.

The system may experience premature breakthrough, which compromises both product purity and process efficiency. To mitigate this risk, an additional portion of column length—referred to as the Length of Unused Bed (LUB)—is incorporated into the design. Including the LUB ensures reliable column operation and helps guarantee that both cycle timing and bed dimensions are sufficient to achieve the desired separation performance. Usually, the LUB has values that stays between 5 and 10 % of the equilibrium length (Pourhakkak et al., 2021). In this case are added 75 mm of LUB to the column.

4.4.3 Non-isothermal adsorption step

PSA processes are often modelled as isothermal to simplify the analysis, under the assumption that temperature variations during the rapid cycle times are minimal and manageable. While this is an approximation, it is generally valid for many systems and allows the focus to remain on the core mechanisms of mass transfer and pressure dynamics. Nevertheless, temperature variations do influence the separation performance by weakening the interactions between the adsorbent material and the target molecules. This effect is evident in the Langmuir isotherms at four different temperatures, as shown in Figure 4.8. Since adsorption is an exothermic process, temperature inevitably rises during the adsorption step, which in turn reduces adsorption capacity. To account for these thermal effects, the complexity of solving energy balance equations must be introduced into the model. Energy balance has the following form:

$$\left[\rho_g c_{p,g} + \left(\frac{1-\varepsilon}{\varepsilon} \right) \rho_s c_{p,s} \right] \frac{\partial T}{\partial t} + \bar{v}_s \rho_g c_{p,g} \frac{\partial T}{\partial z} = - \left(\frac{1-\varepsilon}{\varepsilon} \right) \sum_i \Delta H_i \frac{dq_i}{dt} \quad (4.23)$$

Where $c_{p,g}$ is the heat capacity at constant pressure of the gas phase retrieved in Aspen plus. $c_{p,s}$ the heat capacity at constant pressure of the adsorbent. It is a measure of the solid ability to resist temperature changes when it gains or loses heat and shows how much heat the solid adsorbent can absorb or release per cubic meter of solid for each degree of temperature change. This value is obtained by the article of Subraveti et al. (2021). The isosteric heat of adsorption ΔH_i is the amount of heat released or absorbed when one mole of a component i is transferred from the gas phase to the adsorbed phase. This value has a specific dependence on temperature and pressure and can be calculated with the Clausius Clapeyron equation. Since incorporating the energy balance equation into the model would have been computationally expensive, its solution was instead retrieved from the literature (Park et al., 2016). This provides a relationship between the amount adsorbed and the isosteric heat of adsorption (figure 4.13).

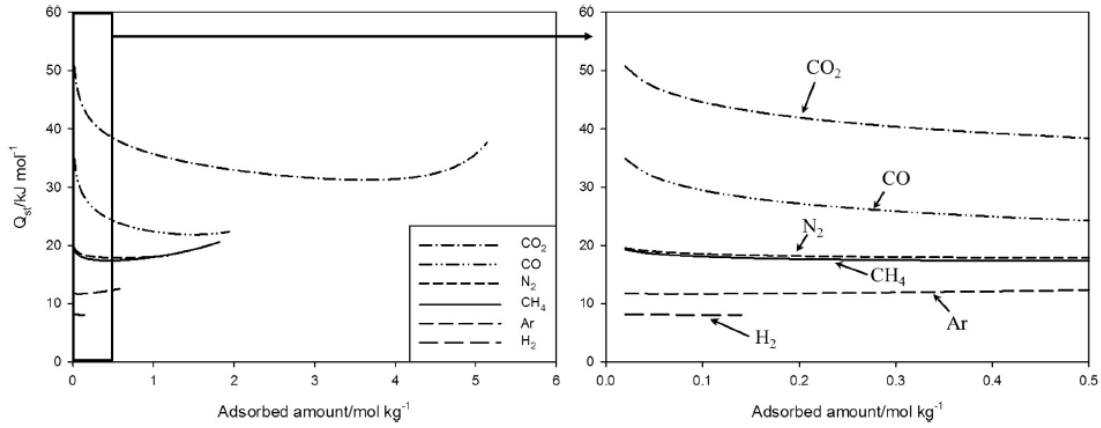


Figure 4.13: Isosteric heat of adsorption on pelletized zeolite 13X with respect to surface loading.

Looking at the left-hand side of the energy balance, the first term quantifies how much thermal energy is being stored per unit volume over time due to changes in temperature of both gas and solid. The second term is the convective heat transport by the gas flow along the axial direction and is the heat carried forward by the flowing gas. The right-hand side has only one term which represents the total heat released or absorbed by adsorption or desorption of all components of the mixture. This term introduces or removes heat depending on whether species are being adsorbed (exothermic) or desorbed (endothermic). In this case only adsorption step is analysed so the heat is always released during the process. The assumption that only carbon dioxide is adsorbed is carried forward also for this simulation. The adsorption term reduces to the heat released by the CO_2 when retained in the zeolite 13X surface. Also, in this case two graphs of the trend of the temperature can be obtained over the time and over the length of the column. Figure 4.14 illustrates the temperature profiles along the column at three different fixed times. Each curve exhibits a similar trend: the temperature rises sharply at a specific point along the

column, remains relatively constant over a certain spatial region, and then gradually decreases back to the feed temperature.

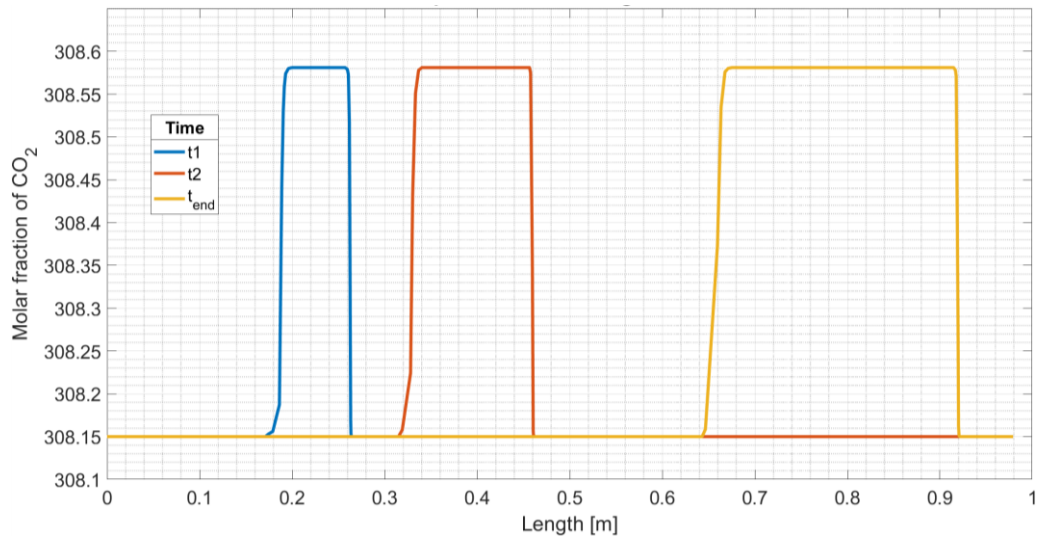


Figure 4.14: Temperature behaviour at three different time over the column.

As CO₂ molecules are adsorbed onto the solid phase, heat is released, resulting in a localized temperature increase visible as a thermal “bump” that propagates along the length of the column. This temperature front advances from the inlet toward the outlet as adsorption proceeds. Its movement is governed by the coupling between mass transfer and heat release: heat is generated in regions where CO₂ is actively adsorbed, while in zones where the adsorbent is already saturated, adsorption slows, heat production ceases, and the temperature gradually returns to baseline. This dynamic behaviour clearly demonstrates the direct link between thermal effects and the progression of the adsorption front within the bed.

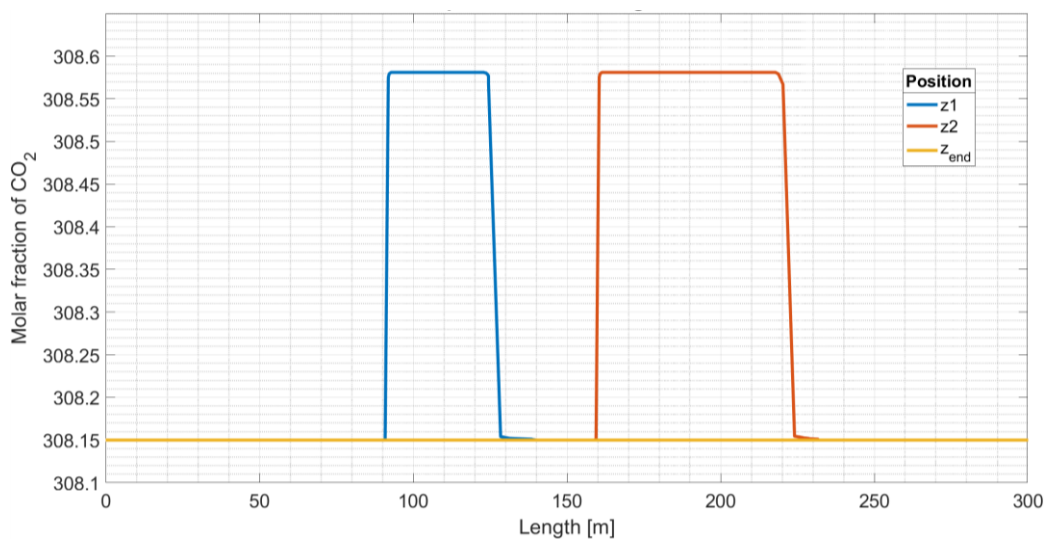


Figure 4.15: Temperature behaviour at three different positions of the column over the time

It must be noted how little is the increase in the temperature that follows the adsorption. Indeed, neither one degree of increase is reached, confirming the feasibility of the isothermal assumption in the description of the PSA unit, at least during the adsorption step.

The results of the simulation can be seen looking at the trends of the molar fraction of CO₂ over the time and over the column, which in this case account also for the LUB and the MTZ.

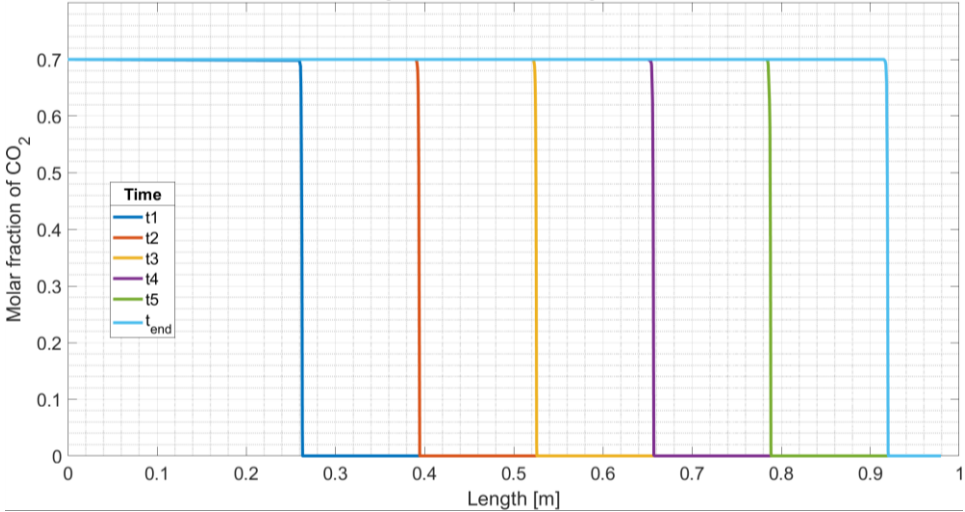


Figure 4.16: Length-based breakthrough curves for the non-isothermal adsorption simulation.

By adding a portion to the equilibrium length, it can be seen how in the length-based breakthrough curves also at the end of the adsorption step, the break point is reached meaning that the complete saturation of the adsorbent is not achieved.

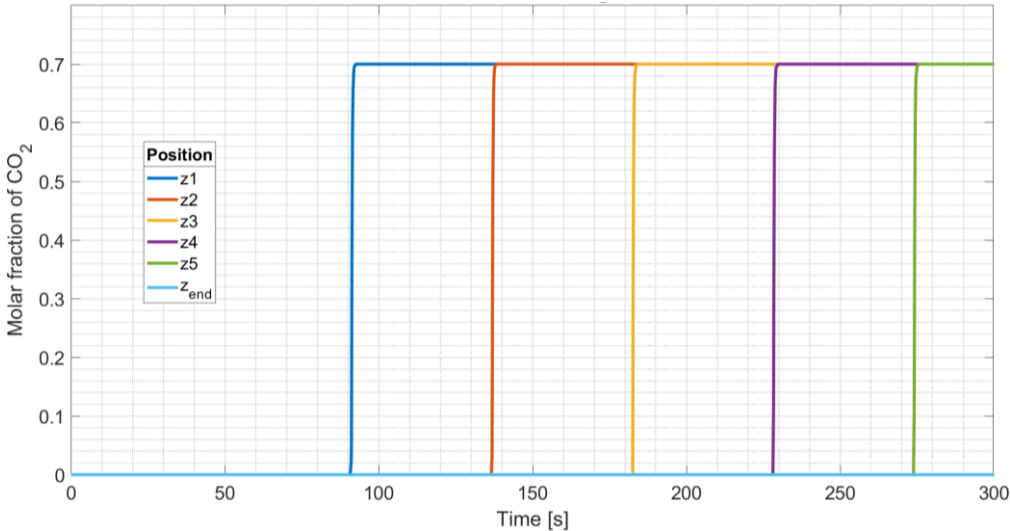


Figure 4.17: Time-based breakthrough curves for the non-isothermal adsorption simulation.

In the time-based breakthrough curves, at the outlet of the bed, the molar fraction of CO₂ has not yet experienced a step increase indicating that a portion of the bed would be still available to adsorb the gas material.

The final dimensions of the column are reported in the following table:

Table 4.7: *Sizing results of the adsorption column.*

Parameter of the column	Unit	Value
Diameter	m	0,304
Total length	m	0,98
Bed volume	m ³	0,071
L/D ratio	-	3,224

The parameters of the sizing will be used as a starting point for the economic analysis developed in Chapter 6.

Chapter 5

Membrane separation unit design

This chapter presents the methodology and the results adopted for the design of the second CO₂ capture technology under consideration: membrane-based separation. The primary objective of the design is to determine the optimal membrane area required to achieve the desired separation performance. In addition, the possibility of implementing a multistage configuration with recycle will be examined to enhance overall process efficiency.

5.1 CO₂ capture membrane unit location in the SYPOX process

The driving force of a membrane gas separations process is the difference in partial pressure of the permeable component in the two side of the membrane. For that reason, it has been chosen to perform the separation from the syngas stream (stream 22 of SYPOX plant) which comes from the low temperature shift reactor.

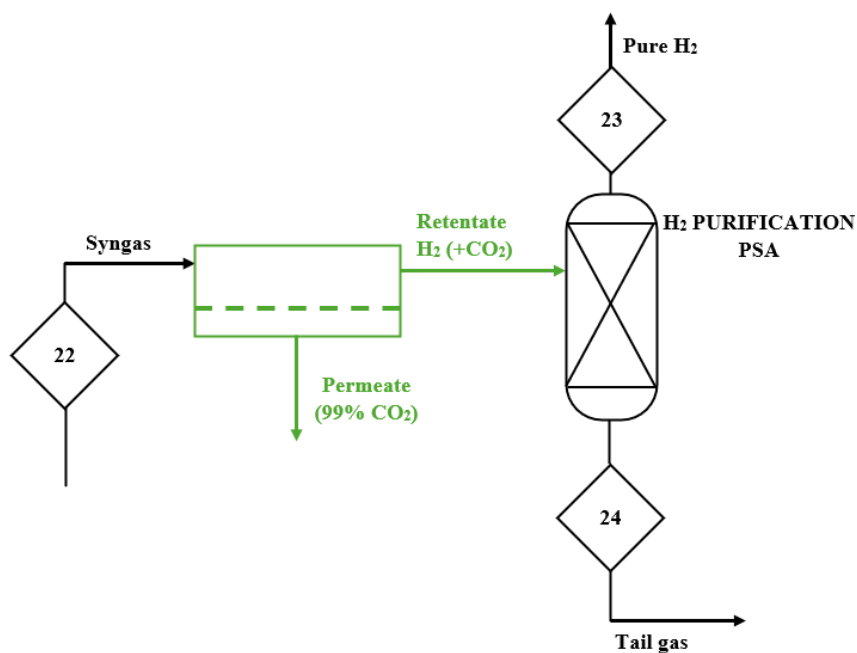


Figure 5.1: BFD with the inclusion of the membrane unit for CO₂ capture.

In the actual process, this stream typically undergoes hydrogen purification via a PSA unit. By implementing membrane-based CO₂ capture upstream of the PSA unit, the subsequent hydrogen purification becomes less energy-intensive and more efficient, due to the reduced CO₂ content in the feed, reducing the cost associated with the PSA already present in the SYPOX plant.

Table 1.1: Syngas stream present in the SYPOX biogas to hydrogen process.

Stream	22
Description	Syngas
Temperature [°C]	35
Pressure [bar]	10
Molar flow [kmol/h]	8.40
Mass flow [kg/h]	134.80
Composition [mol/ mol]	
CO ₂	0.32
CO	0.01
H ₂	0.66
H ₂ O	0.01

As in the PSA modelling, the membrane separation process assumes that the stream consists of a binary mixture composed of 68% hydrogen and 32% carbon dioxide. This simplification is justified by the relatively low concentrations of the other components, water and carbon monoxide, and allows for a more straightforward analysis of component behaviour across the membrane. A second assumption is that the binary H₂/CO₂ mixture behaves as an ideal gas. To assess the validity of this assumption, two thermodynamic models—the Peng-Robinson and the Soave-Redlich-Kwong equations of state—are employed, as was previously done for the tail gas stream. Mass density values are obtained using Aspen Plus by varying the pressure at constant feed temperature. The compressibility factor is calculated using Equation 4.2.

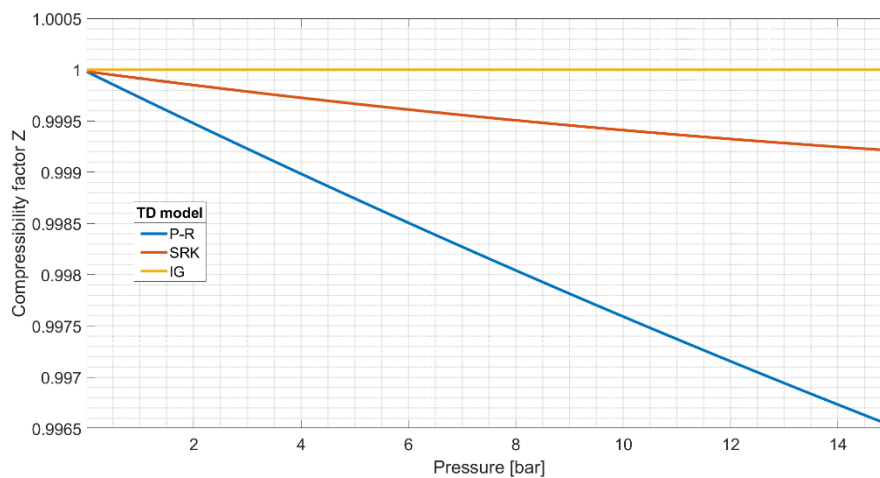


Figure 5.2: Compressibility factor in function of the pressure of the binary mixture hydrogen-carbon dioxide in the syngas for Peng-Robinson and Soave-Redlich-Kwong.

The resulting plot demonstrates that the behaviour of the mixture, as described by both thermodynamic models, closely aligns with that predicted under the ideal gas assumption. Specifically, both the blue and red curves—corresponding to the Peng-Robinson and Soave-Redlich-Kwong models, respectively— in the considered pressure range are nearly close to the yellow curve, representing ideal gas behaviour. The balance to consider in that case will have always the same requirement of purity and recovery. This time the recovery is calculated with respect to the flowrate of CO₂ obtained in the permeate stream:

$$Recovery = \frac{\text{Flowrate of CO}_2 \text{ in the permeate}}{\text{Flowrate of CO}_2 \text{ in the Feed}} \tag{5.1}$$

As in the previous case this value must be equal to 0.9. At the same manner also the CO₂ purity of the permeate stream will be 0.9. Taking the membrane unit as a single block, the overall material balance is shown in figure 5.3:

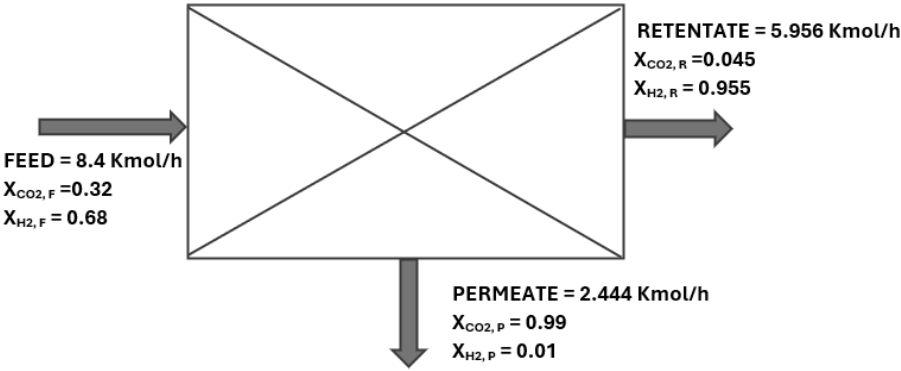


Figure 5.3: Overall material balance for the membrane unit.

The balance fixes the basis to design a proper membrane area for the separation process.

5.2 Membrane model

Several models are commonly used to simulate membrane gas separation, each differing in complexity and accuracy. Considering a single stage membrane, the most widely used three main ways of how the fluid flows across the membrane are explain in figure 5.4. In a co-flow configuration, both the feed and permeate flow in the same direction, parallel to each other along the membrane surface. In counter-flow, the feed and permeate flow in opposite directions, maintaining a higher average driving force across the membrane length and generally achieving better separation performance. In contrast, the cross-flow configuration has the feed gas flowing tangentially to the membrane surface, while the permeate flows perpendicularly through the membrane and is collected at right angles to the feed. The cross-flow model is a widely adopted approach for simulating gas separation in membrane modules, particularly in configurations such as hollow fibre bundles or spiral-wound elements, where the flow geometry supports a tangential arrangement. A key assumption of this model is plug-flow on the feed side: there is

no axial mixing, and both composition and flow rate vary along the membrane length due to the continuous loss of permeating components. This enables the model to capture the gradual decrease in partial pressures and driving force as separation progresses.

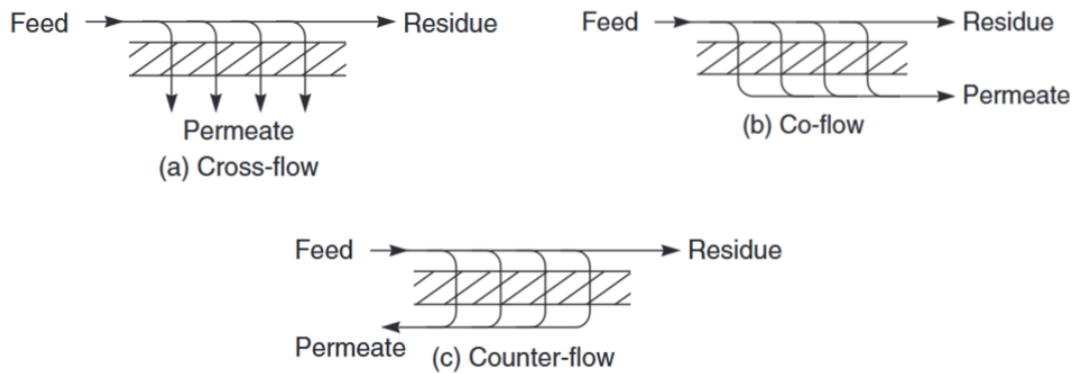


Figure 5.4: *a) Cross-, (b) co-, and (c) counter-flow schemes in a membrane module (Baker et al., 2012).*

On the permeate side, a well-mixed condition is often assumed for simplicity, with constant pressure and composition, though more advanced variants can resolve spatial variations, especially in systems with significant permeate flow or multi-stage designs. Gas transport is typically described by the solution-diffusion mechanism, where flux is proportional to the partial pressure difference across the membrane (Geankoplis, 1993). The cross-flow model balances physical accuracy and computational efficiency, capturing essential separation dynamics without the complexity of fully coupled counter-current formulations. Although it provides a more detailed representation of real systems, for the objectives of this thesis, extremely accurate calculations are not required. For this reason and for sake of simplicity it has been chosen to adopt a model which includes well mixing also in the feed side of the membrane.

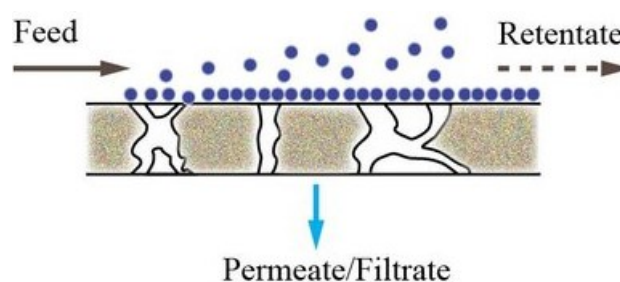


Figure 5.5: *Schematic representation of membrane separation using the cross-flow model (Abetz et al., 2021).*

As in a CSTR the composition and properties of the outlet product are assumed equal to the one inside the reactor, that in this case is the membrane frame. This assumption leads to a model that due to its mathematical simplicity allows for rapid membrane area estimation and straightforward implementation, making it particularly suitable for preliminary design. The main limitation of this approach lies in the assumption of constant driving force, which may lead to an underestimation of the required membrane area when significant changes in feed

composition occur. Nonetheless, the well mixing model offers a practical and efficient tool for early-stage evaluations, representing a reasonable compromise between modelling effort and predictive capability. The equation describing the flux of the CO₂ gas through a membrane, under the assumption of perfect mixing, can be expressed as follows:

$$J_{CO_2} = P_{CO_2} \frac{(x_{CO_2,r}p_0 - x_{CO_2,l}p_l)}{l} \quad (5.2)$$

Where P_{CO_2} is the permeability coefficient of CO₂, l is the membrane thickness, p_0 and p_l are the pressures on the feed side (high-pressure side) and the permeate side (low-pressure side), respectively, and $x_{CO_2,r}$ and $x_{CO_2,l}$ are the constant mole fractions of CO₂ in the retentate and permeate streams (Weller & Steiner, 1950). Since the mixture is assumed to be binary, the molar flux of hydrogen and carbon dioxide across the membrane can each be expressed as a function of the other. Taking the CO₂ molar fraction as the reference, the molar flux of hydrogen through the membrane can be written as follows:

$$J_{H_2} = \frac{P_{CO_2}}{\alpha} \frac{((1 - x_{CO_2,r})p_0 - (1 - x_{CO_2,l})p_l)}{l} \quad (5.3)$$

With α ratio of the permeability coefficients of carbon dioxide and hydrogen. The performance of the membrane can be then defined by the ratio r of the molar composition of the two species in the permeate stream:

$$r = \frac{x_{CO_2,l}}{(1 - x_{CO_2,l})} \quad (5.4)$$

Considering that the flux of both species can be written as a function of the total flux J :

$$J_{CO_2} = Jx_{CO_2,l} \quad (5.5)$$

$$J_{H_2} = J(1 - x_{CO_2,l}) \quad (5.6)$$

The overall mass balance across the membrane must be satisfied:

$$\dot{Q}_F = \dot{Q}_P + \dot{Q}_R \quad (5.7)$$

Being \dot{Q}_F , \dot{Q}_P and \dot{Q}_R the gas molar flowrate respectively in the feed in the permeate and in the retentate stream. Furthermore, also the single species balance needs to be respected, in the case of the carbon dioxide:

$$\dot{Q}_F x_{CO_2,f} = \dot{Q}_P x_{CO_2,l} + \dot{Q}_R x_{CO_2,r} \quad (5.8)$$

The same balance needs to be satisfied for hydrogen. The molar flowrate of a component in the permeate stream is generally expressed as the product of the single species molar flux and the reference membrane area, in the case of CO₂:

$$\dot{Q}_{CO_2,P} = \dot{Q}_P x_{CO_2,l} = J_{CO_2} A \quad (5.9)$$

To solve the material balances presented in Equations 5.8 and 5.9, it is first necessary to specify the retentate stream conditions—namely, the desired molar flow rate and the CO₂ composition in the retentate. Since the feed flowrate and molar fractions are already known that would be sufficient to find the consequent features of the permeate stream. Understanding the value of the carbon dioxide in the permeate stream will be then necessary to solve the flux equation and find the value of J_{CO_2} . The total area necessary to perform the separation with the specified requirements is simply calculated by the ratio of the flowrate and the flux:

$$A = \frac{\dot{Q}_{CO_2,P}}{J_{CO_2}} \quad (5.10)$$

The value of the area must satisfy the requirements of permeation of the CO₂ balancing recovery and selectivity. Furthermore, the calculation of the area is dependent by the retentate specifications pre-selected. In the calculation there will be fixed the molar fraction of the CO₂ in the retentate and there will be evaluated the optimal area to be chosen over a range of total retentate flowrate.

5.3 Membrane material selection

Section 3.3 provided an overview of the potential materials suitable for membrane-based CO₂/H₂ separation. As a preliminary choice, polymeric membranes are preferred over facilitated transport membranes, as the latter still present several unresolved limitations that are currently the subject of ongoing research and development (Scholes et al., 2010). Among the options considered, a membrane composed of PEBAX[®] blended with polyglycol dimethyl ether (PG) was selected, as this combination enhances selectivity toward carbon dioxide. PEBAX[®] is a thermoplastic elastomer composed of alternating segments of polyamide (PA) and polyether (PE) blocks. This structure enables the material to combine the mechanical strength and thermal stability of the polyamide domains with the flexibility and gas affinity of the polyether blocks. The ether-rich domains—particularly those derived from polyethylene oxide (PEO)—play a crucial role in enhancing CO₂ permeability due to acid–base interactions between the polar CO₂ molecules and the electron-rich ether oxygen atoms. In the study by Nguyen et al. (2010), PEBAX[®] 1657 was identified as the most effective grade, exhibiting a CO₂ permeability of up to 100 Barrer (1 Barrer = 3.35e-16 mol · m⁻¹ · s⁻¹ · Pa⁻¹). These properties are linked to its 50/50 PA6/PEO block composition, which balances the need for

sorption capacity (favoured by PEO) and structural integrity (contributed by PA6). The material's semi-crystalline morphology also plays a role: while the crystalline polyamide domains are impermeable, the amorphous and molten polyether phases serve as the main transport paths for gas molecules. As a result, PEBAX[®] membranes function well under the solution-diffusion mechanism, exhibiting high CO₂ solubility and sufficient diffusivity. Moreover, PEBAX[®] can be processed into thin films via extrusion or casting, facilitating the development of scalable membrane modules for industrial use. Its commercial availability, chemical stability, and ease of surface modification (e.g., via cold plasma to graft amine groups) make it an adaptable platform for membrane engineering. Despite the favourable baseline performance of pure PEBAX[®], further enhancement is often needed to meet industrial benchmarks, particularly regarding the permeability-selectivity trade-off. To address this, researchers have explored blending PEBAX[®] with additives such as polyglycol dimethyl ether (PG), a short-chain PEG derivative known for its CO₂- character. Blending PEBAX[®] with PG improves the free volume and the overall solubility of CO₂, leveraging the acid-base interactions between CO₂ and the ether groups in PG. Nguyen et al. observed that blending with 20 wt.% of PEG300 led to a CO₂ permeability of 128 Barrer, significantly surpassing the performance of pure PEBAX[®] 1657. However, miscibility and phase stability issues emerged at higher PG loadings, where phase separation and PEG migration could reduce performance and membrane integrity. The practical relevance of PEBAX[®]/PG membranes was further validated in a techno-economic study by Franz and Scherer (2010), who used Pebax/PG50 (i.e., a 50 wt.% blend) as the reference membrane in a simulation of CO₂ separation within an IGCC (Integrated Gasification Combined Cycle) power plant. The features of the membrane are reported in table 5.1 and will be used as a reference to develop the calculation for the membrane area. PEBAX[®]-based membranes are commonly implemented in flat-sheet or hollow fibre module configurations, depending on the application and fabrication method. Owing to their excellent film-forming properties and compatibility with solution-casting techniques, dense flat-sheet membranes made from PEBAX[®], or its blends are widely employed in laboratory-scale studies and pilot systems. These membranes are often integrated into spiral-wound or plate-and-frame modules, which offer good packing density and modular scalability for gas separation applications. Additionally, PEBAX[®] can be extruded into thin, defect-free films and supported on microporous substrates, making it suitable for use in thin-film composite (TFC) membranes.

Table 5.2: Features of the PEBAX[®]/PG-based membrane (Franz & Scherer, 2010).

Parameter	Unit of measure	Value
Selectivity CO ₂ / H ₂	-	15.50
Thickness	µm	0.5
Permeability-CO ₂	kmol/(h bar m)	3.3876e-9

In TFC configurations, the selective PEBA[®]X layer is deposited over a porous support material (e.g., polysulfone or polyacrylonitrile), enhancing gas permeability while preserving mechanical stability. This structure is frequently adopted in spiral-wound modules for industrial applications. In the reference study by Franz and Scherer, hollow fibre modules were assumed for the membrane configuration.

5.4 Membrane unit configuration

Once the membrane properties are defined, it becomes possible to calculate the membrane area required to achieve the target separation. When this calculation is performed for a single-stage configuration, the results indicate that a very large membrane area would be needed, and even then, the desired separation requirements are not fully satisfied. To address this issue, the first approach considered involves reducing the pressure on the permeate side using a vacuum pump that reaches a vacuum grade of 0.5 bar (see Figure 5.5). This strategy increases the driving force across the membrane by lowering the partial pressures of the permeating components, thereby enhancing the carbon dioxide flux and reducing the membrane area (Vallières & Favre, 2004).

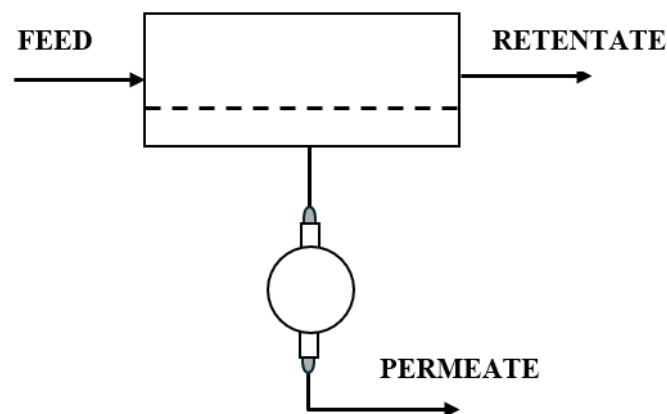


Figure 5.6: *Single stage configuration with vacuum pump.*

By imposing a CO₂ molar fraction of 0.045 in the retentate, as required by the material balances, it was found that the membrane area needed to achieve the desired separation is extremely large across a range of imposed retentate flow rates. The mass balances described in Section 5.2 were solved using MATLAB, and the resulting plots—showing how the retentate and permeate flow rates vary with membrane surface area—are presented in Figure 5.7 and 5.8. In the analysed range, the CO₂ permeation rate becomes insensitive to further increases in surface area, whereas hydrogen permeation continues to rise. This behaviour is attributed to the membrane's high selectivity toward CO₂, which allows it to permeate even at lower surface areas. The plots clearly indicate that achieving the target CO₂ purity in a single-stage configuration is not feasible. This observation is further confirmed by Figure 5.9, which illustrates the variation of

CO₂ molar fraction in the permeate as a function of membrane area. These results suggest that a multi-stage separation process is required. As membrane area increases, the total amount of permeating material also increases.

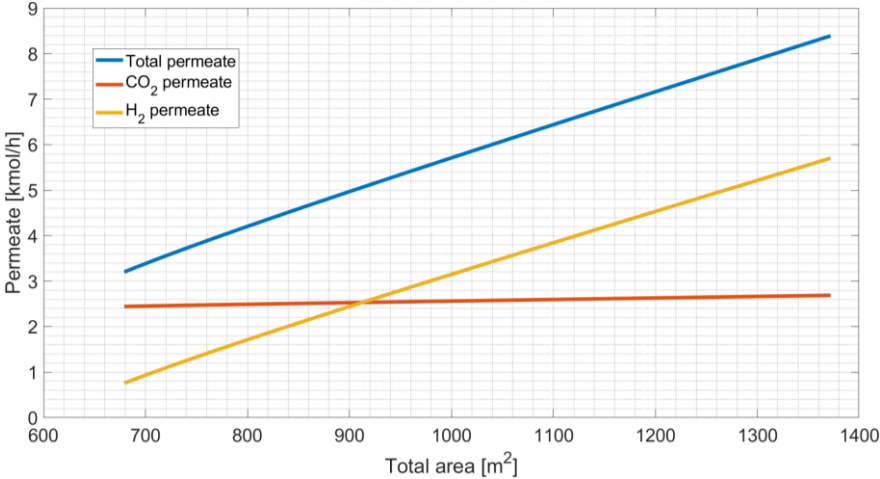


Figure 5.7: Permeate variation as a function of the membrane surface.

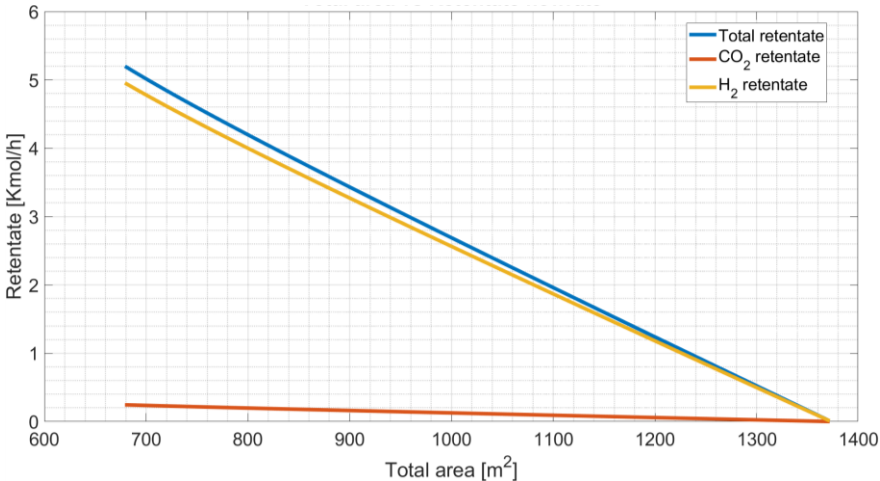


Figure 5.8: Retentate variation as a function of the membrane surface.

Notably, CO₂ permeates more readily than hydrogen, even at lower membrane surface areas, due to the membrane’s favourable selectivity. However, as the area continues to increase, a greater amount of hydrogen also begins to permeate. Therefore, it becomes necessary to design a membrane system that produces a permeate stream with a high CO₂ molar fraction and a moderate flow rate. This enables the implementation of a second separation stage, aimed at further purifying the permeate from the first stage to reach the desired CO₂ purity.

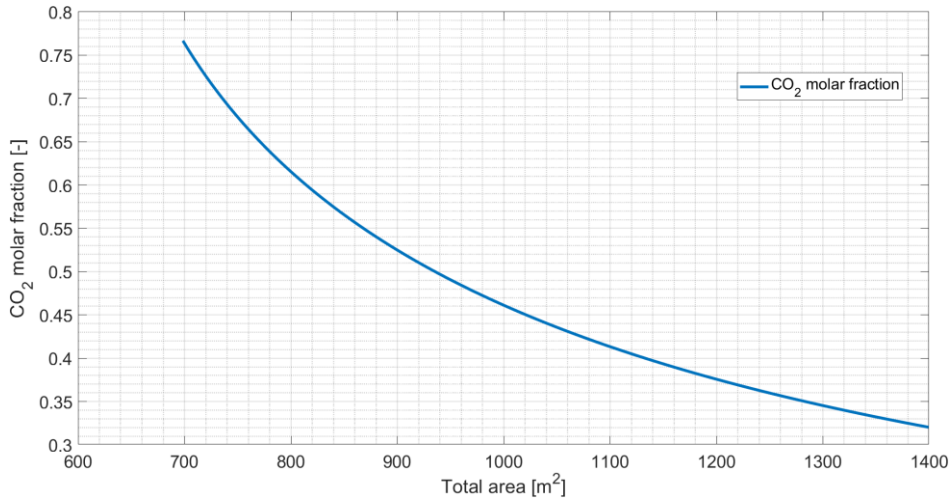


Figure 5.9: *CO₂ molar fraction variation in the permeate as a function of the membrane area.*

The selected membrane area is of 710 m² because increasing further the area, the molar fraction of CO₂ would have been too low. The features of the retentate and permeate streams are reported in table 5.3.

Table 5.3: *Feature of the first stage membrane separation*

First stage membrane-based separation

Parameter	Unit	Value
Membrane		
Area	m ²	710
Retentate		
Molar flowrate	Kmol/h	5.135
CO ₂ molar fraction	-	0.045
H ₂ molar fraction	-	0.953
Total pressure	bar	10
Permeate		
Molar flowrate	Kmol/h	3.304
CO ₂ molar fraction	-	0.744
H ₂ molar fraction	-	0.256
Total pressure	bar	0.5

Performing a second separation stage in series with the first is therefore necessary to achieve the desired product specifications. After the initial separation, the permeate stream exits at sub-atmospheric pressure due to the operation of the vacuum pump. To enable a second membrane stage, this stream must be recompressed to increase the pressure on the feed side of the second membrane. In this design, the pressure is raised to 10 bar, while a vacuum pump is again employed on the permeate side to maintain sub-atmospheric pressure, also in that case at 0.5 bar. This configuration creates a high driving force across the membrane, thereby enhancing the separation efficiency in the second stage. The mass balances for the second separation stage are solved by fixing the molar fraction of carbon dioxide in the retentate to the same value as

that of the first-stage retentate (i.e., 0.045). The two retentate streams are then combined and directed to the subsequent hydrogen purification unit in the SYPOX process. This approach eliminates the need to recycle the retentate from the second stage and ensures that no gas stream is vented to the atmosphere.

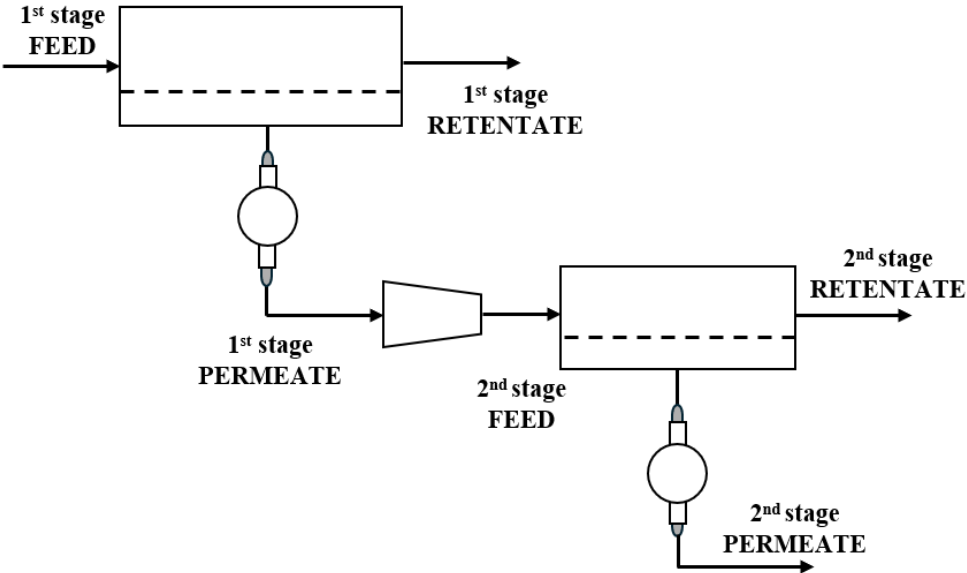


Figure 5.10: Final configuration of the membrane separation unit. The two stages with their streams are shown.

Based on the results obtained from the mass balance calculations, the membrane area required in the second separation stage to achieve the final desired specifications is found to be 630.88 m².

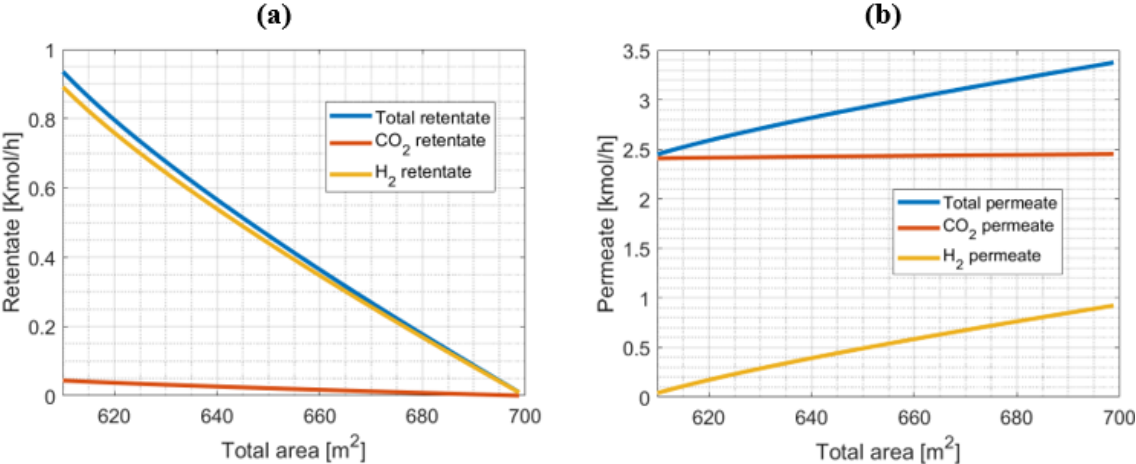


Figure 5.11: Variations of the flowrate with the membrane area in the second stage. (a) retentate flowrate. (b) permeate flowrate.

As observed in the first separation stage, increasing the membrane area beyond the calculated optimal value leads to a substantial rise in hydrogen permeation. This is a direct consequence of using the same membrane material, which, while highly selective toward CO₂, still allows hydrogen to pass through at larger surface areas. Such an effect compromises the separation

performance by diluting the CO₂ content in the permeate stream, ultimately preventing the system from meeting the required purity specifications. Therefore, precise sizing of the membrane is crucial to maintaining the desired balance between CO₂ recovery and hydrogen retention. The detailed results of the second separation stage are presented in Table 5.4

Table 5.4: *Feature of the second stage membrane separation.*

Second stage membrane-based separation			
Parameter	Unit	Value	
Membrane			
	Area	m ²	630.88
Retentate			
	Molar flowrate	kmol/h	0.860
	CO ₂ molar fraction	-	0.045
	H ₂ molar fraction	-	0.955
	Total pressure	bar	10
Permeate			
	Molar flowrate	kmol/h	2.444
	CO ₂ molar fraction	-	0.99
	H ₂ molar fraction	-	0.01
	Total pressure	bar	0.5

The second stage of separation is designed to further purify the permeate stream obtained from the first stage. While the quantity of material to be treated is smaller compared to the initial separation, the performance requirements are more stringent, with a target CO₂ molar fraction of 0.99 and a recovery of 90%. To meet these criteria, a smaller membrane area is required relative to the first stage. This reduction in membrane size not only aligns with the lower material throughput but also results in a less significant cost contribution from the second membrane module—an aspect that will be further discussed in the economic analysis presented in the following chapter.

Chapter 6

Economic analysis

This chapter presents the economic analysis of both the PSA and membrane-based processes. A comprehensive techno-economic evaluation is essential to determine which of the two technologies is more suitable for carbon capture in the SYPOX plant. The first two sections focus on estimating the capital expenditures (CAPEX) and operating expenditures (OPEX) associated with each process, including the costs of auxiliary equipment such as pumps, compressors, and valves. Additionally, a dedicated section will present the updated Hydrogen Production Cost (HPC) and carbon footprint of the plants using firstly the PSA and then the membranes as CO₂ capture technology. Finally, a comparative assessment between the results obtained with the two techniques will be conducted to support the overall conclusions of the thesis.

6.1 CAPEX and OPEX definition

Regarding capital cost estimation, it must be firstly determined the Bare Erected Cost (BEC) for each piece of equipment. According to NETL (2011), the BEC includes the cost of process equipment along with the direct and indirect labour required for its construction and installation. These cost estimates are developed for each process component retrieving data from articles which in turn has developed the cost models from databases and the software packages Aspen Economic Process Analyzer[®]. After the Bare Erected Cost for each equipment is found, there must be calculated the annual cost of this expense over a determined period. The capital costs are annualized using an amortization function. This function is derived by calculating the constant annual payment required to repay the initial investment, including interest, over a fixed period. The goal is to determine the uniform annual cost that, when deposited into a fund each year, would fully cover both the capital expenditure and the accrued interest by the end of the specified term (Turton, et al., 2018). So, there can be defined an annual capital charge ratio, ACCR as:

$$ACCR = \frac{i(1+i)^n}{(1+i)^n - 1} \quad (6.1)$$

Where i is the taxation rate to be assumed and n is the payback period in which the capital costs must be depreciated. To find the annualised CAPEX is sufficient to multiply the annual capital charge ratio by the total BEC of each process.

$$CAPEX_{annualised} = ACCR * BEC_{total} \quad (6.2)$$

Table 6.1 shows the values assumed for this calculation.

Table 6.1: Specifics for the calculation of the ACCR

<i>Parameter</i>	<i>Value</i>
<i>Payback period (years)</i>	<i>10</i>
<i>Interest rate</i>	<i>0.1</i>
<i>ACCR</i>	<i>0.163</i>

The Total Annualized Cost (TAC) can then be found as the sum of the annualized capital expenditure (CAPEX) and the operating expenditure (OPEX), the latter already calculated on an annual basis:

$$TAC = CAPEX_{annualised} + OPEX \quad (6.3)$$

The operating costs considered in this analysis account solely for electricity consumption by equipment such as vacuum pumps and compressors, as electricity is the only utility included in the design of both the PSA and membrane separation processes. The cost of electricity per kWh (0.08 €/kWh) and the total annual operative hours (8000 hours/year) are data necessary to carry out the OPEX and are assumed equal to the ones considered for the SYPOX biogas to hydrogen techno economic analysis.

6.2 PSA

The economic analysis begins by evaluating the equipment required for the PSA process. This includes adsorption columns, vacuum pumps, valves, as well as the cost of the adsorbent material and its periodic replacement. To develop the functions used for calculating the Bare Erected Cost (BEC) of each piece of equipment, the study by Subraveti et al. (2020) is taken as a reference. Their work derived these cost functions using Aspen Process Economic Analyzer[®] across a wide range of cases, considering various design variables.

6.2.1 Columns

For the column Subraveti et al. (2020) considered 156 cases encompassing a wide range of design characteristics. Economic evaluations were performed across varying column diameters

(D), length-to-diameter (L/D) ratios, and operating pressures. The resulting BEC function, is based on these three variables and is presented in Equation (6.4):

$$BEC_{column} = \exp(a \cdot D + b \cdot L/D + c \cdot P + d) \quad (6.4)$$

Here the pressure is referred as the operating pressure in the column during the adsorption step. Regarding the OPEX the column do not need any electricity to work since the separation is based on the differences of pressure in the various steps. The result of the single column BEC will be multiplied by the number of columns necessary to perform the PSA process.

In table 6.2 are presented the regression parameters and the specifics of the column.

Table 6.2: Capital cost of the columns

<i>Parameter</i>	<i>Value</i>	<i>Unit</i>
<i>Coefficient a</i>	0.415	-
<i>Coefficient b</i>	0.074	-
<i>Coefficient c</i>	0.023	-
<i>Coefficient d</i>	10.808	-
<i>Column diameter</i>	0.304	<i>m</i>
<i>L/D ratio</i>	3.224	-
<i>Operating pressure</i>	1.03	<i>bar</i>
<i>Number of columns</i>	5	-
<i>BEC_{column}</i>	72,805.18	€
<i>BEC_{5 columns}</i>	364,025.90	€

As will be seen later columns are the major expenses in the PSA capital expenses.

6.2.2 Vacuum pumps

For a reliable vacuum pump bare erected cost estimation, is used a function based on two key design characteristics of the vacuum pump:

- Volumetric flow rate
- Suction pressure

Hence, a direct cost function with volumetric flow rate of the evacuation step \dot{Q}_{evac} was regressed as shown in Eq. 6.5.

$$BEC_{vac. pump} = (a \cdot \dot{Q}_{evac})^b + c \quad (6.5)$$

In table 6.3 the parameters for the resolution of equation 6.5 are shown.

Table 6.3: Parameters for calculating the capital cost of the vacuum pumps

Parameter	Value	Unit
<i>Coefficient a</i>	423.900	-
<i>Coefficient b</i>	0.653	-
<i>Coefficient c</i>	30000	-
<i>Volumetric Flow rate</i>	1265.171	m^3/h
<i>Suction pressure</i>	0.05	bar
<i>Number of pumps</i>	4	-
<i>BEC_{vac. pump}</i>	74,974.57	€
<i>BEC_{4 vac pumps}</i>	299,898.26	€

Furthermore, For the vacuum pump, it is necessary to estimate electricity consumption to calculate the operating costs. The energy consumption is modelled as an isentropic expansion process, with the required power calculated over the duration of the evacuation step.

Table 6.4: OPEX of the vacuum pumps

Parameter	Value	Unit
<i>Energy consumption</i>	0.371	kWh
<i>Evacuation time</i>	1000	s
<i>Power</i>	1.335	kW
<i>OPEX_{vac. pump}</i>	854.32	€/year
<i>OPEX_{4 vac pumps}</i>	3,417.29	€/year

The operating expenditure (OPEX) is then determined by multiplying the calculated power by the electricity price and dividing by the total number of annual operating hours.

6.2.3 Switching valves

Due to the cyclic nature of VSA operation, switching valves are essential for executing the cycle sequence. In the specific VSA cycle considered, three switching valves are required per column. The first valve connects the column to the feed stream, the second links it to the vacuum pump for the evacuation step, and the third allows for the release of the raffinate stream. Given that the number of columns needed to capture the tail gas is five, the total cost of valves becomes significant. Therefore, the BEC cost of each valve is assumed to be €2,000 (Susarla et al., 2015). The total BEC considering fifteen valves is €30,000.

6.2.4 Adsorbent

The bare erected cost associated with the adsorbent include the purchase cost (PC) and the transport and installation cost (TIC), and were calculated as follows:

$$BEC_{ads} = N \cdot V_{column} \cdot (1 - \varepsilon) \cdot \rho_s \cdot (PC + TIC) \quad (6.6)$$

With N number of total columns in the PSA unit, V_{column} the volume of a single column, ε the void fraction and ρ_s the solid density. Zeolite 13X has been widely deployed industrially and its purchase cost was estimated to €1,500 per tonne (Danaci et al., 2020). The transport and installation costs associated with the adsorbent were set at €1,500 since for commercial adsorbents, these costs are typically comparable to the purchase cost, and this assumption ensures a consistent and realistic estimate of the overall adsorbent direct cost (Subraveti et al., 2021). An important component of adsorbent costs is the replacement of the material over time, due to thermal or mechanical degradation. Although some commercial adsorbents can operate for up to 20 years, a conservative replacement interval of 5 years was adopted (Danaci et al., 2020). The adsorbent replacement cost—which includes purchase, transport, and installation—is incurred once, five years after plant start-up, given the plant's assumed lifetime of 10 years.

Table 6.5: Capital cost for the Zeolite 13X purchase, installation and replacement.

<i>Parameter</i>	<i>Value</i>	<i>Unit</i>
<i>PC</i>	<i>1,500</i>	<i>€/tonne</i>
<i>TIC</i>	<i>1,500</i>	<i>€/tonne</i>
<i>BEC_{ads}</i>	<i>25,170.75 €</i>	<i>€</i>
<i>Adsorbent life</i>	<i>5</i>	<i>years</i>
<i>BEC_{replacement}</i>	<i>25,170.75 €</i>	<i>€</i>
<i>BEC_{tot, ads}</i>	<i>50,341,50</i>	<i>€</i>

The cost of replacement is assumed to be equal to that of the initial installation.

6.2.5 Total annualised costs

By summing the Bare Erected Costs of the PSA unit equipment and the adsorbent, the total capital investment can be determined. This value is then multiplied by the Annual Capital Charge Rate (ACCR) to calculate the annualized capital cost of the unit. The results are shown in table 6.6.

Table 6.6: Annualised capital costs for the PSA unit.

<i>Category</i>	<i>Value [€/year]</i>
<i>Columns</i>	<i>59,243.54</i>
<i>Vacuum pumps</i>	<i>48,807.06</i>
<i>Valves</i>	<i>4,882.36</i>
<i>Adsorbent</i>	<i>16,385.69</i>

The impact of columns, vacuum pumps, valves and adsorbent on the capital cost is shown in figure 6.1.

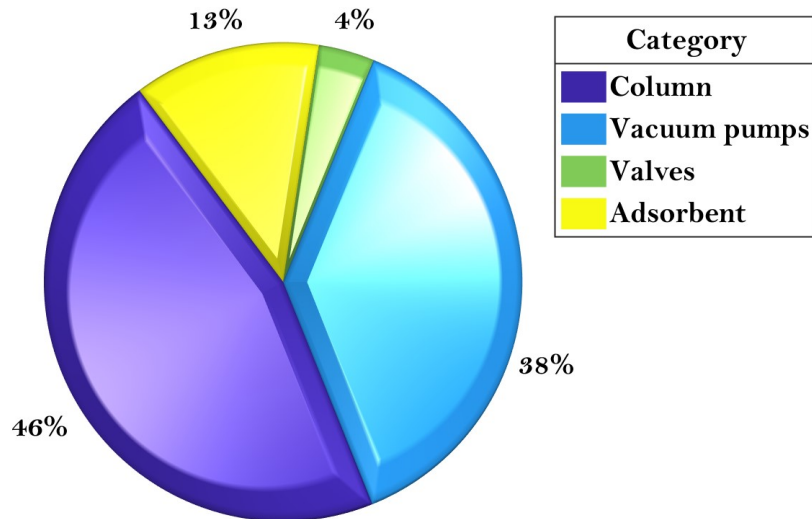


Figure 6.1: Impact of the equipment on PSA annualised capital cost. The percentage of the columns, vacuum pumps, switching valves and adsorbent with respect to the overall capital costs is presented.

The largest share of the investment is attributed to the adsorption columns, underscoring their structural and functional importance in the PSA process. This is followed by vacuum pumps, which represent 38% of the capital costs, reflecting the critical role of pressure manipulation in the system. The overall cost of the zeolite 13X materials, account for 12% of the costs. The switching valves contribute the remaining 4%, indicating they contribute to a non-negligible part of the capital investment. Overall, the breakdown highlights that the core process components—columns and vacuum pumps—are the primary drivers of capital expenditure in PSA systems. By summing the annualised capital costs with the operating costs, the TAC is calculated as reported in table 6.7.

Table 6.7: Total annualised costs of PSA unit.

<i>Variable</i>	<i>Value [€/year]</i>
<i>CAPEX_{ann.}</i>	<i>129,318.66</i>
<i>OPEX</i>	<i>3,417.29</i>
<i>TAC</i>	<i>132,735.95</i>

As illustrated in Figure 6.2, the OPEX associated with the vacuum pump represents a small portion of the total operating costs of the PSA unit.

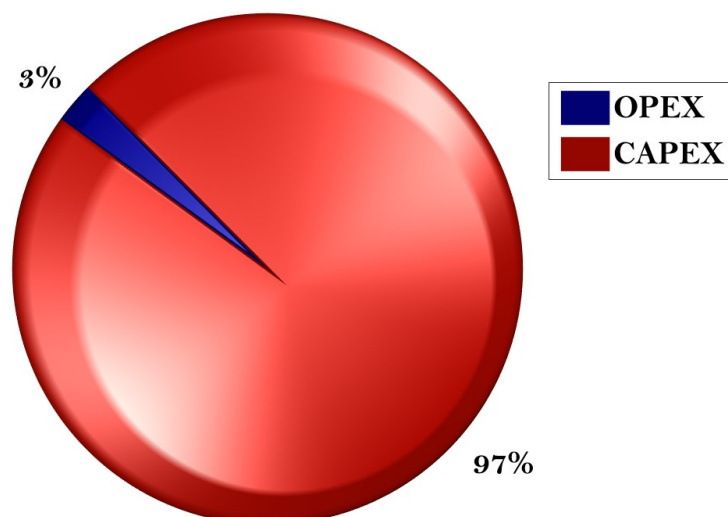


Figure 6.2: Total annualised Costs breakdown between CAPEX and OPEX.

The low vacuum pressure required results in substantial electricity consumption. However, the graph indicates that the PSA system is capital-intensive, with upfront investments exerting a greater influence on the overall cost structure compared to ongoing electricity consumption of the vacuum pumps.

6.3 Membrane-based separation.

The economic analysis for the membrane-based CO₂ capture process includes the cost estimation of membranes for both separation stages, as well as the associated vacuum pumps and compressor. As with the PSA system, the operating expenses are primarily attributed to the electricity consumption of these components. The capital expenditure related to the membranes encompasses both the cost of the membrane material itself and the structural frame in which it is housed. A breakdown of the total annualised cost will be done, to understand the impact of CAPEX and OPEX.

6.3.1 Membranes material and frame

The membrane material cost is calculated simply by multiplying the area of each of the two membranes by the reference cost of the material. This cost is estimated, for a PEBAX[®] blended with PG membrane composed of hollow fibre modules to be 150 €/m² (Arias et al., 2016). It is assumed that the membrane material has a lifetime of 5 years. Given that the overall plant skid lifetime is set at 10 years, the membrane material will require one replacement during the plant's operational period. Another cost component to be considered is that of the membrane frame, which refers to the structural support or housing that secures the membrane material within the membrane module. The cost model used in this analysis is inspired by the approach presented in the study by Zhao et al. (2010). The formula derived to

calculate the bare erected cost is based on the reference frame cost k and on the membrane area A_{mb} :

$$BEC_{frame} = k \cdot \left(\frac{A_{mb}}{2000} \right)^{0.7} \quad (6.7)$$

The calculation of the material, the replacement and the frame cost for the two membranes are presented in the table below:

Table 6.8: Capital cost attributed to the membranes.

Parameter	Membrane 1	Membrane 2
<i>Area (m²)</i>	710	630.88
<i>Material cost (€/m²)</i>	150	150
BEC Material (€)	94,785.00	84,222.35
<i>k-Frame cost (M€)</i>	0.238	0.238
BEC Frame (€)	102,595.15	94,451.36
BEC Replacement (€)	94,785.00	84,222.35

The results indicate that, as expected, the costs for each category are higher for the first membrane stage than for the second, due to the larger membrane area required. Among the various cost components, the membrane frame accounts for the highest share of the Bare Erected Cost, reflecting its structural complexity and material requirements.

6.3.2 Vacuum pumps

The calculation of the costs of the two vacuum pump follows the same procedure used for the vacuum pumps in the PSA unit. The bare erected cost is then calculated with equation 6.5. The operating expenses due to the electricity consumed, necessitate to calculate the power consumption of the pumps. The electricity cost and the operating hours are also in this case respectively 0.08 €/kWh and 8000 hours/year.

Table 6.9: Capital and operating cost for the two vacuum pumps

Parameter	Vacuum pump 1	Vacuum pump 2
<i>Vol. Flow rate (m³/h)</i>	169.286	137.739
<i>Suction pressure (bar)</i>	0.5	0.5
BEC vac. pump (€)	42,093.53	40,569.83
<i>Power consumption (kW)</i>	1.722	1.311
OPEX vac. pump (€/year)	1,134.14	839.03

The first vacuum pump handles a larger volume of material compared to the second, which is reflected in its higher cost. Since the Bare Erected Cost of a vacuum pump is primarily influenced by the required suction pressure, the two pumps used in the membrane separation process are less expensive than those in the PSA unit. This is due to the lower vacuum levels they are required to achieve.

6.3.3 Compressor

The compressor Bare Erected Cost is calculated based on the study of Subraveti et al. (2020). Actual inlet volumetric flow rate \dot{Q}_{comp} and outlet pressure P_{out} are the parameters used to represent the cost estimations for compressors. The regression is shown in equation 6.8.

$$BEC_{Comp} = a \cdot (\dot{Q}_{comp})^b + c^{P_{out}} \quad (6.8)$$

Also, the OPEX due to the electricity consumption of the compressor must be calculated. The power is calculated performing an isothermal compression. The results of the cost calculation are shown in the following table.

Table 6.10: Regression parameters and cost calculation of the compressor.

<i>Parameter</i>	<i>Value</i>	<i>Unit</i>
<i>Coefficient a</i>	121.412	-
<i>Coefficient b</i>	0.9	-
<i>Coefficient c</i>	1.032	-
<i>Volumetric Flow rate</i>	169.286	m^3/h
<i>Outlet pressure</i>	10	bar
<i>BEC_{comp.}</i>	16,858.44	€
<i>Power consumption</i>	2.351	kW
<i>OPEX_{comp.}</i>	1,504.76	€/year

6.3.4 Total annualised costs

By summing the Bare Erected Costs (BEC) of the membrane unit equipment and the associated components, the total capital investment is determined. This value is then multiplied by the Annual Capital Charge Rate (ACCR) to obtain the annualized capital cost of the unit. The results of this calculation are presented in Table 6.11.

Table 6.11: Annualised capital costs for the membrane unit.

<i>Category</i>	<i>Value [€/year]</i>
<i>Membrane 1</i>	47,548.53
<i>Membrane 2</i>	42,785.12
<i>Vacuum pump 1</i>	6,850.53
<i>Vacuum pump 2</i>	6,602.55
<i>Compressor</i>	2,743.63

The breakdown of the capital cost and the consequent impact of each equipment are represented in the pie chart in figure 6.3:

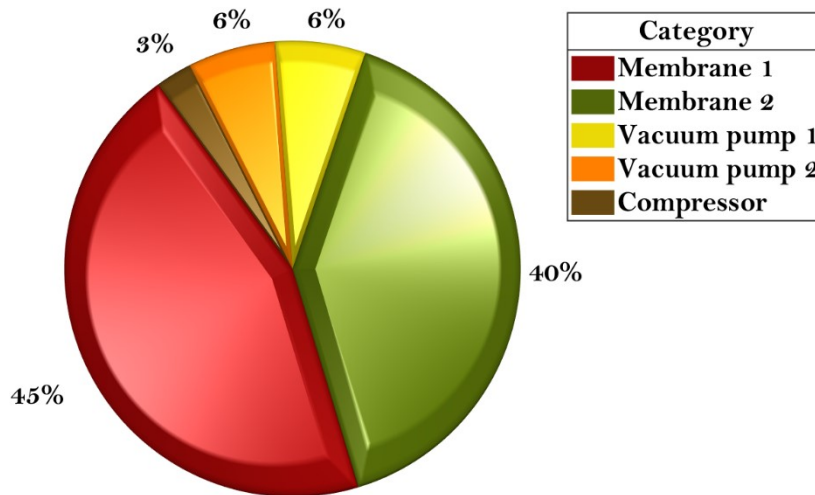


Figure 6.3: *Impact of the equipment on Membranes annualised capital costs. The percentage of the two membranes, the two vacuum pumps, switching valves and compressor with respect to the overall capital costs is presented.*

In the cost calculation, the expenses associated with the two membranes include the material, frame, and replacement costs. As a result, the membranes alone account for approximately 85% of the total capital expenditure, with the first stage contributing slightly more due to its larger membrane area. The two vacuum pumps have a comparable impact on CAPEX, while the compressor represents the least expensive component in the economic analysis.

Going on with the analysis also the OPEX in this case must be broken down into each component electricity consumption price. The operating expenses of the compressor and the two vacuum pumps are shown in figure 6.4

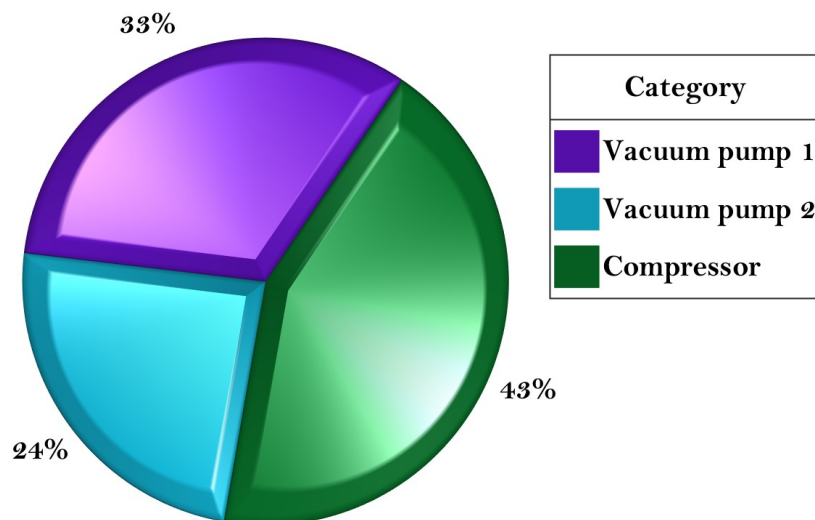


Figure 6.4: *OPEX of the two pumps and the compressor.*

The graph clearly shows that the compressor is the equipment with the greatest impact on annual operating expenses, contributing approximately 43%. This was expected, as it has the highest power consumption among the equipment considered. However, the two vacuum pumps also contribute significantly to the OPEX, given their comparable power requirements. Specifically, the first vacuum pump accounts for 33% of the operating costs, while the second contributes 24%.

Finally, the contributions of both the annualized CAPEX and OPEX, along with the calculated Total Annualized Cost (TAC) of the membrane-based system are presented.

Table 6.12: Total annualised costs of Membranes-unit.

<i>Variable</i>	<i>Value [€/year]</i>
<i>CAPEX_{ann.}</i>	<i>106,530.37</i>
<i>OPEX</i>	<i>3,477.94</i>
<i>TAC</i>	<i>110,008.31</i>

The operating expenses (OPEX) associated with the electricity consumption of the two vacuum pumps and the compressor represent only a small fraction—approximately 3%—of the total annualized costs of the membrane unit. In contrast, capital investment (CAPEX) accounts for the overwhelming majority at 97%, highlighting the highly capital-intensive nature of the membrane-based CO₂ separation process.

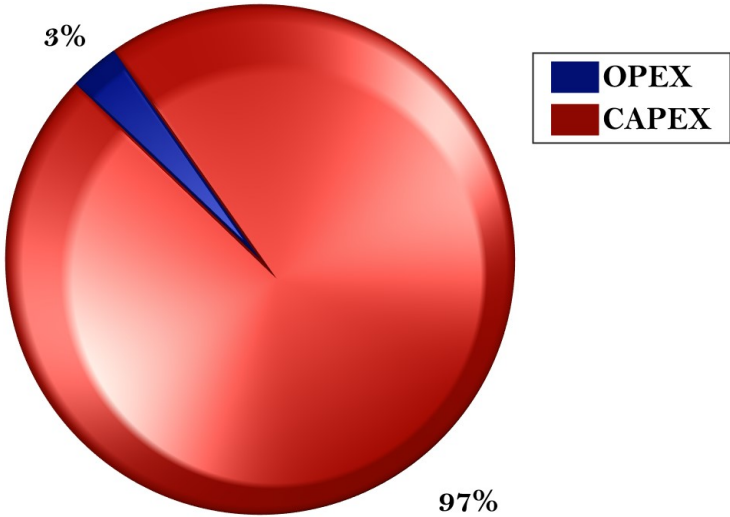


Figure 6.5: Total Annualised Costs breakdown.

This cost distribution suggests that optimizing membrane cost and durability is critical for improving the economic viability of the technology, as further reductions in OPEX would have a limited effect on the overall cost structure.

6.4 Technologies comparison

A final assessment is conducted by comparing the economic expenditures associated with the two carbon capture technologies, considering capital expenditure (CAPEX), operating expenditure (OPEX) and the total annualized cost (TAC).

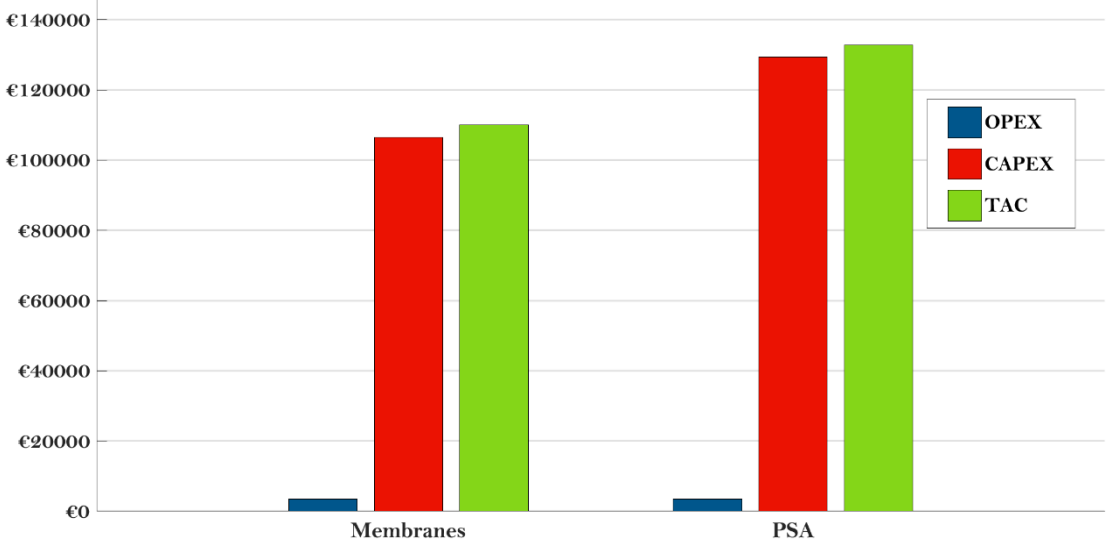


Figure 6.6: Economic comparison of PSA and Membrane-based separation technologies considering OPEX, CAPEX and TAC.

For both technologies, the Total Annualized Costs (TAC) are primarily driven by capital expenditures (CAPEX), while electricity consumption constitutes a relatively minor portion of the overall expense. The analysis reveals that, under equivalent product specifications, membrane-based separation emerges as the more convenient process since entails lower annual costs (110,008.31 €/year) compared to the PSA process (132,735.95 €/year).

Breaking down the total annualised costs (TAC), Figure 6.7 clearly illustrates the cost distribution across the different components for both PSA and membrane technologies. In the PSA case, columns and vacuum pumps represent most of the expenses, together amounting to a value comparable to the entire capital cost of the membrane system. The main factors that make PSA more expensive overall are the costs related to the adsorbent and switching valves. On the other hand, in the membrane process, Membrane 1 and Membrane 2 dominate the cost distribution, followed by the vacuum pumps and compressor. Notably, the OPEX remains relatively similar between the two technologies, suggesting that the difference in TAC is primarily due to capital expenditures. This highlights that PSA is a more capital-intensive option than membrane-based separation under the given conditions.

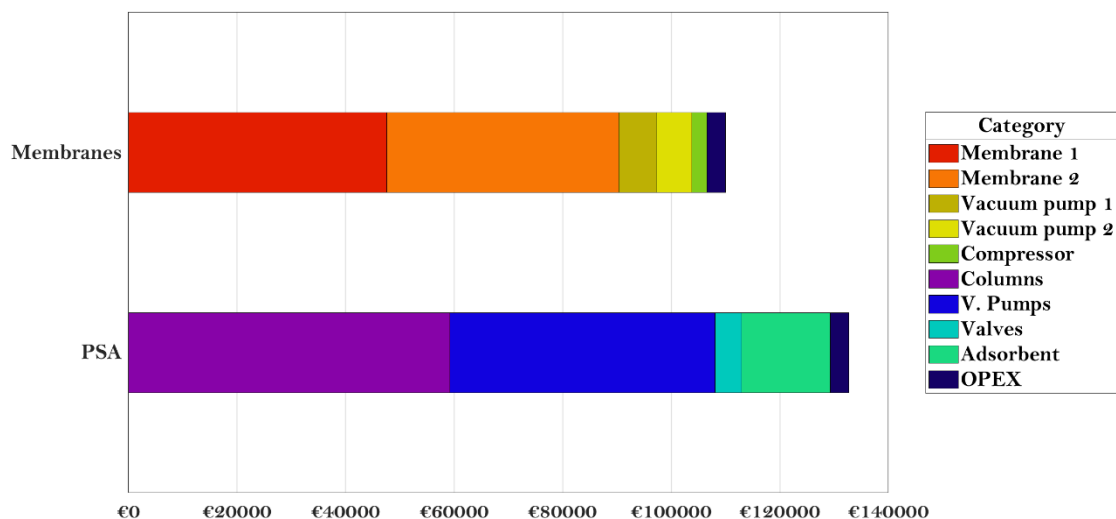


Figure 6.7: Breakdown of the total annualized costs for membrane and PSA. Each equipment is considered in the capital expenses. The OPEX is summarized under a single voice which consider the electricity consumption of the process.

Furthermore, it is possible to evaluate how the cost of hydrogen production changes with the addition of CO₂ capture in the SYPOX plant. It is important to underline that the installation of a CO₂ capture technology, while improving hydrogen recovery and overall process productivity, negatively impacts the Hydrogen Production Cost (HPC).

Table 6.13: HPC with and without the carbon capture. The CAPEX and OPEX are referred to the entire SYPOX plant.

Parameter	CO ₂ capture technology		
	None	PSA	Membranes
Hydrogen recovery [%]	82	98.5	97.7
Hydrogen productivity [kg/h]	9.1	10.91	10.83
Annualized CAPEX [k€]	246	355.3	352.5
CAPEX impact on TAC [%]	52	64	59
OPEX impact on TAC [%]	48	36	41
HPC [€/kgH₂]	7.05	7.69	7.46

This increase is primarily attributed to the high capital expenditure associated with carbon capture systems, which significantly raises overall production costs. When comparing PSA and membrane-based separation in this context, membrane technology emerges as the more cost-effective option, resulting in a lower HPC.

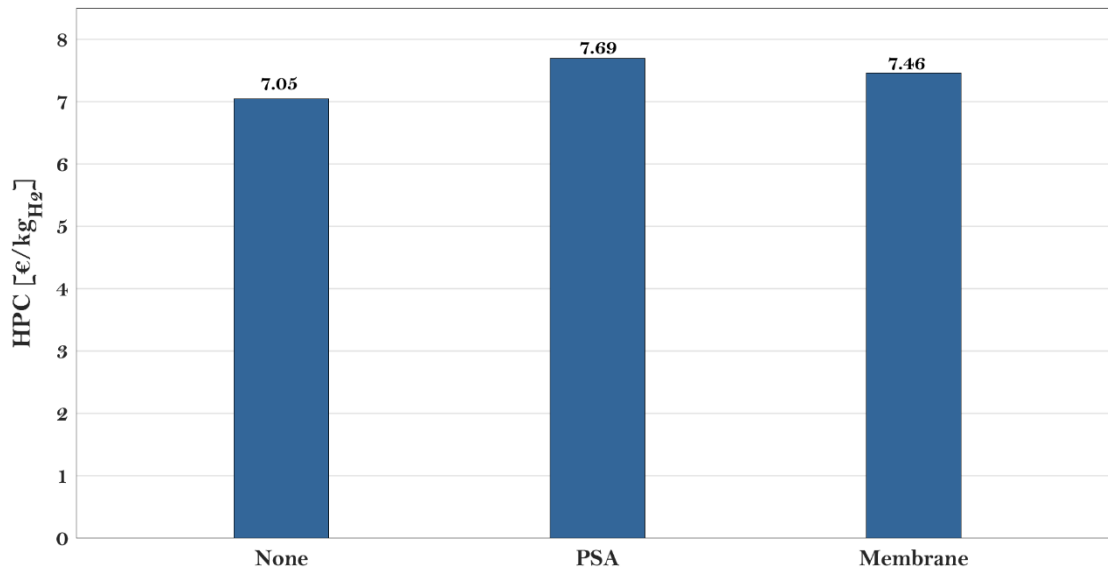


Figure 6.8: Hydrogen production cost of the SYPOX plant without carbon capture compared with the cases of carbon capture using PSA or membranes.

The other important factor to analyse with the adoption of the CO₂ capture technologies in the plant is the carbon footprint. Focusing on the direct CO₂ emissions, Table 6.14 shows that the values become negative when carbon capture technologies are applied.

Table 6.14: Parameters necessary to calculate the carbon footprint of the plant with and without CO₂ capture technologies.

<i>Parameter</i>	<i>CO₂ capture technology</i>		
	<i>None</i>	<i>PSA</i>	<i>Membrane</i>
<i>Plants electricity consumption [kW]</i>	180	224.2	204
<i>Direct CO₂ emissions [kg/h]</i>	62.5	-57.5	-44.5
<i>Hydrogen productivity [kg/h]</i>	9.1	10.91	10.82

This indicates that the CO₂ generated from biogas processing is offset by the CO₂ absorbed during biomass growth through photosynthesis. By implementing CCS, the captured CO₂ effectively corresponds to atmospheric removal, rendering the overall process carbon negative. It must be noted that considering the carbon footprint, PSA emerges as the better technologies. The lower direct CO₂ emissions observed in the PSA process compared to the membrane-based separation are primarily due to the point in the process where carbon capture is applied. Both technologies generate a secondary gas stream—raffinate in PSA and retentate in membrane separation—that contains unseparated gases and must be partially purged to the flare. However, in the membrane configuration, this purge stream is larger. This is because, although a recycle is implemented in both cases towards the PSA hydrogen purification unit, the membrane-based capture is placed upstream of the hydrogen purification. As a result, the process with the membrane CO₂ capture skips one purification step, leading to a greater volume of off-gas in the stream that ultimately must be flared. In contrast, the process with PSA carbon capture allows

for partial raffinate recycling directly within the PSA system, reducing the volume of vented gases and thus the associated CO₂ emissions.

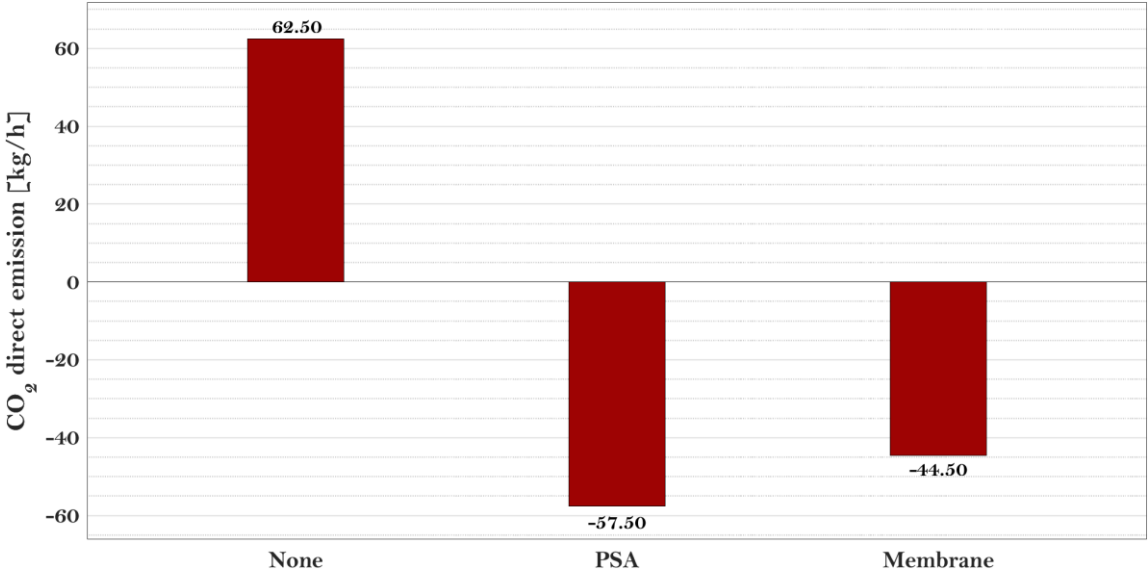


Figure 6.9: CO₂ direct emissions without carbon capture compared with the case of carbon capture using PSA or membranes.

Table 6.15 resume the data shown in section 1.6.3 to compare different site to locate the decentralized e-SMR plants and add the variation that occurs to the carbon footprint if the carbon capture with membrane or PSA is applied. The table highlights how the environmental impact of decentralized hydrogen production varies significantly depending on the country and the use of carbon capture technologies.

Table 6.15: *Hydrogen carbon footprint from electrified biogas reforming with and without carbon capture for different plant location (electricity mix).*

Plant location	Carbon capture technique	Direct emissions [kg_{CO2} /kg H₂]	Indirect emission from electricity [kg_{CO2} /kgH₂]	Total emissions [kg_{CO2} /kgH₂]	Reduction vs centralized SMR [%]
Italy					
	None	6.88	5.51	12.39	+37.6
	PSA	-5.27	5.44	0.17	-98.1
	Membranes	-4.11	4.99	0.88	-90.2
Germany					
	None	6.88	6.24	13,12	+45.7
	PSA	-5.27	6.16	0.89	-90.1
	Membranes	-4.11	5.65	1.54	-82.8
France					
	None	6.88	0.62	7.5	-16,6
	PSA	-5.27	0.61	-4.66	-151.7
	Membranes	-4.11	0.565	-3.54	-139.3

The use of carbon capture technologies, especially Pressure Swing Adsorption (PSA), drastically reduces total emissions in all countries, with France even achieving negative net emissions, meaning more CO₂ is captured than released. Overall, PSA outperforms membrane-based systems, and the effectiveness of decentralized hydrogen production in reducing emissions depends strongly on both the electricity source and the implementation of carbon capture. However also the adoption of a membrane-based CO₂ capture guarantees good result in terms of carbon footprint.

Conclusions

The aim of this thesis was to carry out a techno-economic assessment of two CO₂ capture technologies—Pressure Swing Adsorption (PSA) and membrane gas separation—when integrated into a decentralized hydrogen production plant powered by biogas and based on electrified Steam Methane Reforming (e-SMR). The primary objective was to determine which of the two options is more economically advantageous by comparing the Hydrogen Production Cost (HPC) of the plant under each scenario. In addition, the study evaluates the impact of each technology on the carbon footprint, providing insight into how the integration of carbon capture affects the environmental sustainability of the process. From a technical standpoint, the first key decision was to determine the optimal location for integrating the CO₂ capture technologies. Two options were considered: placing the capture unit downstream of the PSA hydrogen purification unit of the SYPOX process or using the syngas stream exiting the low-temperature shift reactor as the feed. Feed pressure played a decisive role in this choice. For PSA-based CO₂ capture, a desorption step under vacuum is typically required, making it more convenient to use a low-pressure feed stream, such as the tail gas from PSA hydrogen purification, which is at atmospheric pressure. In contrast, membrane-based separation benefits from a high feed pressure, as a significant pressure gradient across the membrane enhances separation performance. Therefore, in the case of membrane technology, the syngas stream at 10 bar was selected as the feed for the CO₂ capture unit. The requirements of purity and recovery are then chosen. The carbon capture aims to obtain a high-pure stream of CO₂, to respect environmental constraints to be able to store the carbon dioxide. For that reason, the requirement of purity is of 99% while the recovery is fixed at 90%.

The first technique analysed is the PSA. Chapter 4 presented the detailed design and dynamic simulation of a PSA unit. A vacuum swing cycle with five synchronized columns was developed to treat the PSA tail gas stream. Zeolite 13X was chosen as the adsorbent due to its high CO₂ selectivity and favourable regeneration properties. The vacuum grade is reached by four vacuum pumps which leads the column to a sub atmospheric pressure of 0.05 bar. A rigorous column sizing approach was then implemented, combining equilibrium calculations, mass transfer modelling, and simulation of the adsorption front. The model accounted for non-idealities such as the mass transfer zone and thermal effects, resulting in a column which has the size of 0.98 height and 0.304 diameter.

Chapter 5 focused on membrane-based CO₂ capture. A polymeric PEBAX–PG membrane was selected due to its favourable CO₂ permeability and selectivity. A crossflow model with the perfect mixing assumption was used to design a two-stage. To increase the driving force given by the partial pressures of the permeable component, a vacuum pump was used in the permeate side of both membranes to reach a grade of vacuum of 0.5 bar. After the first vacuum pump a

compressor is placed to increase again the pressure to 10 bar and consequently the driving force. A single-stage configuration was also tried to be applied for the capture, but the requirements of purity and recovery was not satisfied. The two membrane was found to have an area equal to 710 m² for the first and 630.88 m² for the second.

Chapter 6 presents a comparative economic analysis of the two CO₂ capture technologies. The PSA system exhibits higher capital costs, primarily due to the vacuum pumps and the need for adsorbent replacement. In both technologies, the operating expenses (OPEX) are mainly attributed to the electricity consumption of the equipment required for separation. However, the OPEX for membranes and PSA is comparable, contributing only 3% to the Total Annualised Cost (TAC) in each case. Compared to the PSA technology (7.69 €/kg_{H2}), the Hydrogen Production Cost (HPC) is lower when applying the membrane-based separation (7.46 €/kg_{H2}), owing to its lower capital expenditure. Nevertheless, the integration of carbon capture technologies results in an overall increase in HPC compared to the base case without CO₂ capture (7.05 €/kg_{H2}). This is due to the significant investment required for implementing the capture units, which outweighs the gain in hydrogen productivity. What is better decreased is the carbon footprint of the plant if a CO₂ capture technique is applied. It is defined as kg of CO₂ emitted over kg of H₂ produced. This value is lower if PSA is applied since the location in the plant using the tail gas as a feed stream allows to purge a lower amount of gases.

The final evaluation highlighted that technology selection depends on trade-offs between cost, purity, recovery, and integration constraints Both systems proved viable for decentralized CO₂ capture, each offering distinct advantages aligned with specific process goals and design priorities.

Appendices

Appendix A: Assumptions for the development of the techno-economic analysis.

In this section there will summarize the assumptions made to carry out the techno economic analysis including the PSA column sizing, the proper area calculation of the membrane-based separation and the economic analysis. The first table include the assumptions used for the column sizing.

Table A.1: Assumption for the column design step to find the equilibrium height

<i>Assumption</i>	<i>Reference</i>
Binary mixture (H ₂ +CO ₂)	Simplification justified by the low content of the other components in the feed stream (~ 3%)
Ideal gas mixture	Equilibrium theory (Shendalman and Mitchell, 1972). Comparison of IG model with the PR and SRK thermodynamic model assesses the feasibility.
Isothermal assumption	Equilibrium theory (Shendalman and Mitchell, 1972)
Pressure drops calculated with the Ergun equation	(Perry, 2018)
Velocity of the gas mixture considered constant at the feed value.	(Gas processor suppliers, 2004)
Diameter calculation from maximum velocity	(Gas processor suppliers, 2004)
Mass calculation using isotherm loading (eq. 4.8)	How to guide (Knaebel, 1992)
Equilibrium height calculation	How to guide (Knaebel, 1992)

Table A.2: Assumption made during the dynamic simulation of the adsorption step.

<i>Assumption</i>	<i>Reference</i>
Binary mixture (H ₂ +CO ₂)	Simplification justified by the low content of the other components in the feed stream (~ 3%)
Ideal gas mixture	Equilibrium theory (Shendalman and Mitchell, 1972).
Properties of the mixture taken as constant and at the feed values.	(Schmidt, 2005)
Equilibrium behaviour described by the Langmuir model	(Ruthven, 1994)
Plug flow model	(Yang, 1987)
Negligible axial dispersion	(Ruthven, 1984)
Only CO ₂ is adsorbed	Simplification justified by the low extent of H ₂ loading in zeolite 13X. Helps to reduce computational times.
LDF for kinetic limitations	(Ruthven, 1984)

Table A.3: Assumption made during the calculation of the membrane's areas.

<i>Assumption</i>	<i>Reference</i>
Binary mixture (H ₂ +CO ₂)	Simplification justified by the low content of the other components in the feed stream (~ 3%)
Ideal gas mixture	(Baker, 2012) Comparison of IG model with the PR and SRK thermodynamic model assesses the feasibility.
Isothermal assumption	(Baker, 2012)
Cross flow model	(Weller and Steiner, 1950)
Perfect mixing in the membrane	(Weller and Steiner, 1950)

Table A.4: Assumption made to perform the economic analysis.

<i>Assumption</i>	<i>Reference</i>
Capital cost described summing the Bare erected cost of each equipment of the plant.	(NETL., 2011)
Interest rate for capital costs (ACCR)	(Turton et al., 2018)
Electricity price (0.08 €/kWh).	Reference value used in SYPOX economic analysis
BEC for columns, vacuum pumps, switching valves adsorbent and compressor.	(Subraveti et al., 2020)
PEBAX® /PG of hollow fibre modules material price (150 €/m ²)	(Arias et al., 2016)
Vacuum pumps power consumption in PSA	(Subraveti et al., 2020)

Appendix B: Comparison of PSA and membrane CO₂ with absorption using hot potassium carbonate.

In this section are compared the CO₂ capture technologies analysed in the thesis with a technique placed in the SYPOX plant, using syngas as feed stream. The technique concerns the use of a solution of water and hot potassium carbonate to perform a chemical absorption of CO₂. The results are compared in terms of hydrogen production cost and carbon footprint.

Table B.1: HPC with and without the carbon capture. The CAPEX and OPEX are referred to the entire SYPOX plant.

<i>Parameter</i>	<i>CO₂ capture technology</i>			
	<i>None</i>	<i>PSA</i>	<i>Membranes</i>	<i>Absorption</i>
<i>Hydrogen recovery [%]</i>	82	98.5	97.7	98.9
<i>Hydrogen productivity [kg/h]</i>	9.1	10.91	10.83	10.96
<i>Annualized CAPEX [k€]</i>	246	355.3	352.5	302.4
<i>CAPEX impact on TAC [%]</i>	52	64	59	42
<i>OPEX impact on TAC [%]</i>	48	36	41	58
<i>HPC [€/kg_{H2}]</i>	7.05	7.69	7.46	7.50

Table B.2: Parameters necessary to calculate the carbon footprint of the plant with and without CO₂ capture technologies.

<i>Parameter</i>	<i>CO₂ capture technology</i>			
	<i>None</i>	<i>PSA</i>	<i>Membrane</i>	<i>Absorption</i>
<i>Plants electricity consumption [kW]</i>	180	224.2	204	377
<i>Direct CO₂ emissions [kg/h]</i>	62.5	-57.5	-44.5	-48.5
<i>Hydrogen productivity [kg/h]</i>	9.1	10.91	10.82	10.96

Table B.3: *Hydrogen carbon footprint from electrified biogas reforming with and without carbon capture for different plant location (electricity mix).*

Plant location	Carbon capture technique	Direct emissions [kg_{CO2} /kg H₂]	Indirect emission from electricity [kg_{CO2} /kg_{H2}]	Total emissions [kg_{CO2} /kg_{H2}]	Reduction vs centralized SMR [%]
Italy					
	None	6.88	5.51	12,39	+37,6
	PSA	-5.27	5.44	0.17	-98.1
	Membranes	-4.11	4.99	0.88	-90.2
	Absorption	-4.30	8.87	4.57	-49.27
Germany					
	None	6.88	6.24	13,12	+45,7
	PSA	-5.27	6.16	0.89	-90.1
	Membranes	-4.11	5.65	1.54	-82.8
	Absorption	-4.30	10.04	5.75	-36.16
France					
	None	6.88	0,62	7.5	-16,6
	PSA	-5.27	0.61	-4.66	-151.7
	Membranes	-4.11	0.565	-3.54	-139.3
	Absorption	-4.30	1.00	-3.28	-136.46

Bibliographic references

Introduction

- Intergovernmental Panel on Climate Change (IPCC). (2018). Global Warming of 1.5°C. <https://www.ipcc.ch/sr15/>
- U.S. Environmental Protection Agency. (n.d.). *Overview of Greenhouse Gases*. Retrieved from <https://www.epa.gov/ghgemissions/overview-greenhouse-gases>
- Keeling, C.D. (1960), The Concentration and Isotopic Abundances of Carbon Dioxide in the Atmosphere. *Tellus*, 12: 200-203. <https://doi.org/10.1111/j.2153-3490.1960.tb01300.x>
- Ritchie, H., & Roser, M. (2020). *CO₂ and Greenhouse Gas Emissions*. *Our World in Data*. <https://ourworldindata.org/co2-emissions>
- National Grid. (n.d.). *What is Carbon Capture and Storage (CCS) and how does it work?* <https://www.nationalgrid.com/stories/energy-explained/what-is-ccs-how-does-it-work>

Chapter 1

- IEA (2019), *The Future of Hydrogen*, IEA, Paris <https://www.iea.org/reports/the-future-of-hydrogen>, Licence: CC BY 4.0
- Ming, Q., et al. (2002). *Steam reforming of hydrocarbon fuels*. *Catalysis Today*, 77(1–2), 51–64. *Fuel and Energy Abstracts*, 44(4), 220. [https://doi.org/10.1016/S0140-6701\(03\)82857-6](https://doi.org/10.1016/S0140-6701(03)82857-6)
- IEA (2024), *Global Hydrogen Review 2024*, IEA, Paris <https://www.iea.org/reports/global-hydrogen-review-2024>, Licence: CC BY 4.0
- El-Shafie, M. (2023). *Hydrogen production by water electrolysis technologies: A review*. *Results in Engineering*, 18, 101426. <https://doi.org/10.1016/j.rineng.2023.101426>
- Tahmasbi, M., Siavashi, M., & Ahmadi, R. (2025). *A comprehensive review of hydrogen production and storage methods: Fundamentals, advances, and SWOT analysis*. *Energy Conversion and Management*: X, 26, 101005. <https://doi.org/10.1016/j.ecmx.2025.101005>
- Rostrup-Nielsen, J. R., Sehested, J., & Nørskov, J. K. (2002). Hydrogen and synthesis gas by steam- and CO₂ reforming. *Advances in Catalysis*, 47, 65–139. [https://doi.org/10.1016/S0360-0564\(02\)47005-X](https://doi.org/10.1016/S0360-0564(02)47005-X)

- Towler, G., & Sinnott, R. (2013). *Chemical engineering design: Principles, practice and economics of plant and process design* (2nd ed.). Elsevier.
- S.T. Wismann, J.S. Engbaek, S.B. Vendelbo, F.B. Bendixen, W.L. Eriksen, K. Aasberg-Petersen, C. Frandsen, I. Chorkendorff, P.M. Mortensen, Electrified methane reforming: a compact approach to greener industrial hydrogen production, *Science* 364 (2019) (1979) 756–759, <https://www.science.org>.
- Wismann, S. T., Engbæk, J. S., Vendelbo, S. B., Eriksen, W. L., Frandsen, C., Mortensen, P. M., & Chorkendorff, I. (2019). Electrified methane reforming: Understanding the dynamic interplay. *Nature Energy*, 4(10), 845–852.
- Pauletto, G. (2021). *A reactor with an electrically heated structured ceramic catalyst* (European Patent Application No. EP 3 895 795 A1). European Patent Office.
- Maporti, D., Guffanti, S., Galli, F., Mocellin, P., & Pauletto, G. (2024). Towards sustainable hydrogen production: Integrating electrified and convective steam reformer with carbon capture and storage. *Chemical Engineering Journal*, 499, 156357. <https://doi.org/10.1016/j.cej.2024.156357>
- Khatib, S. J., Baskaralingam, P., Pandey, A., & Pandey, R. A. (2022). Recent developments in methane steam reforming: A review on performance improvement using various reactors and catalysts. *International Journal of Hydrogen Energy*, 47(4), 2686–2716. <https://doi.org/10.1016/j.ijhydene.2021.10.217>
- International Energy Agency. (2024). *Electricity 2024: Analysis and forecast to 2026*. <https://iea.blob.core.windows.net/assets/0f028d5f-26b1-47ca-ad2a-5ca3103d070a/Electricity2025.pdf>
- Hydrogen Council. (2023). *Hydrogen Insights – December Update*. <https://hydrogencouncil.com/en/hydrogen-insights-2023-december-update>
- EPA (2014). EPA issues final rule for renewable fuel standard (RFS) pathways II and modifications to the RFS program, ultra-low sulfur diesel requirements, and E15 misfuelling mitigation requirements, U.S.E.P. Agency, ed.. <https://nepis.epa.gov/Exe/ZyPDF.cgi?Dockkey=P100JPPP.pdf>.
- Anastas, P. T., & Warner, J. C. (1998). *Green Chemistry: Theory and Practice*. Oxford University Press.
- Zhao, X., Joseph, B., Kuhn, J., & Ozcan, S. (2020). Biogas Reforming to Syngas: A Review. *iScience*, 23(5), 101082. <https://doi.org/10.1016/j.isci.2020.101082>
- Mao, C., Feng, Y., Wang, X., & Ren, G. (2015). Review on research achievements of biogas from anaerobic digestion. *Renewable and Sustainable Energy Reviews*, 45, 540–555. <https://doi.org/10.1016/j.rser.2015.02.032>
- Adekunle, K. F., & Okolie, J. A. (2015). A review of biochemical process of anaerobic digestion. *Advances in Bioscience and Biotechnology*, 6(3), 205–212. <https://doi.org/10.4236/abb.2015.63020>

- Zhao, X., Joseph, B., Kuhn, J., & Ozcan, S. (2020). *Biogas Reforming to Syngas: A Review*. *iScience*, 23(5), 101082. <https://doi.org/10.1016/j.isci.2020.101082>
- International Energy Agency. (2020). *Outlook for Biogas and Biomethane: Prospects for Organic Growth*. https://iea.blob.core.windows.net/assets/03aeb10c-c38c-4d10-bcec-de92e9ab815f/Outlook_for_biogas_and_biomethane.pdf
- REN21. (2023). *Renewables 2023 Global Status Report: Bioenergy Market Developments*. https://www.ren21.net/gsr2023/modules/energy_supply/02_market_developments/01_bioenergy/
- Rochelle, G. T. (2009). *Amine scrubbing for CO₂ capture*. *Science*, 325(5948), 1652–1654. <https://doi.org/10.1126/science.1176731>
- IEA (2021), About CCUS, IEA, Paris <https://www.iea.org/reports/about-ccus>, Licence: CC BY 4.0
- United States Department of Energy. (n.d.). Pre-Combustion Carbon Capture Research. Retrieved May 16, 2025, from <https://www.energy.gov/fecm/pre-combustion-carbon-capture-research>
- Hua, W., Sha, Y., Zhang, X., & Cao, H. (2023). *Research progress of carbon capture and storage (CCS) technology based on the shipping industry*. *Ocean Engineering*, 281, 114929. <https://doi.org/10.1016/j.oceaneng.2023.114929>
- National Energy Technology Laboratory (NETL). (n.d.). *Carbon Dioxide Capture Technology Options*. U.S. Department of Energy. Retrieved from <https://netl.doe.gov/>
- Chao, C., Y. Deng, R. Dewil, J. Baeyens and X. Fan (2021). Post-combustion carbon capture. *Renewable and Sustainable Energy Reviews*, 138. <https://doi.org/10.1016/j.ccst.2023.100125>
- Khan, U., Ogbaga, C. K., Abiodun, O. A. O., Adeleke, A. A., Ikubanni, P. P., Okoye, P. U., & Okolie, J. A. (2023). Assessing absorption-based CO₂ capture: Research progress and techno-economic assessment overview. *Carbon Capture Science & Technology*, 3, 100125. <https://doi.org/10.1016/j.ccst.2023.100125>
- Bashir, A., Ali, M., Patil, S., Aljawad, M. S., Mahmoud, M., Al-Shehri, D., Hoteit, H., & Kamal, M. S. (2024). *Comprehensive review of CO₂ geological storage: Exploring principles, mechanisms, and prospects*. *Earth-Science Reviews*, 249, 104672. <https://doi.org/10.1016/j.earscirev.2023.104672>
- IEAGHG. (2010). *Summary report of the IEAGHG workshop – Natural releases of CO₂: Building knowledge for CO₂ storage environmental impact assessments* (2–3 November 2010, Maria Laach, Germany). IEA Greenhouse Gas R&D Programme. https://publications.ieaghg.org/docs/General_Docs/Reports/2011-03.pdf

- Maporti D., Nardi R., Guffanti S., Vianello C., Mocellin P., Pauletto G., 2022, Techno-economic Analysis of Electrified Biogas Reforming, *Chemical Engineering Transactions*, 96.

Chapter 2

- Shah, G., Ahmad, E., Pant, K. K., & Vijay, V. K. (2021). *Comprehending the contemporary state of art in biogas enrichment and CO₂ capture technologies via swing adsorption*. *International Journal of Hydrogen Energy*, 46(5), 6588–6612. <https://doi.org/10.1016/j.ijhydene.2020.11.116>
- Ruthven, D. M. (1984). *Principles of adsorption and adsorption processes*.
- Ruthven, D. M., Farooq, S., & Knaebel, K. S. (1994). *Pressure swing adsorption*.
- Pourhakkak, P., Taghizadeh, A., Taghizadeh, M., Ghaedi, M., & Haghdoost, S. (2021). *Fundamentals of adsorption technology*. In *Interface Science and Technology* (Vol. 33). Elsevier. <https://doi.org/10.1016/B978-0-12-818805-7.00001-1>
- Islam, M. A., Khan, M. R., & Mezaumder, M. S. I. (2004). *Adsorption equilibrium and adsorption kinetics: A unified approach*. *Chemical Engineering & Technology*, 27(10), 1055–1060. <https://doi.org/10.1002/ceat.200407077>
- Brauner, J. C., Deming, W. E., Deming, E. W., & Teller, E. (1940). *A theory of adsorption of gases by solids*. *Journal of the American Chemical Society*, 62(8), 2133–2138. <https://doi.org/10.1021/ja01865a030>
- Langmuir, I. (1918). *The adsorption of gases on plane surfaces of glass, mica and platinum*. *Journal of the American Chemical Society*, 40(9), 1361–1403. <https://doi.org/10.1021/ja02242a004>
- Yang, R. T. (1987). *Gas separation by adsorption processes*.
- Skarstrom, C. W. (1960). *Method and apparatus for fractionating gaseous mixtures by adsorption* (U.S. Patent No. 2,944,627). United States Patent and Trademark Office. <https://patents.google.com/patent/US2944627A>
- Quaranta, I. C. C., Pinheiro, L. S., Gonçalves, D. V., Peixoto, H. R., & Lucena, S. M. P. (2021). *Multiscale design of a pressure swing adsorption process for natural gas purification*. *Adsorption*, 27, 1055–1066. <https://doi.org/10.1007/s10450-021-00330-y>
- Flowserve. *Pressure swing adsorption in oil & gas*. Retrieved from <https://www.flowserve.com/en/industries/oil-gas/pressure-swing-adsorption/>
- Guérin de Montgareuil, P., Domine, D., & Claude, G. (1964). *Process for separating a binary gaseous mixture by adsorption* (U.S. Patent No. 3,155,468). United States Patent and Trademark Office.

- Schmidt, L. D. (2005). *The engineering of chemical reactions* (2nd ed.). Oxford University Press.
- Perry, R. H., Green, D. W., & Maloney, J. O. (Eds.). (2018). *Perry's Chemical Engineers' Handbook* (9th ed.). McGraw-Hill Education.

Chapter 3

- Lu, G. Q., Diniz da Costa, J. C., Duke, M., Giessler, S., Socolow, R., Williams, R. H., & Kreutz, T. (2007). *Inorganic membranes for hydrogen production and purification: A critical review and perspective*. *Journal of Colloid and Interface Science*, 314(2), 589–603. <https://doi.org/10.1016/j.jcis.2007.05.067>
- Baker, R. W. (2012). *Membrane technology and applications* (3rd ed.). John Wiley & Sons. <https://doi.org/10.1002/9781118359686>
- Odani, H., & Uyeda, T. (1991). *Theories of sorption and transport in polymer membranes*. *Polymer Journal*, 23(5), 467–479. <https://doi.org/10.1295/polymj.23.467>
- Baker, R. W., & Low, B. T. (2014). *Gas separation membrane materials: A perspective*. *Macromolecules*, 47(20), 6999–7013. <https://doi.org/10.1021/ma501138z>
- Duthie, X., Kentish, S., Powell, C., Nagai, K., Qiao, G., Stevens, G., 2007b. Operating temperature effects on the plasticization of polyimide gas separation membranes. *J. Membr. Sci.* 294, 40–49.
- Orme, C.J., Stone, M.L., Benson, M.T., Peterson, E.S., 2003. Testing of polymer membranes for the selective permeability of hydrogen. *Sep. Sci. Technol.* 38, 3225–3238.
- Lin, H., Freeman, B.D., 2004. Gas solubility, diffusivity and permeability in poly(ethylene oxide). *J. Membr. Sci.* 239, 105–117.
- Bondar, V.I., Freeman, B.D., Pinnau, I., 2000. Gas transport properties of poly(ether-b-amide) segmented block copolymers. *J. Polym. Sci. B: Polym. Phys.* 38, 2051–2062.
- Baker, R. W., & Wijmans, J. G. (1994). *Membrane separation of organic vapors from gas streams*. In D. R. Paul & Y. P. Yampolskii (Eds.), *Polymeric gas separation membranes* (pp. 353–398). CRC Press.
- Fan, Y., Yu, W., Wu, A., Shu, W., & Zhang, Y. (2024). *Recent progress on CO₂ separation membranes*. *RSC Advances*, 14(20), 20714–20754. <https://doi.org/10.1039/d4ra00444b>
- Quinn, R., Appleby, J.B., Pez, G.P., 1995. New facilitated transport membranes for the separation of carbon dioxide from hydrogen and methane. *J. Membr. Sci.* 104, 139–146.
- Quinn, R., Laciak, D.V., 1997. Polyelectrolyte membranes for acid gas separation. *J. Membr. Sci.* 131, 49–60.

- Myers, C., Pennline, H., Luebke, D., Ilconich, J., Dixon, J.K., Maginn, E.J., Brennecke, J.F., 2008. High temperature separation of carbon dioxide/hydrogen mixtures using facilitated supported ionic liquid membranes. *J. Membr. Sci.* 322, 28–31
- Bai, H., Ho, W.S.W., 2009. New carbon dioxide-selective membranes based on sulfonated polybenzimidazole (SPBI) copolymer matrix for fuel cell applications. *Ind. Eng. Chem. Res.* 48, 2344–2354.
- Scholes, C. A., Smith, K. H., Kentish, S. E., & Stevens, G. W. (2010). *CO₂ capture from pre-combustion processes—Strategies for membrane gas separation*. *International Journal of Greenhouse Gas Control*, 4(5), 739–755. <https://doi.org/10.1016/j.ijggc.2010.04.001>

Chapter 4

- Liu, B., Yu, X., Shi, W., Shen, Y., Zhang, D., & Tang, Z. (2020). *Two-stage VSA/PSA for capturing carbon dioxide (CO₂) and producing hydrogen (H₂) from steam-methane reforming gas*. *International Journal of Hydrogen Energy*, 45(34), 24870–24882. <https://doi.org/10.1016/j.ijhydene.2020.06.264>
- Liu, Z., Grande, C. A., Li, P., Yu, J., & Rodrigues, A. E. (2011). Multi-bed vacuum pressure swing adsorption for carbon dioxide capture from flue gas. *Separation and Purification Technology*, 81, 307–317. <https://doi.org/10.1016/j.seppur.2011.07.007>
- Subraveti, S. G., Roussanaly, S., Anantharaman, R., Riboldi, L., & Rajendran, A. (2021). *Techno-economic assessment of optimised vacuum swing adsorption for post-combustion CO₂ capture from steam-methane reformer flue gas*. *Separation and Purification Technology*, 256, 117882. <https://doi.org/10.1016/j.seppur.2020.117882>
- M.T. Ho, G.W. Allinson, D.E. Wiley, Reducing the cost of CO₂ capture from flue gases using pressure swing adsorption, *Ind. Eng. Chem. Res.* 47 (2008) 4883–4890.
- N. Susarla, R. Haghpanah, I. Karimi, S. Farooq, A. Rajendran, L.S.C. Tan, J.S.T. Lim, Energy and cost estimates for capturing CO₂ from a dry flue gas using pressure/vacuum swing adsorption, *Chem. Eng. Res. Des.* 102 (2015) 354–367.
- M. Khurana, S. Farooq, Integrated adsorbent process optimization for minimum cost of electricity including carbon capture by a VSA process, *AIChE J.* 65 (2019) 184–195.
- Gholami, M., Schoukens, M., Van Assche, T. R. C., & Denayer, J. F. M. (2024). *Improving energy estimation in VSA processes through integration of vacuum pump characteristics: A carbon capture case study*. *Separation and Purification Technology*, 343, 127140. <https://doi.org/10.1016/j.seppur.2024.127140>

- Cavenati, S., Grande, C. A., & Rodrigues, A. E. (2004). Adsorption equilibrium of methane, carbon dioxide, and nitrogen on zeolite 13X at high pressures. *Journal of Chemical & Engineering Data*, 49(4), 1095–1101.
- Kumar, A., Madden, D. G., Lusi, M., Chen, K. J., Daniels, E. A., Curtin, T., & Zaworotko, M. J. (2015). Direct air capture of CO₂ by physisorbent materials. *Angewandte Chemie*, 127(48), 14501–14505.
- Gas Processors Suppliers Association. (2004). *Engineering data book: FPS version, volumes I & II, sections 1–26* (12th ed.). Gas Processors Suppliers Association.
- Knaebel, K. S. (n.d.). A “How To” guide for adsorber design. Adsorption Research, Inc.
- Kohl, A. L., & Nielsen, R. B. (1997). *Gas purification* (5th ed.). Gulf Professional Publishing.
- Williamson, J. E., Bazaire, K. E., & Geankoplis, C. J. (1963). *Gas absorption at low Reynolds numbers in packed beds. Industrial & Engineering Chemistry Fundamentals*, 2(2), 126–129. <https://doi.org/10.1021/i160007a010>
- Bird, R. B., Stewart, W. E., & Lightfoot, E. N. (2002). *Transport phenomena* (2nd ed.). John Wiley & Sons.

Chapter 5

- Abetz, V., Brinkmann, T., & Sözbilir, M. (2021). *Fabrication and function of polymer membranes. Chemistry Teacher International*, 3(2), 141–154. <https://doi.org/10.1515/cti-2020-0023>
- Weller, S., & Steiner, W. A. (1950). *Separation of gases by fractional permeation through membranes. Industrial & Engineering Chemistry*, 42(4), 278–283. <https://doi.org/10.1021/ie50483a012>
- Geankoplis, C. J. (1993). *Transport processes and unit operations* (3rd ed.). Prentice Hall.
- Baker, R. W. (2012). *Membrane technology and applications* (3rd ed.). John Wiley & Sons. <https://doi.org/10.1002/9781118359686>
- Franz, J., & Scherer, V. (2010). *An evaluation of CO₂ and H₂ selective polymeric membranes for CO₂ separation in IGCC processes. Journal of Membrane Science*, 359(1–2), 173–183. <https://doi.org/10.1016/j.memsci.2010.01.047>
- Vallières, C., & Favre, E. (2004). *Vacuum versus sweeping gas operation for binary mixtures separation by dense membrane processes. Journal of Membrane Science*, 244(1–2), 17–23. <https://doi.org/10.1016/j.memsci.2004.04.017>
- Scholes, C. A., Smith, K. H., Kentish, S. E., & Stevens, G. W. (2010). *CO₂ capture from pre-combustion processes—Strategies for membrane gas separation. International*

References for chapter 6

- NETL, Quality guidelines for energy system studies: Cost estimation methodology for NETL assessments of power plant performance, 2011, <http://pDOE/NETL-2011/1455>.
- Haaf, M., Anantharaman, R., Roussanaly, S., Ströhle, J., & Epple, B. (2020). CO₂ capture from waste-to-energy plants: Techno-economic assessment of novel integration concepts of calcium looping technology. *Resources, Conservation and Recycling*, 162, 104973. <https://doi.org/10.1016/j.resconrec.2020.104973>
- Susarla, N., Haghpanah, R., Karimi, I., Farooq, S., Rajendran, A., Tan, L. S. C., & Lim, J. S. T. (2015). *Energy and cost estimates for capturing CO₂ from a dry flue gas using pressure/vacuum swing adsorption*. *Chemical Engineering Research and Design*, 102, 354–367. <https://doi.org/10.1016/j.cherd.2015.06.004>
- Danaci, D., Bui, M., Mac Dowell, N., & Petit, C. (2020). *Exploring the limits of adsorption-based CO₂ capture using MOFs with PVSA — From molecular design to process economics*. *Molecular Systems Design & Engineering*, 5(1), 212–231. <https://doi.org/10.1039/C9ME00109F>
- Subraveti, S. G., Roussanaly, S., Anantharaman, R., Riboldi, L., & Rajendran, A. (2021). *Techno-economic assessment of optimised vacuum swing adsorption for post-combustion CO₂ capture from steam-methane reformer flue gas*. *Separation and Purification Technology*, 256, 117882. <https://doi.org/10.1016/j.seppur.2020.117882>
- Arias, A. M., Mussati, M. C., Mores, P. L., Scenna, N. J., Caballero, J. A., & Mussati, S. F. (2016). *Optimization of multi-stage membrane systems for CO₂ capture from flue gas*. *International Journal of Greenhouse Gas Control*, 52, 371–382. <https://doi.org/10.1016/j.ijggc.2016.08.005>
- Zhao, L., Riensche, E., Blum, L., & Stolten, D. (2010). *Multi-stage gas separation membrane processes used in post-combustion capture: Energetic and economic analyses*. *Journal of Membrane Science*, 359(1–2), 160–172. <https://doi.org/10.1016/j.memsci.2009.11.041>